Electronic Energy Loss of Heavy Ions and Its Effects in Ceramics

A Dissertation Presented for the

Doctor of Philosophy

Degree

The University of Tennessee, Knoxville

Ke Jin

May 2015

DEDICATION

To my father, Weishi Jin, my mother, Xiaoxin Dai, and my girlfriend, Xiruo Song, for their love and support

ACKNOWLEDGEMENTS

I would like to express my sincere appreciation to Dr. Yanwen Zhang, my advisor, and Dr. William J. Weber, my co-advisor, for their scientific guidance, encouragement and kindness throughout my study, my research, and the completion of this dissertation.

I am grateful to Dr. Zihua Zhu, Mr. Sandeep Manandhar, Dr. Vaithiyalingam Shutthanandan, and Dr. Suntharampillai Thevuthasan from Pacific Northwest National Laboratory (PNNL). They provided tremendous help in both work and life during my visit at PNNL.

I am grateful to all my fellow graduate students and staff members in the Department of Materials Science and Engineering, The University of Tennessee, Knoxville, for the wonderful time we spent together. Especially, I want to thank Mr. Haizhou Xue and Mr. Chien-hung Chen, graduate students in Dr. Zhang and Dr. Weber's group, for providing me enormous help in my research. I cherish the friendship with them.

I am grateful to Dr. Hongbin Bei and Dr. Lawrence H. Heilbronn for serving on my committee, and for their valuable comments and suggestions to my dissertation work.

I am also grateful to Dr. Helmut Paul and Dr. Jianming Xue, for the helpful discussions and insightful suggestions to my research.

My great appreciation goes to my families for their love and support.

ABSTRACT

Energy loss of medium energy heavy ions (i.e. Cl, Br, I, and Au) in thin compound foils containing light elements (i.e. silicon carbide and silicon dioxide) is directly measured using a time-of-flight elastic recoil detection analysis (ToF-ERDA) technique. An improved data analysis procedure is proposed to provide the experimentally determined electronic stopping powers. This analysis procedure requires reliable predictions of nuclear stopping. Thus, the nuclear stopping predicted by the Stopping and Range of Ions in Matter (SRIM) code is validated by measuring the angular distribution of 1 MeV Au ions after penetrating a thin silicon nitride foil, using a secondary ion mass spectrometry (SIMS). In order to validate our derived electronic stopping power values, Rutherford backscattering spectrometry (RBS) and SIMS are utilized as complementary techniques to measure the depth profiles of implanted Au ions in SiC. Moreover, the original version of the SRIM code, TRIM-85, is modified to adopt our derived electronic stopping powers to predict ion distributions. The comparison studies show that the ion distributions predicted based on our derived electronic stopping powers agree well with the experimental results, but exhibit considerable discrepancies with the SRIM predictions.

The large deviation from SRIM predictions is further observed in other materials. The distributions of implanted Au ions with various energies from 1 to 15 MeV are measured in Si and MgO. The electronic stopping powers for Au ions in Si are estimated based on the measured ion profiles. For Au ion irradiation in MgO, significant channeling effects on the ion and damage profiles are observed for the irradiations along both axial and planar channels.

Furthermore, the effect of electronic energy deposition from medium energy heavy ions (i.e. 21 MeV Ni) on the damage evolution in MgO, in which the initial defects are induced using 1 MeV Au, is studied. The evolution in damage level and damage structure under the irradiations is characterized using RBS/ion channeling technique combined with transmission electron microscopy (TEM).

TABLE OF CONTENTS

LIST OF TABLES

LIST OF FIGURES

CHAPTER 1
INTRODUCTION

The energy deposition for energetic ions travelling in matter is generally described by two mechanisms, nuclear energy loss and electronic energy loss. Nuclear energy loss is attributed to the elastic collisions with target nuclei, results in the displacement of atoms and dominates in the low energy regime. Electronic energy loss is attributed to the inelastic collisions with target electrons, results in the excitation and ionization of the target electrons, and dominates in the high energy regime. Stopping power (sometimes termed as stopping force) is defined as the energy loss per unit path length.

$$S = -dE / dx \tag{1.1}$$

1.1 Quantification of stopping power

As summarized by Sigmund,[1] quantitative knowledge of stopping power is of critical importance not only in fundamental research in physics and materials science, but also in broad applications such as ion beam modification, ion beam analysis, semiconductor fabrication, nuclear engineering, radiation therapy, space exploration, etc. Thus, quantification of stopping power has been a subject of long-standing experimental and theoretical interest since the early twenty century.

1.1.1 Nuclear stopping power

ZBL universal potential and SRIM

Nuclear stopping can be theoretically treated as the elastic two-body scattering between screened particles. According to the conservation of energy and momentum of the system, the elastic energy transfer T can be described as[2]:

$$T = \frac{2M_1M_2}{(M_1 + M_2)^2} E_i(1-\cos\theta^*), \tag{1.2}$$

where M_1 and M_2 are the masses of the projectile and target atoms, respectively, E_i is the incident energy of the projectile, and θ^* is the scattering angle in the center-of-mass frame.

In order to obtain the cross-section of the energy transfer, or the nuclear stopping power, the probability for each final scattering angle must be known. The key issue thus

becomes the calculation of the interatomic potentials concerning different screening functions.[3] Four important pioneering models: the Sommerfeld approximation of the Thomas-Fermi potential[4], the Moliere approximation,[5] the Lenz-Jensen,[6,7] and the Bohr potential[8] have been compared to the one of the most widely used potentials at present, the Ziegler-Biersack-Littmark (ZBL) universal screening potential.[3] The later one shows the highest overall accuracy.[3] The ZBL universal screening function, as shown in Fig. 1.1, is based on the calculation of solid-state interatomic potentials of 522 randomly chosen pairs of atoms over the range 1-82 for Z_1 and Z_2, expressed as:

$$\Phi_U = .1818e^{-3.2x} + .5099e^{-.9423x} + .2802e^{-.4028x} + .02817e^{-.2016x} \quad (1.3)$$

where $x = r/a_U$ is the normalized radius, r is the radius, and $a_U = 0.8854a_0/(Z_1^{0.23} + Z_2^{0.23})$ is the screening length.

Connor et al.[9] compared the universal potential with more than a hundred experimental data, and on overall discrepancy within 5% is estimated. The ZBL universal potential is used in the code named *The Stopping and Range of Ions in Matter* (SRIM) by Ziegler et al[3] to provide the nuclear stopping power values and to simulate the scattering process when ions penetrating a target. SRIM has been the most widely used since late 1980s, contributing to more than 700 publications per year as estimated in 2010.[10]

Remaining issues on nuclear stopping power

Due to the relative theoretical simplicity and existing experimental evidence (e.g. Ref.9), the validity and accuracy of SRIM nuclear stopping have been generally accepted. However, at least two issues remain. Firstly, the nuclear stopping calculation assumes neutral ions and target atom in its normal crystalline state; these assumptions make for errors, and may make the nuclear stopping power too large for low energies.[11] Secondly, the previous experimental validations have limitations. For example, the experimental data used in Connor's comparison study[9] are mostly limited to alkali metals and rare gas targets. Few direct transmission measurements on angular distribution of very heavy ions (e.g. Au) through solid films existed, except the ones by Geissel et al.[12] This is possibly due to two difficulties. The first one is the difficulty in fabricating strong and uniformly

thin enough foils to bear the slow heavy ion irradiation. The second one is the difficulty in detecting very heavy ions using semiconductor detectors, compared to light and medium heavy ions such as helium and carbon ions.[13-16] Geissel's experiments utilized a continuously rotatable ToF spectrometer that is, unfortunately, not a standard instrument in most ion beam laboratories.

1.1.2 Electronic stopping power

Early theoretical efforts

The theoretical description of electronic stopping is far more complex than nuclear stopping, since both ions and targets continuously change during the ions' passage[3]: 1) the charge states are continuously changing with ion energy and electron density of the target, and this process is almost impossible to be directly measured; 2) the target electrons polarize in front of and around the ion, changing the local electron density, and the ion charge density also polarizes and change its shape; 3) the electrons of ions penetrating the target electron cloud are subjected to Pauli promotion since its fully occupied electron shells merge with the shells of fully occupied target atom shells; and 4) for semiconductors, the band gaps reduce the available excitation levels that are open for the electrons, reducing the absorption of energy from the ions.

The effort of theoretically quantifying stopping power has been carried out for more than a century. It is dated back to Bohr[17] in 1913 who developed a theory in which the stopping power and ion range were predicted using classical mechanics. Pioneers have established a profound system of theories to treat electronic stopping power from classical to quantum mechanics, from light ions to heavy ions, and from slow ions to swift ions. As the most influential examples, Bethe, Bloch, and Muller[18-22] established the quantum mechanics treatments of electronic stopping and derived the Bethe-Bloch formula to describe the electronic stopping power of swift ions; Fermi formed the idea of the treatment of target electrons as plasma;[23] Lindhard derived the famous Lindhard-Scharff (LS) formula[24,25] that is substantially applied for slow heavy ions:

$$S_e(E) = k' E^{1/2}, \tag{1.4}$$

where $k' = 3.83 \frac{Z_1^{7/6} Z_2}{M_1^{1/2} (Z_1^{2/3} + Z_2^{2/3})^{3/2}}$ (1.5)

S_e (E) is given in units of 10^{-15} eVcm^2/atom and E is in keV[2]. Besides, Lindhard developed a generalized treatment of interaction between swift light ions[26-28] and electron gas (Lindhard gas). Those theories, especially the Lindhard's theories have been thoroughly and comprehensively reviewed by Ziegler,[3] and Sigmund.[1,29]

In the recent years, first principle calculations, such as the time-dependent density functional theory method (TD-DFT), have been developed to acquire accurate electronic stopping power, but they are strongly limited to the simplest cases, such as low energy light ions due to the extreme computational expense.[30-32] Because an accurate theoretical description of inelastic process for ions in materials is extremely complex, especially for semiconductors, empirical or semi-empirical descriptions based on the experimental results are still the most common approaches up-to-date.

SRIM's integration

The Lindhard's free electron gas theory combing the local density approximation[33] is the key of calculating the electronic stopping power of proton in SRIM, which is the foundation of the calculation for all other ion-solid combinations. SRIM uses "scaling" method to simplify the calculation of heavy ion electronic stopping power.[3] In this method, heavy ion stopping power is calculated from the light ion stopping power at the same velocity in the same medium. For helium ions, the equivalent H stopping is multiplied by the He effective charge at the same velocity

$$S_{He} = S_H (Z_{He} \gamma_{He})^2, \quad (1.6)$$

where γ is the fractional effective charge.

$$\gamma_{He}{}^2 = 1 - \exp[-\sum_0^5 a_i Ln(E)^i] \quad (1.7)$$

where a_i are fitting parameters. For E<1 keV/u, S_e is proportional to the velocity of ions.

It is important to note that strictly speaking keV/u is not a unit of either energy or velocity, and "specific energy" is probably a more accurate term. However, the terms in the literature have not been consistent. In this dissertation, the "specific energy" is abbreviated as energy for convenience.

For ions heavier than He, the scaling approach is different in three energy regimes. 1) for low velocity ions (<25 keV/u, except when Z_1<19 in band gap target with very low energy), the Lindhard treatment is employed that *Se* is generally proportional to the velocity of ions. However the numeric input (e.g. constant of proportionality) could be significantly different by fitting the experimental data;[1] 2) for high velocity ions (>200 keV/u), the Thomas-Fermi scaling rules are used to generalize the heavy ions stopping power; and 3) for medium velocity ions (25 keV/u<E<200 keV/u), the theory proposed by Brandt and Kitagawa[34] is adopted to scale heavy ion stopping power to proton stopping power. In any cases, the final values given by SRIM, as well as other empirical codes (e.g. MSTAR[35,36]), are based on fitting and extrapolating experimental data.[37]

SRIM's accuracy for light ions

It can be naturally expected from the descriptions above that the accuracy of electronic stopping power given by SRIM strongly depends on the amount and quality of experimental values, and this is one of the reasons why the electronic stopping power in SRIM updates regularly.[1]

The most abundant and consistent experimental data exist for helium ions (much more than any others, including proton).[3] This is mainly attributed to the development of Rutherford backscattering spectrometry (RBS) technique since 1970s,[38,39] in which the helium ions from a few hundred keV to a few MeV is the predominantly used particle. Since there have been hundreds of experimental measurements available on the stopping power for light and medium heavy (e.g. from Li to Ar) ions and new stopping data are becoming rapidly available, it is hard to comprehensively review them in a single work. Fortunately, since 1990s, Paul[40] and his colleagues have built and are continuously updating a web-database ("https://www-nds.iaea.org/stopping/" available at present), in which the experimental results, as well as the theoretical models (SRIM is one of the

major models) are collected, commented, compared, and plotted. In addition, the accuracy of existed models (or, programs) is statistically tested. It is shown[40,41] that the accuracy of the SRIM predicted electronic stopping power for He ions is high, as expected due to the large amount of available data. The mean normalized differences $\delta = 100 \times (S_{\exp} - S_{table}) / S_{\exp}$ between the SRIM values and over 2000 experimental data points for He ions in 16 elemental solids and ~150 condensed compounds are (1.7±7.3)% and (-0.4±5.3)%, respectively. For medium heavy ion stopping, there are also more than a thousand experimental data points in total, and, as expected, the SRIM predictions hold a similar accuracy comparing to light ions.

Difficulties in stopping measurements for heavier ions

While electronic stopping powers for light ions have been extensively measured and validated, the measurement for very heavy ions (e.g. Au) in the low and medium energy regime has been a long-standing challenge. The direct measurement of electronic stopping power can be generally done with two geometries: backscattering[42] and transmission[43], while in each geometry there are numerous specific ways of producing the ions, locating the target, and detecting the ions.[44] Backscattering geometry is mainly used for light ions in heavy targets due to the kinematic restriction. For heavy ions in light target, transmission geometry is usually needed. In transmission geometry, due to the difficulties of manufacturing high-quality (high purity and high uniformity) thin stopping foils, previous measurements mainly focused on high energies. For example, in Jokinen's stopping work[45] on Au ions in C, a ~1000 nm C foil was used and the stopping power could only be measured down to 11 MeV. On the other hand, the determination of the density and the thickness of stopping foils are essential to the measured stopping power values and, for a very thin foil, the error in thickness becomes increasingly critical.[43,46]

There are two additional issues that make the difficulties of measurements significantly increase with increasing mass of ions, leading to very limited available experimental data. Firstly, the energy determination of semiconductor detectors becomes

more problematic for heavier ions and the calibration becomes challenging.[13-16] For example, the pulse height defect (PHD)[47], as shown in Fig. 1.2, is normally defined as the difference between the true energy of the heavy ion and its apparent energy in Si detector, such that heavier ions have lower pulse height than light ions with the same energy. In addition, small deviations from linear behavior for heavy ions also exist and make the conventional method of calibrating a Si detector challenging.[14,15] Secondly, as stated above, nuclear stopping dominates in the low energy regime and electronic stopping dominates in the high energy regime. In the medium energy regime, the situation becomes complex: although electronic energy loss is the dominating process, the nuclear energy loss cannot be neglected when ions penetrate stopping foils. The ratio of nuclear stopping power to electronic stopping power, given by SRIM, for Cl, Br, I and Au ions in SiC is shown in Fig. 1.3 in the energy regime of a few MeV. The ratio of nuclear stopping power to electronic stopping power in SiC is less than 2% for ions lighter than Cl and with energies higher than 3 MeV. The nuclear energy loss is, therefore, negligible for lighter ions in the total energy loss measurement. For heavier ions, the ratio at 3 MeV is 0.23, 0.65 and 0.89 for Br, I and Au ions, respectively. As a result, a correction of contributing nuclear energy loss is necessary when measuring electronic stopping powers for these ions in this energy regime. As was reported by Paul,[11] a few previous measurements neglected the nuclear stopping contribution and concluded that the measured electronic stopping power is similar or larger than the SRIM prediction. However, these results[45,48,49] are not supported by ion distribution and damage profile measurements, which will be discussed in detail in the following chapters. Previous studies[50] have attempted to correct the nuclear stopping power using Monte-Carlo simulation with a Moliere interaction, but the potential choice and thus the corrected results have been questioned.[51]

Besides direct measurements, deduction from range measurements is another way of determining electronic stopping powers. For example, Zhai et al.[52] deduced electronic stopping power for Au ions in Si by fitting their measured ion range to LSS theory. However, their result indicates that the electronic stopping power is constant with the increase of energy from ~1-3 MeV, which seems questionable. It is important to note that

this questionable result does not necessarily question the LSS model or the removal of nuclear stopping power, because RBS was the only utilized technique, and this makes the range values less validated.

Problems in SRIM predicted electronic stopping power for heavy ions

Due to the lack of experimental support, lower accuracy is expected in the prediction of electronic stopping power by SRIM for very heavy ions. Actually, both theoretical and experimental evidences have indicated considerable error in SRIM predictions. Theoretically, Sigmund[37] introduced a reciprocity criteria to compare electronic stopping power with the roles of projectile and target interchanged. The reciprocity theory states that, in the low energy region (<25 keV/u), where the projectiles are neutral and the probability for electron loss is small, electronic stopping cross-section (in the unit of 10^{-15} $eVcm^2$) remains invariant when interchanging projectile and target atom (at the same velocity, or the same energy in keV/u). This theory can be utilized as a criterion for examining stopping values from both models and experiments. An example is shown in Fig. 1.4[37] (top), where the Si/C combination agrees with the reciprocity theory very well. However, dramatic deviation is observed when combination between very heavy ions (e.g. Au) and light elements (e.g. Al) is examined (Fig. 1.4 bottom), indicating electronic stopping power by SRIM is probably too large. It needs to be noted that, in the case of Au in Al, no experimental data are available. On the other hand, the MSTAR code only provides ions no heavier than Ar, limiting further judgment on SRIM.

Experimentally, considerable discrepancies have been observed in SRIM-predicted ion ranges and disorder profiles in comparison with experimental values for very heavy ions in light targets.[53-59] For example, in the case of 2 MeV Au irradiation in GaN, as shown in Fig. 1.5,[59] both damage range measured by TEM and implanted Au range measured by time-of-flight secondary ion mass spectrometry (ToF-SIMS) are considerably deeper than the prediction by SRIM. The underestimate of ion range indicates an overestimate of stopping power, i.e. electronic stopping power, if the nuclear stopping power is considered accurate. In a direct measurement, using a monoenergy beam, the electronic stopping power of Au in C with energy of ~4 MeV was found to be 6.07 $keV\mu g^{-1}cm^2$,[50]

much smaller than the SRIM value of 14.8 keVμg^{-1}cm^{2}. Although this is a single data point and the nuclear stopping correction may bear criticism,[51] the error shown in SRIM prediction is far beyond the experimental uncertainty.

In general, despite the long history of extensive study, understanding and description on electronic stopping power, especially for heavy ions in compounds containing light elements are far not adequate. "There is less to read and more to do for those engaging in heavy-ion stopping", as pointed out by Sigmund.[1]

1.2 Ion irradiation induced damage evolution in ceramics

1.2.1 Effects of nuclear energy deposition

The effect of energy deposition on defect production and evolution is one of the major subjects in studying materials applied in an irradiation environment. Due to high damage rates, irradiation with heavy ion in the low and medium energy regimes has been commonly used to simulate the damage evolution induced in extreme nuclear radiation environments.[60,61]

The ion channeling technique based on RBS is one of the most commonly applied methods to study irradiation damage in ceramics. The damage range induced by slow heavy ions is usually a few tens to hundreds of nanometers from surface, and build-up of point defect concentration is the first damage stage for most of materials responding to nuclear energy deposition. Several references are listed here as examples for such studies since 2000 on GaN,[62] SiC,[63] ZnO,[64] Al_2O_3,[65] $SrTiO_3$,[66] ZrO_2, [67] and $Gd_2Ti_2O_7$.[68] Despite the fact that sometimes the damage evolution appears confusing after point defects achieve a certain concentration in some ionic ceramics,[64,67] understanding on the materials response to nuclear stopping has been relatively well established. In brief, elastic energy transfer to target atoms can result in displacements of atoms from their original sites, creating atomic-scale defects in the structure. An example is shown in Fig. 1.6, demonstrating the amorphization process in $SrTiO_3$ under 900 keV Au ion irradiations.

1.2.2 Effects of electronic energy deposition

In contrast to nuclear energy deposition, much less understanding has been achieved on the defect response to electronic energy deposition in ceramics, especially from ions in the medium energy regime (a few tens of MeV). The complexity is mainly attributed to the fact that electronic energy deposition plays conflicting roles in the damage dynamics of heavy ion irradiated ceramics.[69] On one hand, damage induced by inelastic collision may be created near the ion track. On the other hand, electronic energy deposition can enhance mobility of point defects and thus promote recovery of displacement damage. As a result, understanding the response of a pre-damaged material to electronic stopping power is highly desired.

In some materials, e.g. ZrO_2,[70,71] and SiO_2,[72] the damage production from electronic energy loss and nuclear energy loss are primarily simple additive and little synergetic effect is observed. In contrast, the electronic energy loss induced annealing, or recrystallization, has been observed in SiC from two kinds of study strategy: 1) dual beam irradiation, including a nuclear stopping dominant beam (e.g. 900 keV I) and a electronic stopping dominant beam (e.g. 36 MeV W)[70,71] and 2) using a nuclear stopping dominant beam to create initial damage, and then using a electronic stopping dominant beam at the same location to "anneal" the pre-damage.[73] The advantage of the first strategy could be the better simulation of the real irradiation environment, while the advantage of second could be the convenience of separating, and elucidating the effect of each kind of energy deposition. Fig. 1.7 shows the annealing effect of 21 MeV Si ions on the pre-damaged SiC single crystal.[73] The diamonds indicate the damage profile after 900 keV Si ion (nuclear stopping dominant) irradiation, the up-triangles indicate the damage profile at the same spot after subsequent 21 MeV Si ion irradiation (electronic stopping dominant). The damage level is clearly decreased due to the electronic energy deposition.

1.2.3 Puzzles in MgO

Comparing to the cases mentioned above, damage evolution in MgO is confusing under either nuclear or electronic energy deposition. Under irradiation from nuclear

stopping dominant beam (e.g. 3 MeV Au and 100 keV Ar), a few previous experiments[74-77] have observed that after defect concentration reaches a certain level, further irradiation may reduce the damage level (from the perspective of ion channeling) and the damage profile could be unexpectedly deeper than the implanted ion profile. There have been several conjectures on the possible cause of these phenomena. At least two papers[74,75] attribute this observation to the annealing effect due to the electronic stopping from the incident ions. However, this explanation is doubtable because the electronic stopping power of both 3 MeV Au and 100 keV Ar are low; let alone at the depth close to damage peak, the energy of ions is further lower and the electronic stopping power is negligible. Other explanations[74,78,79] include the migration of oxygen interstitial, the strain release, the formation of dislocation or cluster, etc. However, there has been insufficient evidence to conclusively demonstrate any one of those proposed mechanisms.

Under dual beam irradiation,[70,71] a similar phenomenon compared to SiC has been observed in MgO that the damage level is lower under the simultaneous irradiation of two beams together than under the low energy beam alone. However, the mechanisms can be expected to be significantly different between SiC and MgO. In SiC, nuclear energy deposition leads to the accumulation of defects (either point defects or clusters) till fully amorphization. The reduction in damage level induced by electronic energy deposition, especially in the two-step irradiation experiment (see Fig. 1.7),[73] could be attributed to the healing, or recombination of the pre-existed defects. In MgO, nuclear energy deposition could not lead to amorphization. Clusters or dislocation loops could be formed under nuclear energy deposition, which could also reduce the damage levels from the perspective of ion channeling.[74-77] As a result, RBS analysis itself on only one dual beam experiment is difficult to elucidate the mechanism of these findings.

1.3 References

1 P. Sigmund, Nucl. Instrum. Methods Phys. Res. B **135**, 1 (1998).
2 G. S. Was, *Fundamentals of Radiation Materials Science: Metals and Alloys*. (Springer, 2007).
3 J. F. Ziegler, J. P. Biersack, and M. D. Ziegler, *SRIM - The Stopping and Range of Ions in Matter*. (SRIM Co., Chester, MD, USA, 2008).
4 A. Sommerfeld, Z. Physik **78**, 283 (1932).
5 G. Moliere, Z. Naturforschung **2**, 133 (1947).
6 W. Lenz, Z. Physik **77**, 713 (1932).
7 H. Jensen, Z. Physik **77**, 722 (1932).
8 N. Bohr, Mat. Fys. Medd. Dan. Vid. Selsk **18** (1948).
9 D. J. O'Connor and J. P. Biersack, Nucl. Instrum. Methods Phys. Res. B **15**, 14 (1986).
10 J. F. Ziegler, M. D. Ziegler, and J. P. Biersack, Nucl. Instrum. Methods Phys. Res. B **268**, 1818 (2010).
11 H. Paul, AIP Conf. Proceedings **1525**, 309 (2013).
12 H. Geissel, W. N. Lennard, H. R. Andrews, D. P. Jackson, I. V. Mitchell, D. Philips, and D. Ward, Nucl. Instrum. Methods Phys. Res. B **12**, 38 (1985).
13 R. Ghetti, B Jakobsson, and H. J Whitlow, Nucl. Instrum. Methods Phys. Res. A **317**, 235 (1992).
14 H. J. Whitlow and Y. Zhang, Nucl. Instrum. Methods Phys. Res. B **190**, 375 (2002).
15 Y. Zhang and H. J. Whitlow, Nucl. Instrum. Methods Phys. Res. B **190**, 383 (2002).
16 Y. Zhang and W. J. Weber, Phys. Rev. B **82**, 075202 (2010).
17 N. Bohr, Philos. Mag. **25**, 10 (1913).
18 F. Bloch, Zeitschrift für Physik **81**, 363 (1933).
19 F. Bloch, Ann. der Phys. **16**, 285 (1933).
20 H. Bethe, Annalen der Physik **397**, 325 (1930).
21 H. Bethe, Zeitschrift für Physik **76**, 293 (1932).
22 C. Møller, Ann. Physik **406**, 531 (1932).
23 E. Fermi, Phys. Rev. **57**, 485 (1940).
24 J. Lindhard and M. Scharff, Phys. Rev. **124**, 128 (1961).
25 J. Lindhard, M. Scharff, and H.E. Schioett, Mat. Fys. Medd . Dan. Vid. Selsk **33**, 1 (1963).
26 J. Lindhard and M. Scharff, Mat. Fys. Medd . Dan. Vid. Selsk **27**, 1 (1953).
27 J. Lindhard, Mat. Fys. Medd . Dan. Vid. Selsk **28**, 1 (1954).
28 J. Lindhard and A. Winther, Mat. Fys. Medd . Dan. Vid. Selsk **34**, 1 (1964).
29 P. Sigmund, Phys. Scripta **28**, 257 (1983).
30 M. Zeb, J. Kohanoff, D. Sánchez-Portal, A. Arnau, J. Juaristi, and E. Artacho, Phys. Rev. Lett. **108**, 225504 (2012).
31 J. Pruneda, D. Sánchez-Portal, A. Arnau, J. Juaristi, and E. Artacho, Phys. Rev. Lett. **99**, 235501 (2007).

32 M. Draxler, S. Chenakin, S. Markin, and P. Bauer, Phys. Rev. Lett. **95**, 113201 (2005).
33 G. J. Iafrate and J. F. Ziegler, J. Appl. Phys. **50**, 5579 (1979).
34 W. Brandt and M. Kitagawa, Phys. Rev. B **25**, 5631 (1982).
35 H. Paul and A. Schinner, Nucl. Instrum. Methods Phys. Res. B **179**, 299 (2001).
36 H. Paul and A. Schinner, Nucl. Instrum. Methods Phys. Res. B **195**, 166 (2002).
37 P. Sigmund, Euro. Phys. J. D **47**, 45 (2008).
38 W-K Chu, J. W. Mayer, and M. A Nicolet, *Backscattering Spectrometry*. (Academic Press, Inc., 1978).
39 L. C. Feldman, J. W. Mayer, and S. T. Picraux, *Materials Analysis by Ion Channeling*. (Academic Press, 1982).
40 H. Paul, (https://www-nds.iaea.org/stopping/, 2012).
41 H. Paul and A. Schinner, Nucl. Instrum. Methods Phys. Res. B **227**, 461 (2005).
42 P. Bauer, Nucl. Instrum. Methods Phys. Res. B **27**, 301 (1987).
43 P. Mertens, Nucl. Instrum. Methods Phys. Res. B **27**, 315 (1987).
44 H. Geissel, H. Weick, C. Scheidenberger, R. Bimbot, and Gardes Gard, Nucl. Instrum. Methods Phys. Res. B **195**, 3 (2002).
45 J. Jokinen, Nucl. Instrum. Methods Phys. Res. B **124**, 447 (1997).
46 K. Arstila, P. Tikkanen, and J. Keinonen, Nucl. Instrum. Methods Phys. Res. B **136-138**, 98 (1998).
47 G. F. Knoll, *Radiation Detection and Measurement*, 3rd ed. (Wiley, New York, 2000).
48 M. Barbui, D. Fabris, M. Lunardon, S. Moretto, G. Nebbia, S. Pesente, G. Viesti, M. Cinausero, G. Prete, V. Rizzi, K. Hagel, S. Kowalski, J. B. Natowitz, L. Qin, R. Wada, and Z. Chen, Nucl. Instrum. Methods Phys. Res. B **268**, 20 (2010).
49 Y. Zhang, W. Weber, and C. Wang, Phys. Rev. B **69**, 205201 (2004).
50 W. N. Lennard, H. Geissel, D. P. Jackson, and D. Philips, Nucl. Instrum. Methods Phys. Res. B **13**, 127 (1986).
51 Lev G. Glazov and P. Sigmund, Nucl. Instrum. Methods Phys. Res. B **207**, 240 (2003).
52 Y. Zhai, X. Lu, T. Zheng, Z. Xia, and D. Shen, Nucl. Instrum. Methods Phys. Res. B **135**, 128 (1998).
53 Y. Zhang, I. T. Bae, K. Sun, C. Wang, M. Ishimaru, Zi. Zhu, W. Jiang, and W. J. Weber, J. Appl. Phys. **105**, 104901 (2009).
54 E. Friedland, S. Kalbitzer, M. Hayes, C. Klatt, G. Konac, and C. Langpape, Nucl. Instrum. Methods Phys. Res. B **136**, 147 (1998).
55 P. L. Grande, P. F. P. Fichtner, M. Behar, and F. C. Zawislak, Nucl. Instrum. Methods Phys. Res. B **35**, 17 (1988).
56 M. Behar, P. F. Fichtner, C. A. Olivieri, J. P. De Souza, F. C. Zawislak, and J. P. Biersack, Nucl. Instrum. Methods Phys. Res. B **6**, 453 (1985).
57 L. Palmetshofer, M. Gritsch, and G. Hobler, Mater. Sci. Eng. B **81**, 83 (2001).
58 H. Z. Xue, Y. Zhang, Z. Zhu, W. M. Zhang, I. T. Bae, and W. J. Weber, Nucl. Instrum. Methods Phys. Res. B **286**, 114 (2012).
59 Y. Zhang, M. Ishimaru, J. Jagielski, W. M. Zhang, Z. Zhu, L. Saraf, W. Jiang, L. Thome, and W. J. Weber, J. Phys. D: Appl. Phys **43**, 085303 (2010).

60 J. C. Dran, Solid State Phenomena **30-31**, 367 (1992).
61 Y. Zhang, J. Lian, C. Wang, W. Jiang, R. Ewing, and W. Weber, Phys. Rev. B **72**, 094112 (2005).
62 S. O. Kucheyev, J. S. Williams, C. Jagadish, J. Zou, and G. Li, Phys. Rev. B **62**, 7510 (2000).
63 W. Jiang and W. J. Weber, Phys. Rev. B **64**, 125206 (2001).
64 S. O. Kucheyev, J. S. Williams, C. Jagadish, J. Zou, C. Evans, A. J. Nelson, and A. V. Hamza, Phys. Rev. B **67**, 094115 (2003).
65 C. S. Schnohr, E. Wendler, K. Gartner, W. Wesch, and K. Ellmer, J. Appl. Phys. **99**, 123511 (2006).
66 Y. Zhang, J. Lian, C. M. Wang, W. Jiang, R. Ewing, and W. J. Weber, Phys. Rev. B **72**, 094112 (2005).
67 S. Moll, L. Thome, G. Sattonnay, A. Debelle, F. Garrido, L. Vincent, and J. Jagielski, J. Appl. Phys. **106**, 073509 (2009).
68 S. Moll, G. Sattonnay, L. Thome, J. Jagielski, C. Decorse, P. Simon, I. Monnet, and W. J. Weber, Phys. Rev. B **84**, 064115 (2011).
69 S. J. Zinkle, V. A. Skuratov, and D. T. Hoelzer, Nucl. Instrum. Methods Phys. Res. B **191**, 758 (2002).
70 L. Thomé, A. Debelle, F. Garrido, P. Trocellier, Y. Serruys, G. Velisa, and S. Miro, Appl. Phys. Lett. **102**, 141906 (2013).
71 L. Thome, G. Velisa, A. Debelle, S. Miro, F. Garrido, P. Trocellier, and Y. Serruys, Nucl. Instrum. Methods Phys. Res. B **326**, 219 (2014).
72 M. Toulemonde, W. J. Weber, G. Li, V. Shutthanandan, P. Kluth, T. Yang, Y. Wang, and Y. Zhang, Phys. Rev. B **83**, 054106 (2011).
73 Y. Zhang, T. Varga, M. Ishimaru, P. D. Edmondson, H. Xue, P. Liu, S. Moll, F. Namavar, C. Hardiman, S. Shannon, and W. J. Weber, Nucl. Instrum. Methods Phys. Res. B **327**, 33 (2014).
74 E. Wendler, K. Gärtner, and W. Wesch, Nucl. Instrum. Methods Phys. Res. B **257**, 488 (2007).
75 H. Ogiso, S. Nakano, and J. Akedo, Nucl. Instrum. Methods Phys. Res. B **206**, 157 (2003).
76 E. Friedland, Nucl. Instrum. Methods Phys. Res. B **80-81**, 128 (1993).
77 E. Friedland and M. Hayes, Nucl. Instrum. Methods Phys. Res. B **65**, 287 (1992).
78 L. Gea, C. R. A. Catlow, S. M. M. Ramos, B. Canut, and P. Thevenard, Nucl. Instrum. Methods Phys. Res. B **65**, 282 (1992).
79 S. Moll, Y. Zhang, A. Debelle, L. Thomé, J. Crocombette, Z. Zihua, J. Jagielski, and W. J. Weber, Acta Mater. **88**, 314 (2015).

Appendix 1.1

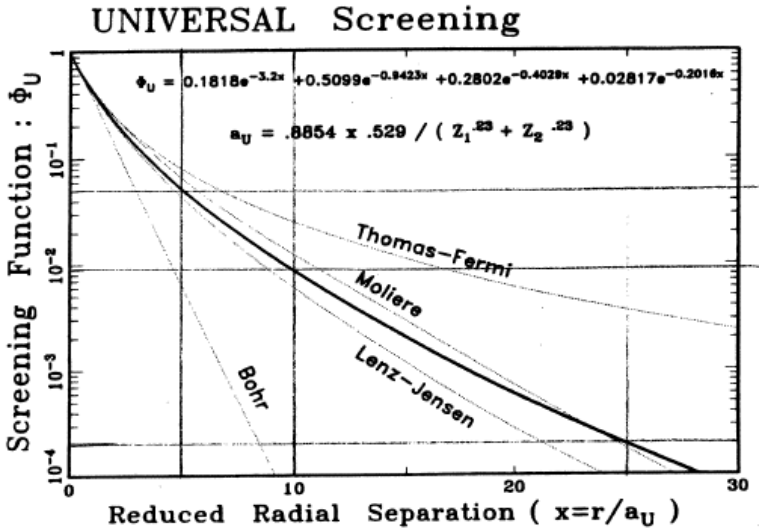

Fig. 1.1. Comparison between the Universal Screening function and previous models. [Ziegler et al, The stopping and range of ions in solids, 1985]

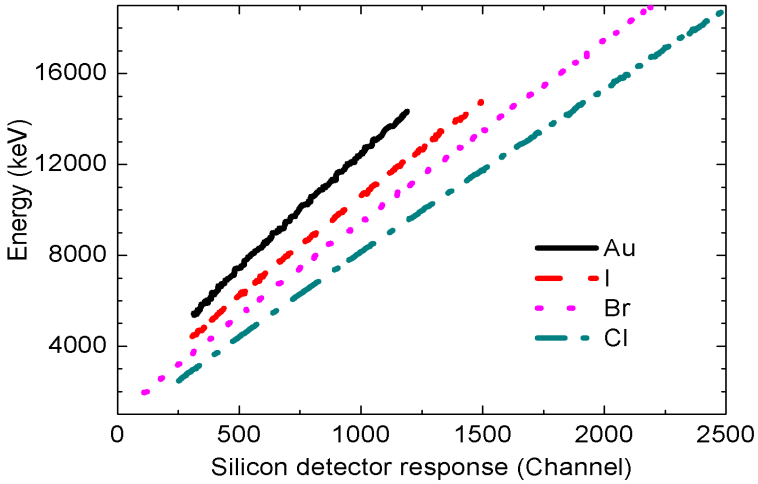

Fig. 1.2. Si detector response to different ion irradiations: energy of various ions versus the corresponding pulse height from the detector (channel number). [Jin et al, Electronic stopping powers for heavy ions in SiC and SiO_2, J. Appl. Phys., 2014]

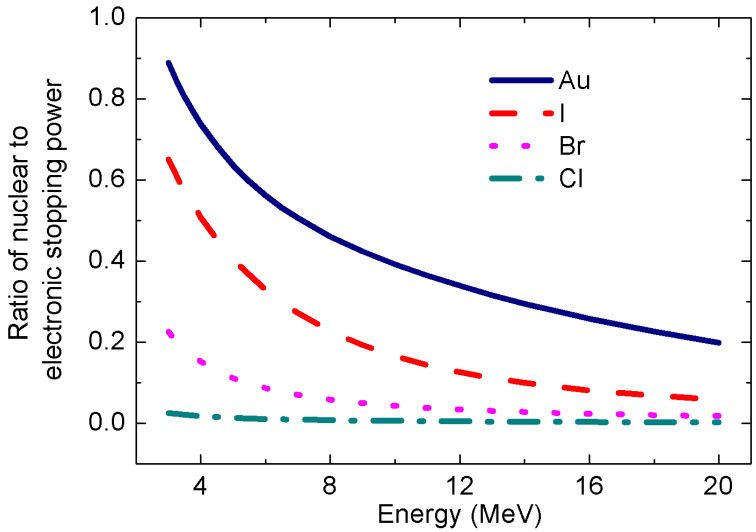

Fig. 1.3. Ratio of nuclear stopping power to electronic stopping power for ions in SiC given by SRIM. [Jin et al, Electronic stopping powers for heavy ions in SiC and SiO_2, J. Appl. Phys., 2014]

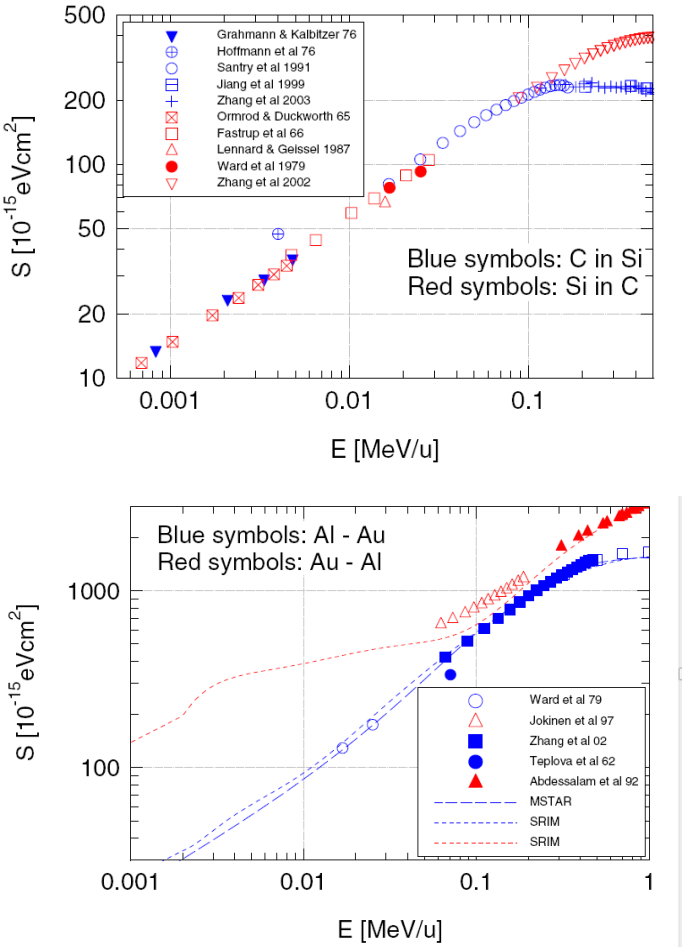

Fig. 1.4. Stopping cross sections for the C/Si combination (top), and the Al/Au combination (bottom). [Sigmund, Reciprocity in the electronic stopping of slow ions in matter, Euro. Phys. J. D, 2008]

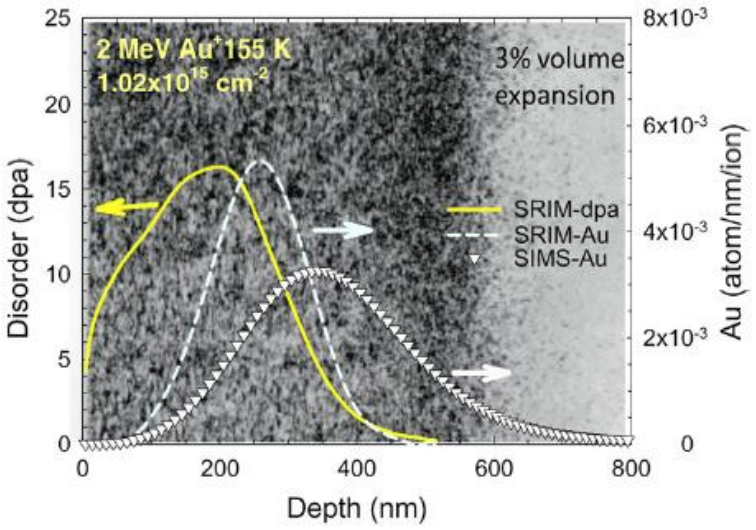

Fig. 1.5. The damage profile (yellow, solid line) is overlaid on top of the TEM image for 2 MeV Au ion irradiation in GaN. The corresponding Au ion distributions predicted by SRIM (dash line) and measured by SIMS (triangles) are also plotted for comparison. [Zhang et al, Damage and microstructure evolution in GaN under Au ion irradiation, J. Phys. D: Appl. Phys., 2010]

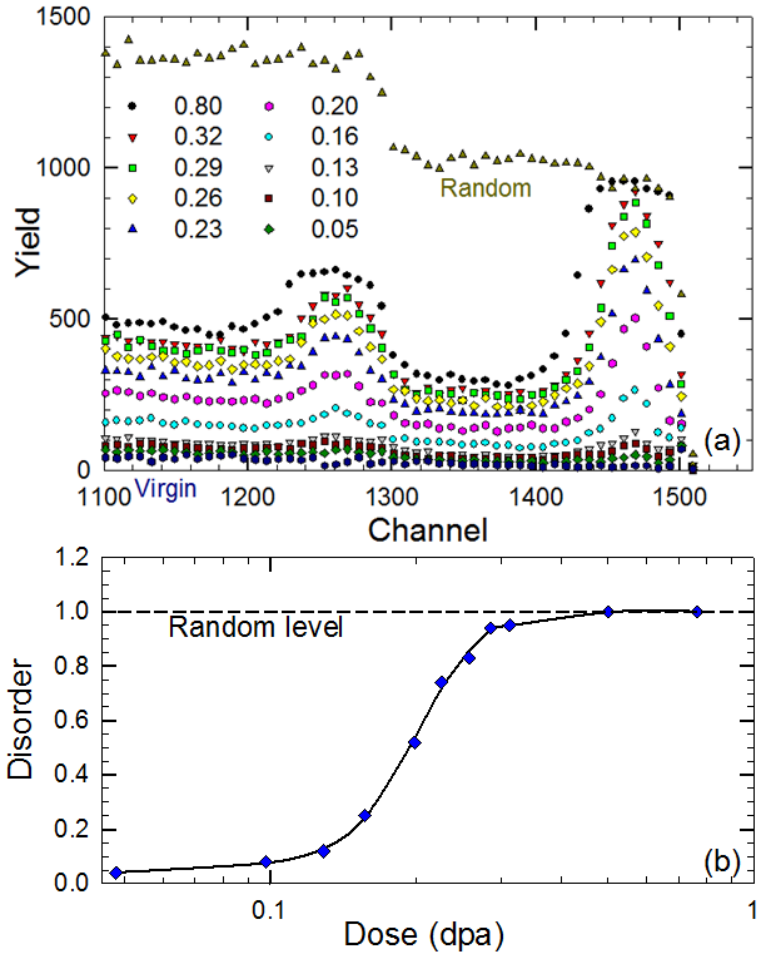

Fig. 1.6. (a) RBS/channeling spectra of $SrTiO_3$ irradiated with 900 keV Au^+ to different ion fluences. (b) Relative disorder as a function of local dose at the damage peak in $SrTiO_3$. [Zhang et al, New ion beam materials laboratory for materials modification and irradiation effects research, Nucl. Instr. Meth. Phys. Res., Sect. B, 2014]

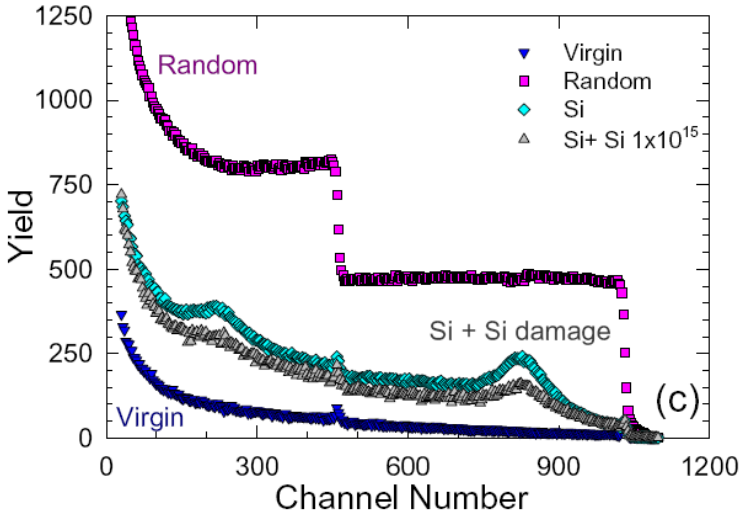

Fig. 1.7. Annealing effect of 21 MeV Si ions on the 4H-SiC single crystal pre-damaged by 900 keV Si ions. [Zhang et al, Competing effects of electronic and nuclear energy loss on microstructural evolution in ionic-covalent materials, Nucl. Instrum. Methods Phys. Res. B, 2014]

CHAPTER 2
EXPERIMENTAL METHODS

2.1 ToF-ERDA measurement

In this study, energy loss measurements are performed using a time-of-flight elastic recoil detection analysis (ToF-ERDA) system, shown in Fig. 2.1. The setup consists of a ToF spectrometer followed by a Si detector.[1]

Monoenergetic ions are produced using a tandem accelerator and scattered by a Au target into the ToF spectrometer with a continuous range of energies. The energy of each ion is determined by the ToF spectrometer following a linear calibration relationship:

$$T(ns) = a_1 T(ch) + a_0 \tag{2.1}$$

where $T(ns)$ is the measured time in the unit of nanosecond, $T(ch)$ is the measured time in channel number, and a_1 and a_0 are the slope and offset in the linear calibration, respectively.

In order to obtain accurate time calibration, two complementary methods are used. First, a time calibration module (ORTEC module 462) is used to generate pulse signals with equal time intervals. Multiple series of measurements could give an accurate value on the time slope a_1. Second, the largest energy of the detected ions can be determined by

$$E_{\max} = E_i \frac{4M_1M_2}{(M_1+M_2)} \cos^2\varphi \text{, for the recoils, and} \tag{2.2}$$

$$E'_{\max} = E_i \frac{M_1^2}{(M_1+M_2)^2} \{cos\varphi + [(\frac{M_2}{M_1})^2 - \sin^2\varphi]^{1/2}\}^2 \text{, for the projectiles,} \tag{2.3}$$

where φ is the scattering angle, E_i is the incident energy, M_1, and M_2 are the masses of projectile and target, respectively. In this study, the projectile is used for analysis. The high-energy edges of different elements scattered from the sample surface are used to calibrate the time offset a_0.

Stopping foils are mounted on a push-rod that can be reproducibly moved into and out of the ion path between the ToF spectrometer and the Si detector. With the stopping foil out of the ion path, the Si detector directly measures the energy (E_{Si1}) of the ions leaving from the ToF spectrometer (E_{T1}); each channel of the Si detector is, therefore, calibrated

using the corresponding ToF energy.[1] In this way, the calibration difficulties for a Si detector in response to heavy ions are eliminated. Since the ions lose energy when passing through the C_{out} film (Fig. 2.1) before leaving the ToF, a correction for the small energy loss (ΔE_{C1}) is included:

$$E_{Si1} = E_{T1}^{'} = E_{T1} - \Delta E_{C1}. \tag{2.4}$$

With a stopping foil in the ion path, each ion exiting from the ToF and detected in the Si detector has energy:

$$E_{Si2} = E_{T2}^{'} - \Delta E = E_{T2} - \Delta E_{C2} - (\Delta E / \Delta x) \cdot \Delta x \tag{2.5}$$

where, Δx is the thickness of the stopping foil and ΔE is the energy loss in the stopping foil. Using Eqs. (2.4) and (2.5) and considering the two ToF energies that yield the same energy in the Si detector (i.e., $E_{Si1} = E_{Si2}$), the stopping power (with small Δx) is given by:

$$dE / dx = (E_{T2}^{'} - E_{T1}^{'}) / \Delta x \tag{2.6}$$

at the corresponding energy of $(E_{T2}^{'} + E_{T1}^{'})/2$.

An example of He ion stopping is shown in Fig. 2.2. In Fig. 2.2 (a), two correspondence curves are shown between the Si detector and the ToF with and without the stopping foil. Fig. 2.2 (b) shows the ToF time responses for He ions at the pulse height channel of 2000 from the Si detector. The difference in energy determined by ToF is considered as the energy loss in the stopping foil.

In this measurement, two self-supported stopping foils are used. The SiO_2 foil (36 μg cm^{-2}) was produced by physical vapor deposition (Luxel Corporation, WA 98250, USA), and the SiC foil (82 μg cm^{-2}) was prepared by high-temperature, low-pressure chemical vapor deposition (FLX Micro, Cleveland, OH, USA). The thickness of the foils was determined by measuring the electronic energy loss of He ions in these foils as demonstrated in previous studies.[2-4] The value of the thickness is adjusted so that the determined stopping power agreed with SRIM. The experimentally determined values and the SRIM results for electronic stopping power for He ions in both SiC and SiO_2 are

shown in Figs. 2.3 (a) and (b), respectively. The foundation of this method is the fact, stated in chapter 1, that the SRIM prediction of electronic stopping power of He ions has been extensively validated by numerous experiments and is considered accurate. In this way, the error in measuring the foil thickness, including the density uncertainty and the roughness, is minimized.

2.2 Correction of effective nuclear energy loss

As discussed in chapter 1, the contribution of nuclear energy loss in the measurements has to be corrected to derive realistic electronic stopping power values. However, the tabulated nuclear stopping power cannot be directly subtracted from the measured results. In the measured energy loss, the contribution from electronic energy loss is assumed to have a negligible dependence on collision scattering angle, but the nuclear energy loss is strongly dependent on the collision scattering geometry. With the stopping foil in place, ions that encounter large-angle scattering will not be detected within the small solid angle constrained by the collimator, as shown in Fig. 2.1. Thus, only ions with smaller scattering angles, corresponding to the ions with smaller nuclear energy loss in the foil, can be detected by the Si detector. For example, based on SRIM simulations, only ~47% and 75% of the Au ions with incident energies of 6 and 10 MeV on SiC, respectively, can be detected by the Si detector. The remaining ions, which encountered larger angle scattering, will be stopped by the collimator. Another example for I ions penetrating an Al foil was discussed by Paul,[5] and a similar result was observed. In this work, the effective nuclear energy loss is defined as the average nuclear energy loss for the ions that can be detected for a specific geometry determined by the experimental setup, and the total nuclear energy loss is referred to the average of all ions that is given by SRIM (in the Stopping / Range Tables).

The correction of the effective nuclear energy loss is determined by the following steps: 1) apply SRIM simulations to determine the exit angle and position for an ion penetrating through the stopping foil; 2) determine the position when the ion reaches the Si detector based on the present experimental configuration (relative location of the stopping foils and the Si detector) and compare the radius with the diameter of the

collimator located in front of the Si detector to determine whether the ion is within the collimator and will be detected; 3) perform such simulations for a large number of ions with different incident energies (~50,000 per energy); and 4) for each incident energy, calculate the mean energy loss of those detectable ions for the corresponding ion energy (average of the energy before and after penetrating the stopping foil), and obtain a continuous curve fit of mean energy loss (S_e+Eff S_n) as a function of ion energy, shown by solid curves in Fig. 2.4(a). The effective nuclear energy loss is the difference between these curves and those of electronic energy loss. The final step is: 5) subtract the effective nuclear energy loss from the measured values.

This correction method is based on the assumption that SRIM provides a reasonable prediction of nuclear stopping powers and has little correlation with SRIM predicted electronic stopping powers. In this correction method, 1) the error on electronic stopping power for each energy is cancelled out in step (5) based on the independence of electronic stopping power with the scattering angle, as well as the small difference in the ion path-length in the thin foils; and 2) this correction is not based on "incident energy" but on an "average energy" that is shown as the smooth curve obtained in step (4). In other words, for ions with the same average energy, their nuclear stopping power and thus their scattering behavior are the same regardless of the incident or exit energy. The error on electronic stopping power that mainly affects the slowing down process, therefore, has minimal effects on this correction.

As shown in Fig. 2.4(a), the effective nuclear energy loss is a significant contribution to the total energy loss for Au ions, and becomes less significant but not negligible for Br ions. The results in Fig. 2.4(b) show the electronic stopping powers with and without the effective nuclear stopping correction, as well as with total nuclear stopping subtraction. The SRIM predicted results are also included for comparison. It is evident that the correction is crucial to the final results. The key issue of the reliability of this correction is whether the SRIM predicted angular distribution of ions penetrating a thin foil is correct. As discussed in chapter 1, the nuclear stopping power predicted by SRIM has been generally accepted but the direct experimental validations of such angular

distributions are still limited by the requirement of unique equipments. In this study, a newly designed experiment is performed for this validation (see section 2.3 and chapter 4). The result shows that the SRIM predictions on angular distribution are reasonable, and thus our effective nuclear stopping correction is reliable.

2.3 Measurement of angular distribution of Au ions penetrating a Si_3N_4 thin foil.

The angular distribution measurements mainly consist of two parts, ion irradiation and ToF-SIMS measurement. The setup of ion irradiation is shown in Fig. 2.5. Low stress LPCVD (Low Pressure Chemical Vapor Deposition) Si_3N_4 foils are deposited on a Si substrate by Norcada Inc (Edmonton, AB, Canada). The foils range from 95 to 103 nm in thickness, and the actual thickness of each foil was measured independently by ToF-SIMS, scanning electron microscopy (SEM) and transmission electron microscopy (TEM). The density of the foils is provided by the manufacturer as 3.1 g cm^{-3}, which has been confirmed by areal density measurement with RBS in combination with SEM and TEM results. The Si_3N_4 foils are grown on a Si substrate (5 mm × 5 mm, 200 μm thick) that is thick enough to block the incoming beam. A window in the central area of the silicon substrate, 0.25 mm × 0.25 mm, is created by etching[6] and is taken as the beam spot size. The Si_3N_4/Si window is mounted on the front of a metal frame with a thickness of 14.2 mm, and a Si wafer is mounted at the back of this frame. The 1 MeV Au ion irradiations are performed using a tandem accelerator. The Au beam covers the whole 0.25 mm window region, and the transmitted ions are collected by the Si wafer.

The Si wafers implanted with Au ions are subsequently analyzed by ToF-SIMS. As shown in Fig. 2.6, depth profiling is performed across the Si wafer with steps of 0.5 mm. The size of each crater is 0.3 mm × 0.3 mm. At each position, the Au depth profile is integrated to calculate the implanted fluence and is normalized to the $^{30}Si^-$ signal in order to minimize the effects from current fluctuations. In order to locate the center of the Au beam, three line scans are performed on each sample: the first scan is performed from a rough center of the wafer; the second scan starts from the Au peak position of the first

scan along a direction perpendicular to the first scan; and the third scan starts from the Au peak position of the second scan along a direction perpendicular to the second scan (parallel to the first scan). Following such approach, the distributions from the second and the third scan are ensured along the diameters of the Au distribution.

In order to evaluate the thickness change of the foils under ion irradiation, ToF-SIMS depth profiling is performed on both the window (the suspended foil without the Si substrate: irradiated area) and the supported region (the film supported by the Si substrate: virgin area) of each sample under different irradiation fluences. The sputtering rate is determined by the crater depth measured by a Dektak 150 profilometer.

Both SEM and TEM methods are applied to measure the thickness of the foils. The SEM measurements are carried out with FEI Helios 600 Nanolab FIB/SEM. Thin layers of sputtered Au are introduced on both sides of the wafer to enhance the clarity of the Si_3N_4 surfaces. Images are taken under immersion mode at a tilt angle of 52º. TEM measurements are carried out at 200 keV with a Zeiss Libra 200MC TEM/STEM. The detector is equipped with 2K × 2K CCD-camera. The cross-sectional TEM samples are prepared by mechanical polishing following by ion milling. The energy resolution is ~0.15 eV.

2.4 Measurement of the depth profile of implanted ions

In this study, two techniques are used to measure the depth profile of implanted ions: RBS and ToF-SIMS.

RBS is one of the major ion beam analysis techniques used in surface and near surface analysis in solids. A target is bombarded with ions in the energy regime from a few hundreds of keV to a few MeV. The projectiles that are backscattered by the atoms in the solids, from either surface or bulk, are recorded by an energy sensitive detector. In this study, Si detector and He ions are used.

In order to achieve a reliable ion profile from RBS measurements, energy calibration is of critical importance. The energy calibration is usually performed by measuring the maximum energy of the backscattered ions from known elements at a certain scattering

angle, corresponding to the backscattering by the atoms at surface.[7] These maximum energies are determined by Eq. (2.3). Using different calibration samples with known composition and using different ion energies are two commonly used methods for practical energy calibration. Usually, the energy and channel have a linear relationship. Sometimes, a second order polynomial function is needed. An example this is shown in Fig. 2.7. In this case, a few elements and four energies of He ions are used, and all the data points follow well a linear energy-channel relationship. It has been introduced in chapter 1 (see. Fig. 1.2) that energy calibration is different for different types of incident ions, and the linearity may be compromised for heavy ions.

For the signals from a certain element, different exit energies of He ions indicate different depth where the collision occurred. The energy-depth conversion is based on the electronic stopping power of He ions in the samples, and the values predicted by SRIM are widely used. Since the stopping power is energy dependent, accurate analysis usually requires a numerical method combined with a slabs model.[7] In this model, the total depth, x shown in Fig. 2.8, is divided into many small slabs with equal depth Δx. Thus, it can be reasonably assumed that in each slab the stopping power is uniform, and the energies only change at the boundaries between two slabs:

$$_{(n+1)}E = {}_{n}E \mp \left.\frac{dE}{dx}\right|_{nE} \left(\frac{\Delta x}{\cos\theta_{1,2}}\right) \tag{2.7}$$

where, ${}_{n}E$ and $(dE/dx)|_{nE}$ are the energy and stopping power of He ions in the n^{th} slab, respectively, the $\theta_{1,2}$ are the angles between the surface normal direction and the incident or outgoing directions of He beam, respectively. The minus sign is used for the incident beam, and the plus sign is used for the outgoing beam. Note that there is an abrupt change in energy when a collision happens, as described by Eq. (2.3). Following this approach, the exit energy of the He ions can be calculated by adjusting the depth x. In other words, the depth can be derived from the known exit energy.

ToF-SIMS[8] is a powerful technique in depth profiling trace elements in materials. In brief, the sample of interest is sputtered with a beam of primary ions; the secondary ions

formed during the sputtering process are extracted and analyzed using a ToF spectrometry. In this study, the dual beam mode is used to measure depth profile of implanted ions. A 2.0 keV Cs^+ sputter beam with ~130 nA is used to remove materials from sample surfaces at a reasonable rate, while a 25 keV Bi^+ beam with ~1 pA is used for data collection.

The data analysis of ToF-SIMS depth profile is more straightforward comparing to RBS. With stable current of the sputtering beam, the sputter rate is considered either constant or linearly changed. The values are determined by measuring the depth of the crater after the complete sputtering process with a known sputtering time, using ZYGO NewView 200 and Dektak 6 M profilometers.

Compared to RBS, advantages of ToF-SIMS include excellent detection limit (~ppm level) and ultra high depth resolution (a few angstroms). However, SIMS is a destructive measurement (due to the sputtering). Besides, SIMS measures the absolute depth (e.g. unit in nm), while the RBS measure the area density (e.g. unit in 10^{15} atoms/cm^2). In theoretical predictions, the areal density can be directly calculated from the stopping cross-section but the density of the sample is needed to calculate the absolute depth. In practice, volume swelling (i.e. the density decrease) can be induced by large fluence heavy ion irradiation. In SiC, such volume swelling can be as large as 15%[9], which has to be corrected when comparing experimental and theoretical results or comparing RBS and SIMS results.

2.5 Ion channeling measurement of damage profile in single crystals

In this study, an ion channeling technique is used to study damage of MgO under ion irradiation. Channeling[10] is referred to the influence of crystal lattice on the trajectories of energetic particles (usually 1-4 MeV He ions). When incident beam is well aligned with crystal lattice axes or planes (so-called in channeling direction), the close-encounter probability between ions and target atoms will be dramatically reduced. As a result, the backscattering yield from channeling ions is very low (~5%) comparing with that from the ions in “random” direction or ions in an amorphous material.

The imperfections (defects, distortion, etc.) can compromise the low backscattering yield. Normally, point defects (interstitials) have two effects[10] on the incident beam in channeling directions, as shown in Fig 2.9 (top). First, the ions can be directly backscattered, since the interstitials do not sit on the lattice sites. Second, ions can be dechanneled, that is, some channeled ions are scattered into non-channeled directions, behaving the same as a random beam afterwards. As a result, the incident beam can be divided into two fractions, the channeled fraction and the random fraction, as shown in Fig. 2.9 (middle). Similarly, as shown in Fig. 2.9 (bottom), the RBS yield of a damaged sample, χ_D, can also be divided into two fractions. The yield from the channeled beam is a result from direct backscattering by the defects, as shown in the shaded area. The dechanneling yield, shown as χ_R, is a result from dechanneled (random) fraction of the beam. It is important to note that the effect of direct backscattering is restricted within the damage region, but the effect of dechanneling is extended to larger depths. This is why a peak is formed in the channeling spectrum, but yield cannot decrease to the virgin level even though no defect exists in the material at larger depth beyond the damage region.

The principle of deducing the damage level from the RBS spectra is described as following.[10] The damage yield is expressed as:

$$\chi_D(z) = \chi_R(z) + [1 - \chi_R(z)]\frac{fn_D(z)}{n}, \tag{2.8}$$

where, n_D is the defect density, n is the atomic density of sample, f is called the defect scattering factor. Conventionally, f = 0 for pure dechanneling defects, e.g. dislocations; f = 1 for randomly displaced atoms (interstitials). As stated above, χ_R is the dechanneling fraction which cannot be directly measured. Omitting the derivation process, χ_R can be expressed as:

$$\chi_R(z) = \chi_v(z) + [1 - \chi_v(z)][1 - \exp(-\int_0^z \sigma_D n_D(z')dz')], \tag{2.9}$$

where σ_D is the dechanneling factor and χ_v is the yield for the virgin sample.

Combining Eq. (2.8) and (2.9), the defect density n_D can be derived using an iteration method from χ_D and χv, if σ_D is known. However, the dechanneling factor is not a pre-

known value, and its determination is based on many assumptions that are not well understood. As a result, a commonly accepted treatment is making the σ_D a tuning factor.[11] By tuning σ_D, the χ_R curve is correspondingly changed. The suitable σ_D value is determined when the χ_R curve overlaps with χ_D at the depth after which the defect density is considered zero.

2.6 Ion irradiation and fluence calibration

The ion irradiation and implantation are performed using the 3 MV tandem accelerators at both University of Tennessee (UT)[12] and the Pacific Northwest National Laboratory (PNNL). The details of the UT ion beam materials laboratory are introduced in Ref. [12]. The key of successful ion irradiation in damage accumulation and evolution studies is precise control of the fluences. Several fluence calibrations have been performed. Au ions are selected in the calibrations due to the achievable high beam current and high backscattering cross section of He on Au. One example of fluence calibration is illustrated in Fig. 2.10, where a Si sample is implanted with 2.25 MeV Au^{2+} ions. After the Au ion implantation to the fluence of 6.1×10^{15} cm^{-2}, RBS is performed using 2.0 MeV He ions. As shown in Fig. 2.10, the concentration of Au shown in the RBS spectrum is determined by fitting the data to a simulated profile obtained using SIMNRA software[13]. The diamonds are the data from the RBS measurement, and the dashed line is the fit from SIMNRA. In this example, while the intended fluence is 6.1×10^{15} cm^{-2}, the fluence determined by SIMNRA simulation is 6.3×10^{15} cm^{-2}. Such fluence calibration has been performed several times using Au ion with different energies in different targets, and the uncertainty of our irradiation fluence is within ±10%.

2.7 References

1 Y. Zhang, Nucl. Instrum. Methods Phys. Res. B **196**, 1 (2002).
2 Y. Zhang, W. Weber, and C. Wang, Phys. Rev. B **69**, 205201 (2004).
3 Y. Zhang, W. J. Weber, D. E. McCready, D. A. Grove, J. Jensen, and G. Possnert, Appl. Phys. Lett. **87**, 104103 (2005).
4 J. F. Ziegler, (www.srim.org).
5 H. Paul, AIP Conf. Proceedings **1525**, 309 (2013).
6 N. E. Flowers-Jacobs, S. W. Hoch, J. C. Sankey, A. Kashkanova, A. M. Jayich, C. Deutsch, J. Reichel, and J. G. E. Harris, Appl. Phys. Lett. **101**, 221109 (2012).
7 W-K Chu, J. W. Mayer, and M. A Nicolet, *Backscattering Spectrometry*. (Academic Press, Inc., 1978).
8 J. C. Vickerman and D. Briggs, *ToF-SIMS: Surface Analysis by Mass Spectrometry*. (Manchester and IM Publications, 2001).
9 I. T. Bae, W. J. Weber, and Y. Zhang, J. Appl. Phys. **106**, 123525 (2009).
10 L. C. Feldman, J. W. Mayer, and S. T. Picraux, *Materials Analysis by Ion Channeling*. (Academic Press, 1982).
11 L. Shao and M. Nastasi, Appl. Phys. Lett. **87**, 064103 (2005).
12 Y. Zhang, M. L. Crespillo, H. Xue, K. Jin, C. H. Chen, C. L. Fontana, J. T. Graham, and W. J. Weber, Nucl. Instrum. Methods Phys. Res. B **338**, 19 (2014).
13 M. Mayer, SIMNRA, http://home.rzg.mpg.de/~mam/. (2014).

Appendix 2.1

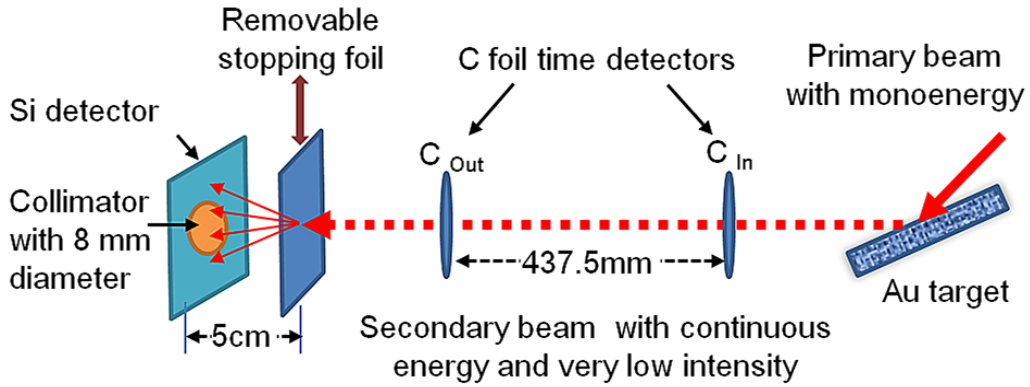

Fig. 2.1. Schematic illustration of the experimental configuration of a ToF-ERDA system for energy loss measurements. [Jin et al, Electronic stopping powers for heavy ions in SiC and SiO_2, J. Appl. Phys., 2014]

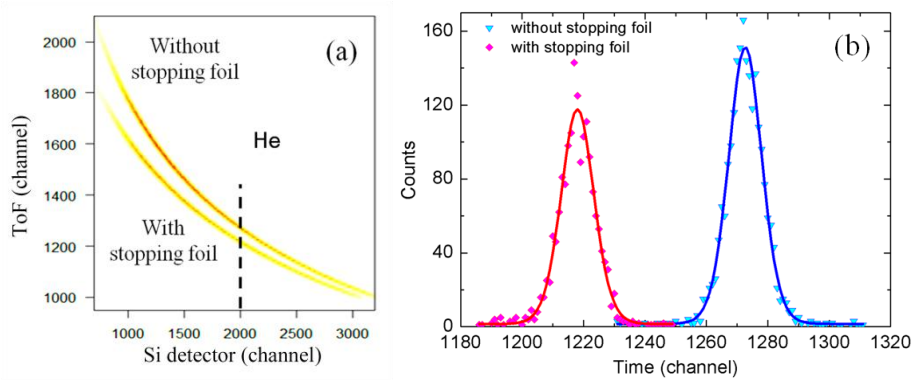

Fig. 2.2. (a) Contour map of the ToF-Si detector correspondence for He ions, with and without the stopping foil. (b) Time diagram at channel 2000 from the Si detector. [Jin et al, Electronic stopping powers for heavy ions in SiC and SiO_2, J. Appl. Phys., 2014]

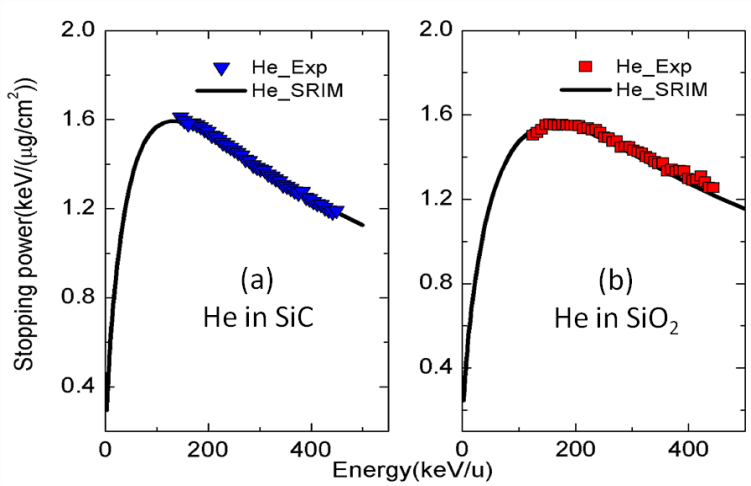

Fig. 2.3 Comparisons of electronic stopping powers for He ions in (a) SiC and (b) SiO_2 between the measured results and the SRIM predictions. [Jin et al, Electronic stopping powers for heavy ions in SiC and SiO_2, J. Appl. Phys., 2014]

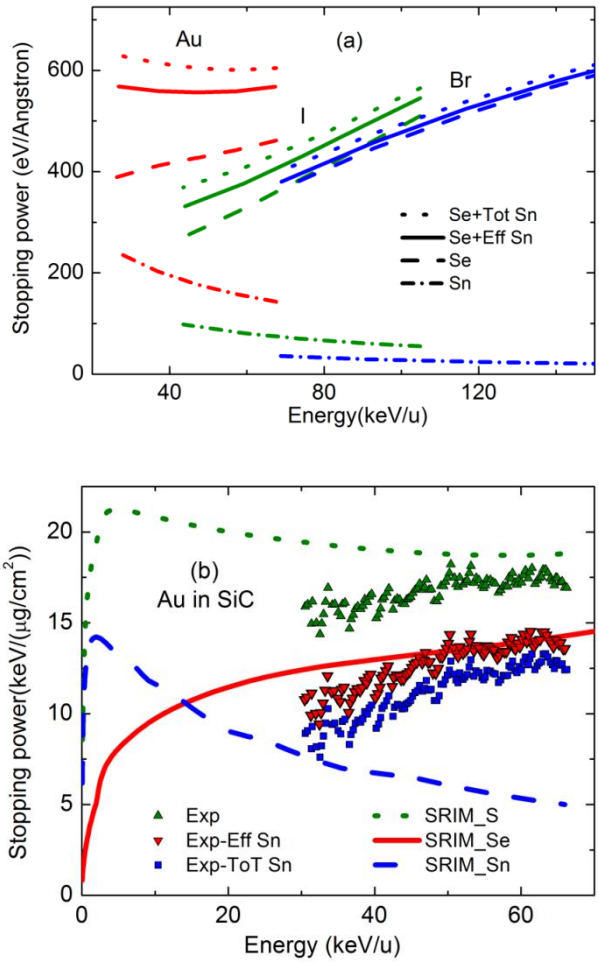

Fig. 2.4. Ions in SiC: (a) SRIM prediction of the mean energy loss (solid line) of the ions detected by the Si detector, with the nuclear stopping power (dash dot), electronic stopping power (dash), and total stopping power (dot) of Au, I, and Br ions in SiC. (b) Comparison between uncorrected (Exp), effective nuclear stopping corrected (Exp-Eff Sn) and total nuclear stopping corrected (Exp-Tot Sn) data of measured electronic stopping power for Au ions in SiC; along with the SRIM predictions. [Jin et al, Electronic stopping powers for heavy ions in SiC and SiO_2, J. Appl. Phys., 2014]

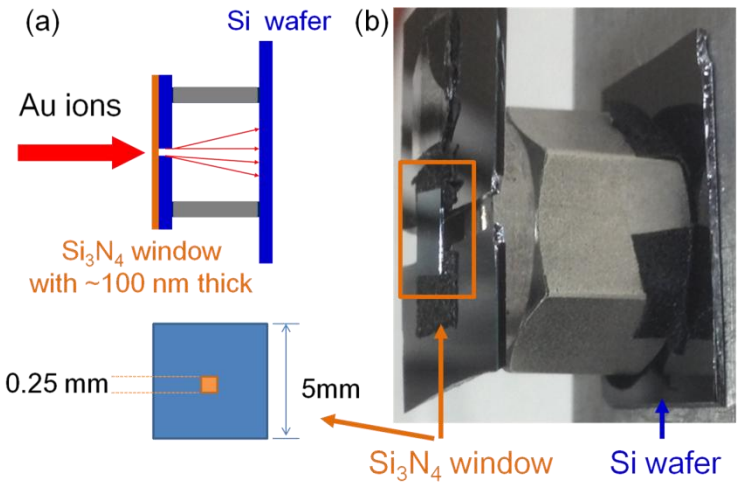

Fig. 2.5. (a) Schematic illustration and (b) a photo of the setup to collect scattered Au ions penetrating a Si_3N_4 thin foil. The penetrated Au ions are collected in a Si wafer located at the rear of the metal frame. The suspended Si_3N_4 foil (0.25 mm × 0.25 mm) at the center of the Si wafer is defined as the "window region" and the rest of Si_3N_4 thin film is defined as "supported region". [Jin et al, Angular distribution and recoil effect for 1 MeV Au^+ ions through a Si_3N_4 thin foil, Nucl. Instr. Meth. Phys. Res., Sect. B, 2014]

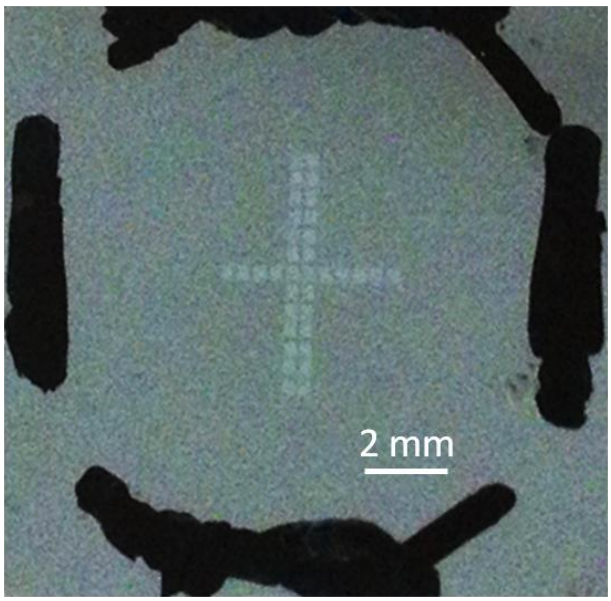

Fig. 2.6. A photo of a Si wafer after lateral scan by ToF-SIMS depth profiling to determine the Au ion concentration as a function of radius. [Jin et al, Angular distribution and recoil effect for 1 MeV Au^{+} ions through a Si_3N_4 thin foil, Nucl. Instr. Meth. Phys. Res., Sect. B, 2014]

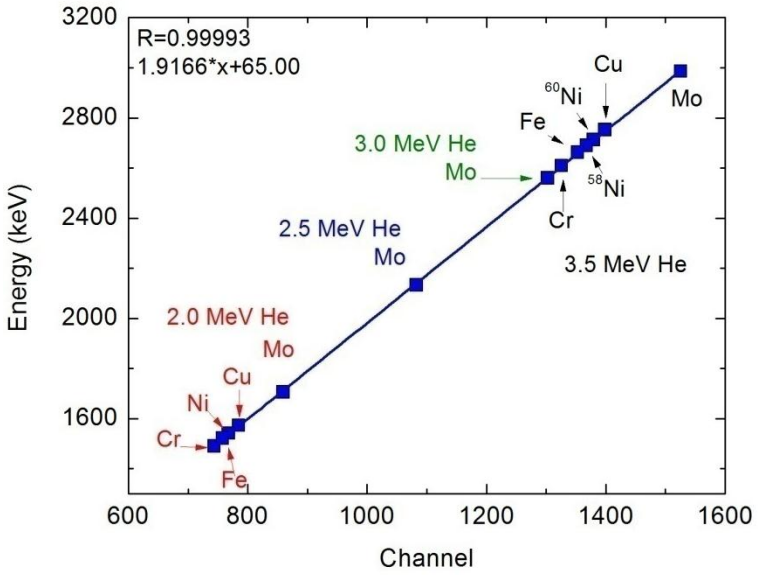

Fig. 2.7. An example of the energy calibration of the Si detector in response to He ions.

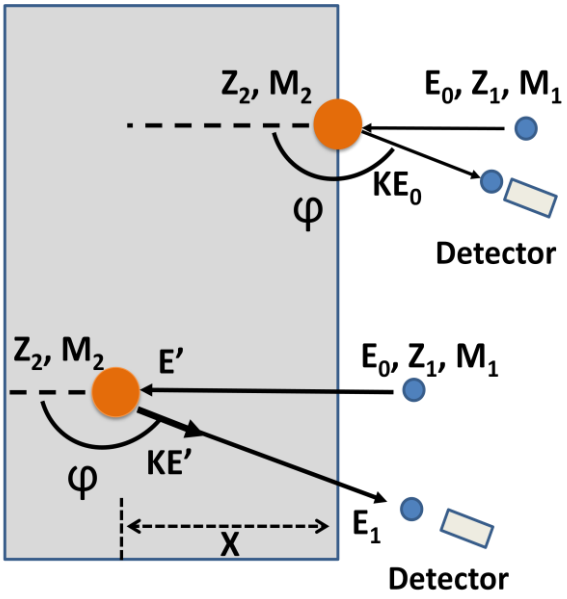

Fig. 2.8. Illustration of the principle of the RBS depth profiling.

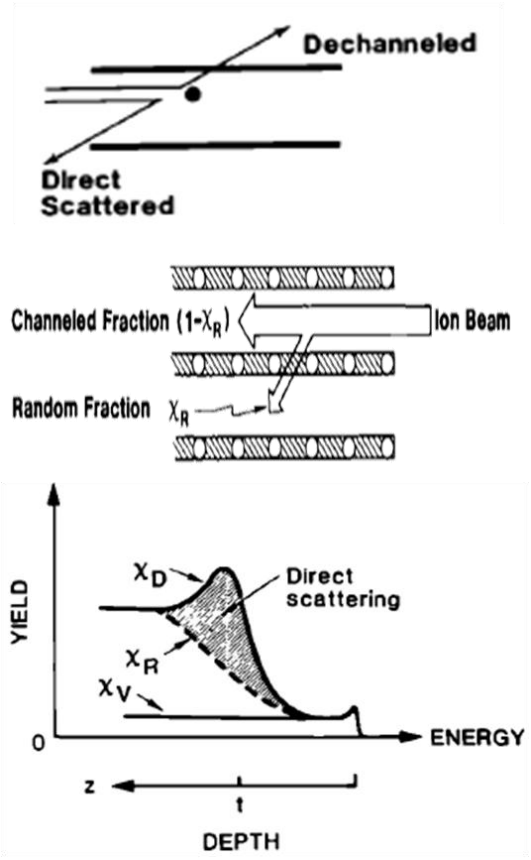

Fig. 2.9. Illustration of the dechanneling mechanism by point defects. [Feldman, Materials Analysis by Ion Channeling, 1982]

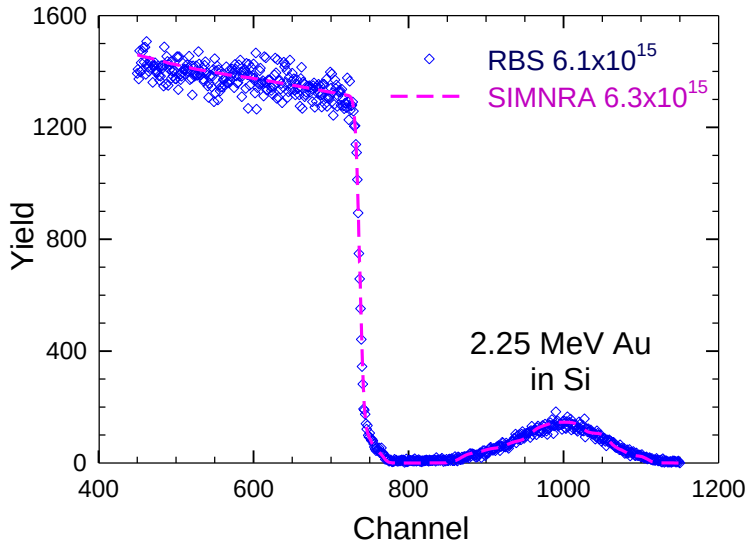

Fig. 2.10. RBS spectrum of Si implanted with 2.25 MeV Au^{2+} ions to an intended fluence of 6.1×10^{15} cm^{-2}. The measured spectrum is fit using SIMNRA, indicating 6.3×10^{15} cm^{-2} as the actual implanted fluence. [Zhang et al, New ion beam materials laboratory for materials modification and irradiation effects research, Nucl. Instr. Meth. Phys. Res., Sect. B, 2014]

CHAPTER 3

ELECTRONIC STOPPING POWERS FOR HEAVY IONS IN SIC AND SIO_2

Abstract

In this chapter, ToF-ERDA technique is utilized to measure the energy loss of heavy ions (i.e. Cl, Br, I, and Au) in SiC and SiO_2 thin foils, and the electronic stopping powers are derived over the energy regime from 0 to 15 MeV. Compared with the experimental results, significant deviations from the SRIM predictions are observed, especially for I and Au ions. For experimental validation, the implanted Au ion distributions with energies from 700 keV to 15 MeV in SiC are measured using RBS and SIMS. The measured results agree well with the predictions based on our derived electronic stopping power values, and confirm overestimation of electronic stopping power from the SRIM predictions.

3.1 Introduction

Accurate information on energy transfer from energetic ions to materials is essential for fundamental research, electronic and optical device fabrication, and prediction of the performance of materials subject to high irradiation environments.[1-13]

As important materials used in electronic devices, SiO_2 and SiC are often subjected to ion implantation, which is a key technique to selectively introduce dopants to modify electronic properties.[5-7] Accurate information of electronic stopping power is fundamental to precise control of dopant concentrations over well-defined depth distributions. MeV heavy ions have recently been applied to produce ion tracks in SiO_2/Si systems that can be etched to form nanostructures in thin films for microelectronic devices or waveguide applications, and the electronic stopping power is an important input in the inelastic thermal spike model[3,14] to predict the track radii.

Reliable performance under energetic ion bombardments is also critical for advanced electronic devices used in space exploration, where a large variety of energetic particles, from protons to very heavy ions, may interact with the electronic components. Single ion events induced by the electronic energy deposition from heavy ions can be a hazard for information storage in microprocessors and memory elements, and may lead to destructive burnout and rupture of gate dielectrics in power devices. Accurate knowledge

on electronic stopping power and a correct model of materials response to energetic charged particles are the scientific foundation to evaluate the survival of advanced electronics to single ion events.[11-13]

In addition, due to the excellent chemical, physical and mechanical properties, SiC is widely considered for use in advanced nuclear energy systems. For example, SiC is proposed as a structural layer in the tri-structural isotropic coated fuel (TRISO) to retain the fission products;[15,16] While not a nuclear material, SiO_2 is the major component of borosilicate glasses proposed for the immobilization of nuclear waste from advanced nuclear fuel cycles.[8,9] In such nuclear applications, these materials are exposed to extreme radiation environments.[8-10] Due to high damage rates, very heavy ions, such as Au, are commonly used to simulate damage evolution induced by radiation in extreme nuclear radiation environments.[17,18] Models of nuclear materials performance rely highly on accurate electronic stopping power data.

As discussed in detail in chapter 1, despite intense studies on the stopping of ions in matter over the past century, electronic stopping power, especially for slow heavy ions in targets with light elements, has not been adequately understood and described. Current theories and models provide significantly inconsistent predictions, and experimental results have shown large error in prediction of ion range and damage profile based on the SRIM predicted electronic stopping power. Due to the long-standing challenge in direct stopping measurement for very heavy ions in low energy regime, reliable data with experimental validation of electronic stopping power for slow heavy ions in light compounds are lacking.

In this chapter, electronic stopping powers for Cl, Br, I, and Au ions are experimentally determined in SiC and SiO_2, based on the single ion technique. An effective nuclear stopping power correction to the data analysis is discussed and validated. For experimental validation, RBS and SIMS are utilized to measure the depth profiles of implanted Au ions in SiC for energies from 700 keV to 15 MeV. In addition, an early version of the TRIM code is modified to incorporate our suggested electronic stopping

power values, and this M-TRIM code is used to predict ion profiles. The measured results and the predictions from the modified code are compared.

3.2 Experimental

The energy loss of the ions penetrating the stopping foils are measured using the ToF-ERDA system, as described in Sec. 2.1. Data analysis procedures are mostly introduced in Sec. 2.1, while the correction of effective nuclear energy loss is described separately in Sec. 2.2. The ion distributions are measured using RBS and ToF-SIMS, as described in Sec. 2.4.

3.3 Electronic stopping power values

Mean electronic stopping powers for heavy ions, after the correction for the effective nuclear energy loss, in SiC and SiO_2 are summarized in Fig. 3.1. The trend lines can be well described over a wide range by the following expression:

$$\frac{dE}{dx} = \frac{a_0+a_1\times E+a_2\times E^2+a_3\times E^3}{a_4\times E+a_5\times E^2+a_6\times E^3} \tag{3.1}$$

Due to the lack of reliable experimental data currently available and the large disagreements between the existing theoretical predictions, the fitting parameters and the corresponding energy regions are listed in Table 1 for convenient implementation in other applications. The coefficients for He are also included.

For Cl ions, SRIM prediction underestimates electronic stopping power at energies higher than 200 keV/u for both materials. Below this energy, the measured data agree well with or are slightly lower than the SRIM prediction. This result follows the trend for lighter ions observed previously: it has been found[19] that for O, F, and Si ions in SiO_2, SRIM prediction provides reasonable estimates or slight overestimates at lower energies, while noticeably underestimating at higher energies. This trend appears more obvious for heavier ions. For example, Si ions have a similar trend as that of Cl ions. For Br ions, underestimation of the SRIM prediction is more significant.

For I ions, especially in SiO_2, the deviation from the SRIM prediction is unexpectedly large. The results from LSS theory and a prediction based on the reciprocity theory[20] are included in Fig. 3.2 for comparison. Even though the LSS formula is normally treated as a crude estimation of electronic stopping power in the low energy regime,[20,21] it is clear from Fig. 3.2 that both LSS and reciprocity predictions agree to each other up to 40 keV/u, and they are smoothly extended to the measured data at ~40 keV/u. In the low energy regime, SRIM also agrees with the other two theoretical predictions. The unexpected curvature shown at ~20 keV/u may be attributed to improper fitting parameters.

For Au ions, SRIM prediction overestimates electronic stopping power in the low energy regime in both targets, and slightly underestimates at higher energy region in SiO_2. Detailed discussion on Au stopping power is provided in Sec 3.4. The stopping data for heavier ions have higher statistical variation, which is clearly observable in Fig. 3.1. Raw data of the Time-Energy correspondence of He, Cl and Au ions are shown as contour maps in Fig. 3.3. As expected, the broadening with increasing ion mass is significant. Besides the lower counting statistics to avoid heavy-ion damage in the Si detector, one important contribution is the intrinsic energy loss straggling of heavier ions, in both the Si detector and the stopping foil. The energy loss straggling is qualitatively described by Bohr's equation[22]:

$$\Omega_B^2 = 4\pi Z_1^2 e^4 Z_2 N \,, \tag{3.2}$$

where Z_1 and Z_2 are the projectile and target atomic numbers, respectively, e is the electronic charge and N is the target atomic density. According to Eq. 3.2, the straggling increases significantly with increasing ion masses.

3.4 Ion range and ion distribution

Quick calculation of the projected ion range R_p for heavy ions in the energy range of this study is based on the method developed by Lindhard and coworkers[23] that:

$$R_p = \frac{R}{1+(M_2/3M_1)}, \tag{3.3}$$

where M_1 and M_2 are the masses of the projectile and target atoms, respectively, and R is the total ion path:

$$R = \int_0^R dx = \frac{1}{N}\int_0^{E_1} \frac{dE}{[S_n(E)+S_e(E)]}. \tag{3.4}$$

In order to calculate R, the nuclear stopping power S_n is obtained from the SRIM code. For electronic stopping power S_e, we derive new values shown in Fig. 3.4. Our measured data are used for the high energy range (≥ 30 keV/u). The reciprocity theory prediction, which has been regarded as working well in the low energy region, is used in the low energy regime (≤ 5 keV/u). An extrapolation (dash line) from 5 to 30 keV/u is made to smoothly connect the measured data and the reciprocity theory prediction. The abnormal curvature change (> 5 keV/u range) in the reciprocity curve is abandoned. The prediction from LSS theory is also shown in Fig. 3.4. The large disagreement between different predictions further indicates the necessity of careful stopping measurements and experimental validations.

Experimentally measured and theoretically predicted ion ranges for Au ions in SiC with different energies are shown in Fig. 3.5. Experimentally, the depth profiles of the implanted Au ions are measured by both RBS and SIMS. The ion ranges are calculated from the fitted curves as

$$R_p = \sum R_i n_i / N, \tag{3.5}$$

where n_i is the number of ions with the range of R_i, and N is the total number of ions. It should be mentioned that the density issue needs to be considered before making a quantitative comparison of ion ranges between different techniques and the theoretical predictions. For convenient comparison, theoretical density of virgin SiC (3.21 g/cm^3) is applied in both the RBS data analysis and the SRIM simulations in this study. As a result, the SIMS profiles need to be corrected for the volume swelling[24,25] due to the amorphization after the high-fluence (up to ~5×10^{15}/cm^2) heavy ion irradiation. 15%

volume swelling is observed in this study, which agrees with the previous studies.[24,25] Theoretically, the ion ranges are calculated based on nuclear stopping power predicted by SRIM and electronic stopping powers derived in this study.

Our predicted results agree well with the experimental results, while SRIM clearly underestimates the ion ranges. The largest errors (~23%) for the SRIM calculations appear between 2 and 5 MeV (see inset of Fig. 3.5), because the nuclear stopping power dominates at lower energies and the error of electronic stopping power reduces at higher energies.

A more intuitive and accurate method to validate the electronic stopping power, especially for the extrapolation region, is to directly compare the ion distribution profiles between experimental results and simulated results using our derived electronic stopping powers. The current SRIM code is not an open-source program, and it doesn't allow users to input their own electronic stopping power values. The original version TRIM-85[26] is, however, an open source code. We have modified the source code of TRIM-85 to include our derived stopping power values. This M-TRIM code is used to predict the profiles of implanted ion distribution. Based on the Monte-Carlo process in the TRIM code, the electronic stopping power is a direct input and can be modified independently, while the nuclear stopping power is indirectly determined by the binary collision processes between each free-flight-path using the Universal Potential. Comparing TRIM-85 and the current version of SRIM, the electronic stopping power has been replaced and the nuclear stopping power has been modified by changing the parameters in the empirical formulas. However, the core concept of TRIM has remained unchanged and considered to be reliable over the years.

In order to compare the ion range with different electronic stopping powers, the electronic stopping power used in TRIM-85 is replaced by either the values from the current SRIM code or the values derived in this study (Fig. 3.4, trend line). By using the current SRIM electronic stopping power, the nuclear stopping parameters in the M-TRIM code are adjusted such that the ion-distribution profiles overlap with current SRIM predictions. Since this nuclear stopping power provides results equivalent to the current

SRIM code, it is used in M-TRIM and named "equivalent" SRIM nuclear stopping power. This equivalent nuclear stopping power is then kept unchanged, and the electronic stopping powers derived by this study are used in the M-TRIM code to predict ion distributions for comparison with the experimental results. For Au energies of 1, 7 and 12 MeV, comparisons between SRIM predictions, RBS results, density corrected SIMS results, and new M-TRIM predictions using both SRIM stopping powers and our derived stopping powers are shown in Fig. 3.6. With the equivalent SRIM nuclear stopping power and the SRIM electronic stopping power, the M-TRIM predicted ion distributions overlap with the SRIM predictions. However, with equivalent SRIM nuclear stopping power and our derived electronic stopping power, the M-TRIM predicted ion distributions agree well with the experimental results. The 1 MeV results indicate the reliable prediction by the reciprocity theory for energies below 5 keV/u. The 7 MeV results indicate that the extrapolation proposed in the present study is reasonable, and the 12 MeV results validate the stopping power measurements.

The use of reciprocity theory relies on the accurate stopping data for light ions (given by SRIM, in this work). Although, as stated in chapter 1, SRIM usually provides reasonable predictions of the electronic stopping power for light ions, some previous evidence (both theoretical and experimental) indicates an underestimate of the electronic stopping power for C ions in Au (see the stopping data plot for C on Au in Paul's database)[27] for ion energies larger than 5 keV/u. This may explain why the reciprocity prediction deviates from our derived values over 5 keV/u.

Since nuclear stopping power dominates in the low energy region, even a small difference in ion range corresponds to a large error in electronic stopping power. Using 1 MeV Au in SiC as an example, the SRIM prediction on ion range is only 20% lower than the experimental result, but its prediction of electronic stopping powers are 2.5 times larger than the our derived values. As a comparison, the range error for energies larger than 10 MeV Au is mainly from the accumulation of electronic stopping power error in lower energy range, while the SRIM prediction on stopping power for the higher energy region seems reasonable.

The Au-SiC system is one of the extreme cases among the ion-target combinations investigated in this work, because Au is the heaviest ion used. In this case, the direct measurement of electronic stopping power and the theoretical prediction are linked together, and the new stopping power values have been successfully crosschecked with depth profiles. The same approach and strategy demonstrated in this work can be used to develop new stopping power curves for other ion-target combinations.

3.5 References

1 A. Molvik, H. Kollmus, E. Mahner, M. Covo, M. Bellachioma, M. Bender, F. Bieniosek, E. Hedlund, A. Krämer, J. Kwan, O. Malyshev, L. Prost, P. Seidl, G. Westenskow, and L. Westerberg, Phys. Rev. Lett. **98** (2007).

2 M. Backman, F. Djurabekova, O. H. Pakarinen, K. Nordlund, and M. Toulemonde, MRS Proceedings **1264**, 5 (2011).

3 M. Toulemonde, W. J. Weber, G. Li, V. Shutthanandan, P. Kluth, T. Yang, Y. Wang, and Y. Zhang, Phys. Rev. B **83**, 054106 (2011).

4 Y. Zhang and W. J. Weber, Phys. Rev. B **82**, 075202 (2010).

5 J. B. Casady and R. W. Johnson, Solid-State Electronics **39**, 1409 (1996).

6 C. Raynaud, J. Non-Crystal. Solids **280**, 1 (2001).

7 D. Wesch, D. Kabelitz, K. Friese, and K. Pechhold, Eur. J. Immunol. **26**, 557 (1996).

8 W. J. Weber, R. C. Ewing, C. R. A. Catlow, T. D. de la Rubia, L. W. Hobbs, C. Kinoshita, H. Matzke, A. T. Motta, M. Nastasi, E. K. H. Salje, E. R. Vance, and S. J. Zinkle, J. Mater. Res. **13**, 1434 (1998).

9 W. J. Weber, A. Navrotsky, S. Stefanovsky, E. R. Vance, and E. Vernaz, MRS bulletin **34**, 46 (2009).

10 T. Nozawa, T. Hinoki, A. Hasegawa, A. Kohyama, Y. Katoh, L. L. Snead, C. H. Henager, and J. B. J. Hegeman, J. Nucl. Mater. **386-388**, 622 (2009).

11 N. V. Kuznetsov, R. A. Nymmik, and N. M. Sobolevsky, Adv. Space Res. **30**, 985 (2002).

12 S. Duzellier, Aerospace Science and Technology **9**, 93 (2005).

13 Y. Zhang and W. J. Weber, Nucl. Instrum. Methods Phys. Res. B **267**, 1705 (2009).

14 A. Dallanora, T. L. Marcondes, G. G. Bermudez, P. F. P. Fichtner, C. Trautmann, M. Toulemonde, and R. M. Papaléo, J. Appl. Phys. **104**, 024307 (2008).

15 Y. Katoh, L. L. Snead, I. Szlufarska, and William J. Weber, Curr. Opin. Solid State Mater. Sci. **16**, 143 (2012).

16 H. Y. Xiao, Y. Zhang, L. L. Snead, V. Shutthanandan, H. Z. Xue, and W. J. Weber, J. Nucl. Mater. **420**, 123 (2012).

17 J. C. Dran, Solid State Phenomena **30-31**, 367 (1992).

18 Y. Zhang, J. Lian, C. Wang, W. Jiang, R. Ewing, and W. Weber, Phys. Rev. B **72**, 094112 (2005).

19 Y. Zhang, W. J. Weber, D. E. McCready, D. A. Grove, J. Jensen, and G. Possnert, Appl. Phys. Lett. **87**, 104103 (2005).

20 P. Sigmund, Euro. Phys. J. D **47**, 45 (2008).

21 M. Zeb, J. Kohanoff, D. Sánchez-Portal, A. Arnau, J. Juaristi, and E. Artacho, Phys. Rev. Lett. **108**, 225504 (2012).

22 N. Bohr, Mat. Fys. Medd. Dan. Vid. Selsk **18** (1948).

23 J. Lindhard, V. Nielsen, and M. Scharff, Mat. Fys. Medd. Dan. Vid. Selsk **36**, 3 (1968).

24 I. T. Bae, W. J. Weber, and Y. Zhang, J. Appl. Phys. **106**, 123525 (2009).

25 C. J. McHargue and J. M. Williams, Nucl. Instrum. Methods Phys. Res. B **80-81**, 889 (1993).
26 J. F. Ziegler, J. P. Biersack, and U. Littmark, *The stopping and range of ions in solids*. (Per-gamon Press, New York, 1985).
27 H. Paul, (https://www-nds.iaea.org/stopping/, 2012).

Appendix 3.1

TABLE 3.1. Fitting coefficients [Eq. 3.1] to the stopping data (keV/(μg/cm^2)) for the corresponding validating energy (keV/u) region. [Jin et al, Electronic stopping powers for heavy ions in SiC and SiO_2, J. Appl. Phys., 2014]

(a) Ions in SiC

Ions	Au	I	Br	Cl	He**
E_{min} (keV/u)	30*	40	40	80	120
E_{max} (keV/u)	70	120	250	500	500
a_0	-3.676×10^{1}	1.464×10^{2}	4.672×10^{1}	-1.707×10^{6}	-8.479×10^{2}
a_1	1.512×10^{3}	-1.783×10^{3}	-4.239×10^{2}	4.696×10^{4}	8.808×10^{2}
a_2	7.681×10^{2}	2.773×10^{3}	6.424×10^{2}	-1.444×10^{3}	1.326×10^{2}
a_3	1.486×10^{1}	2.520×10^{2}	1.071×10^{2}	2.495×10^{1}	2.373×10^{-2}
a_4	2.453×10^{3}	-5.985×10^{2}	-2.520×10^{2}	-7.466×10^{3}	2.961×10^{3}
a_5	8.979	1.153×10^{3}	5.386×10^{2}	1.123×10^{2}	4.649×10^{1}
a_6	1.191	4.778	1.754	9.061×10^{-1}	1.547×10^{-1}

(b) Ions in SiO_2

Ions	Au	I	Br	Cl	He**
E_{min} (keV/u)	30*	40	40	80	120
E_{max} (keV/u)	70	120	250	500	500
a_0	-6.253	1.091×10^{2}	1.019×10^{2}	-1.707×10^{6}	-7.238×10^{1}
a_1	4.786×10^{1}	6.833×10^{1}	-6.689×10^{2}	4.696×10^{4}	7.042×10^{1}
a_2	2.550×10^{1}	1.840×10^{2}	4.967×10^{2}	-1.444×10^{3}	9.492
a_3	-2.224×10^{-1}	5.359	6.961×10^{1}	2.495×10^{1}	-4.260×10^{-4}
a_4	7.468×10^{1}	2.206×10^{2}	-3.976×10^{2}	-7.466×10^{3}	2.699×10^{2}
a_5	-9.011×10^{-2}	3.517×10^{1}	3.961×10^{2}	1.123×10^{2}	3.316
a_6	-2.827×10^{-3}	3.464×10^{-2}	9.580×10^{-1}	9.061×10^{-1}	8.539×10^{-3}

* For Au ions, the extrapolation allows the E_{min} down to 1keV/u.

**The validating energy ranges listed are based on the measurement; Eq. (3.1) with these coefficients fits the SRIM value well for energies from 0 to over 800 keV/u.

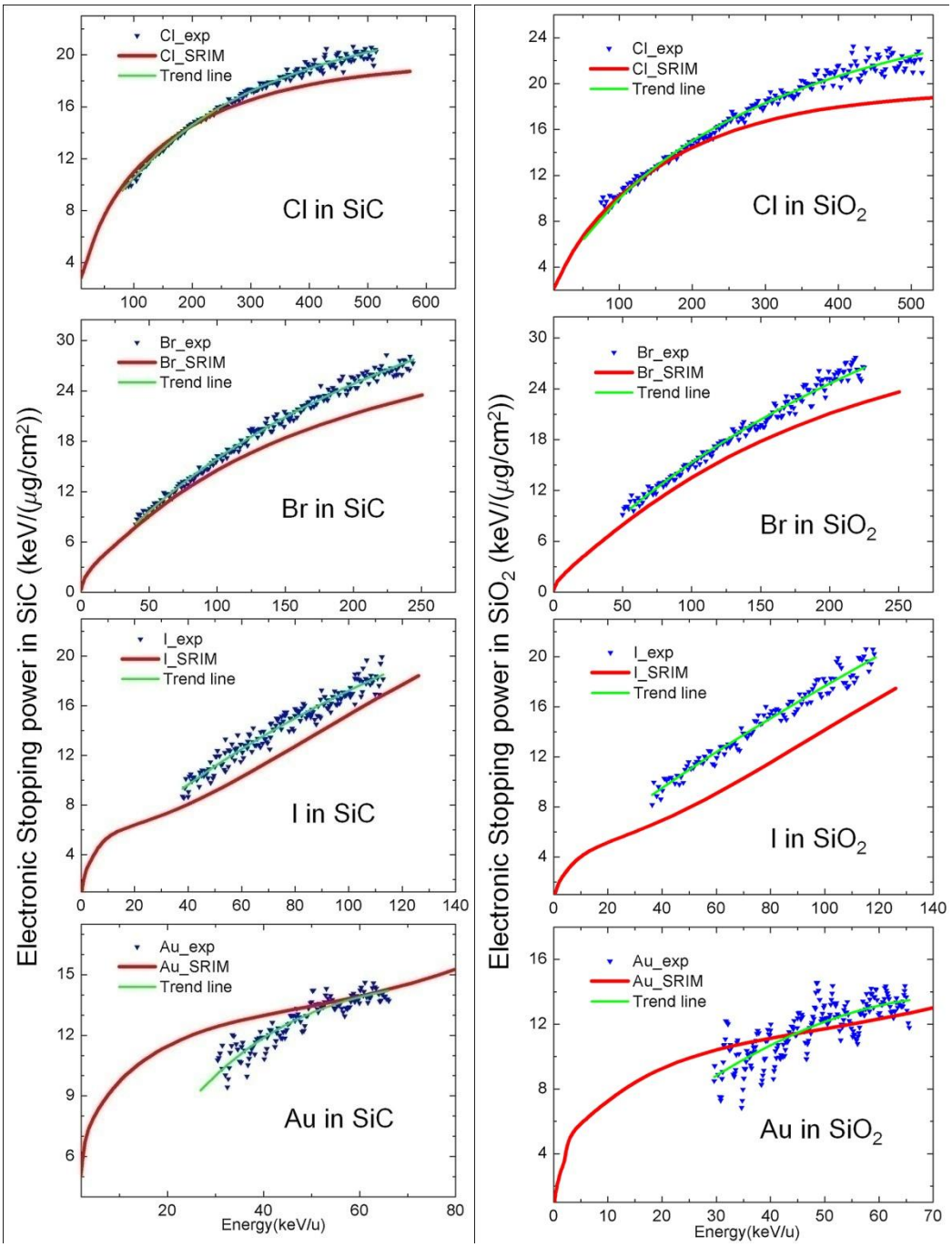

Fig. 3.1. Measured mean electronic stopping power of Cl, Br, I and Au ions in SiC (left) and SiO_2 (right) with the trend lines (Eq. 3.1) and the SRIM predictions. [Jin et al, Electronic stopping powers for heavy ions in SiC and SiO_2, J. Appl. Phys., 2014]

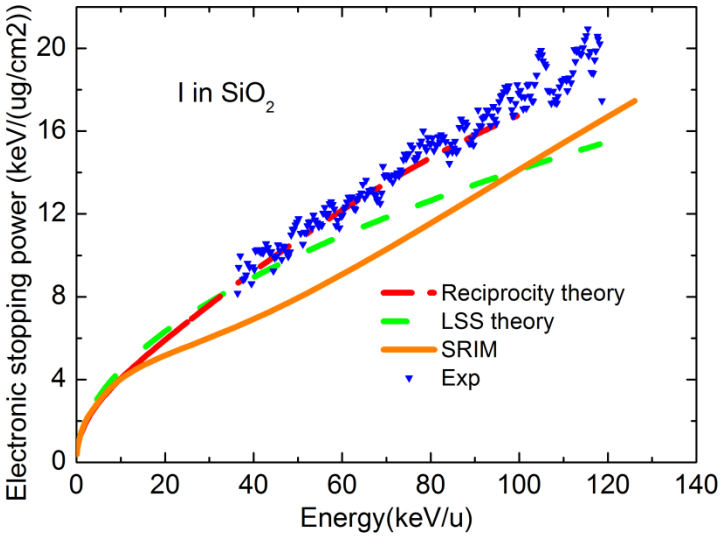

Fig. 3.2. Comparison of the electronic stopping power for I ions in SiO_2 between the measured data and the predictions by LSS theory, reciprocity theory and SRIM. [Jin et al, Electronic stopping powers for heavy ions in SiC and SiO_2, J. Appl. Phys., 2014]

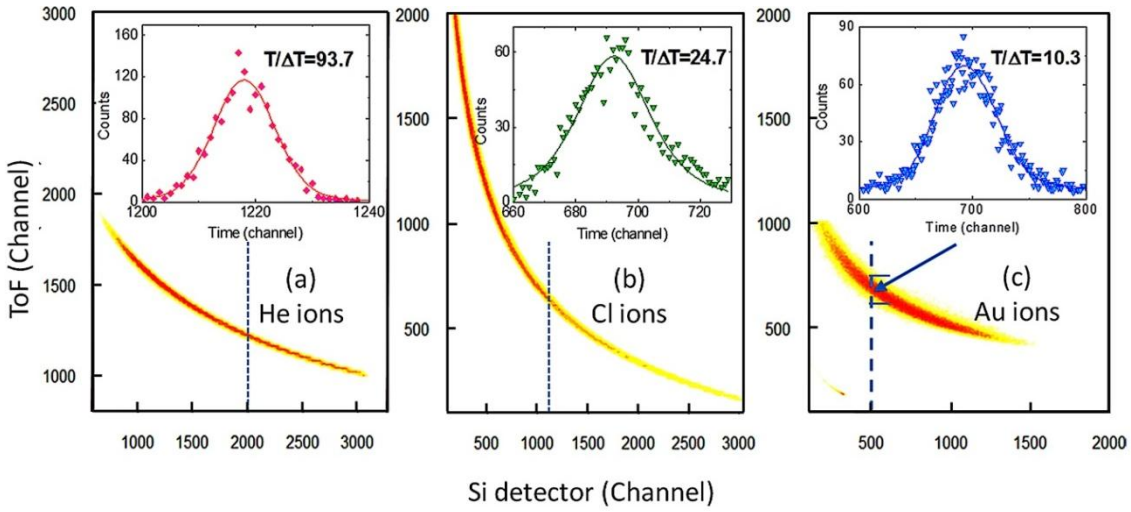

Fig. 3.3. Contour map of the Time-Energy correspondence for (a) He, (b) Cl, and (c) Au ions penetrating through the SiC stopping foils. ToF (channel) represents the energy before penetration; Si detector (channel) represents the energy after the penetration. The point density is represented in logarithmic scale. The insets are the time (corresponding to energy) distribution profiles for each selected Si detector channel (shown as vertical lines). It is clear that lighter ions have much better time (energy) resolution. [Jin et al, Electronic stopping powers for heavy ions in SiC and SiO_2, J. Appl. Phys., 2014]

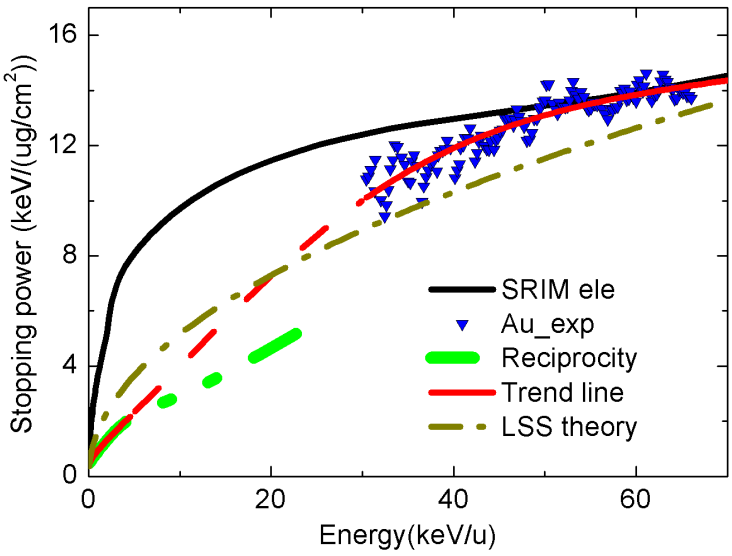

Fig. 3.4. Comparison between the measured data and the SRIM, LSS theory and reciprocity theory predicted electronic stopping powers for the Au ions in SiC. The red line is our derived trend line (Eq. 3.1). The solid line parts are the measured data (> 30 keV/u) or reciprocity predicted (<5 keV/u). The dash line is the extrapolation for connection between 5-30 keV/u. [Jin et al, Electronic stopping powers for heavy ions in SiC and SiO_2, J. Appl. Phys., 2014]

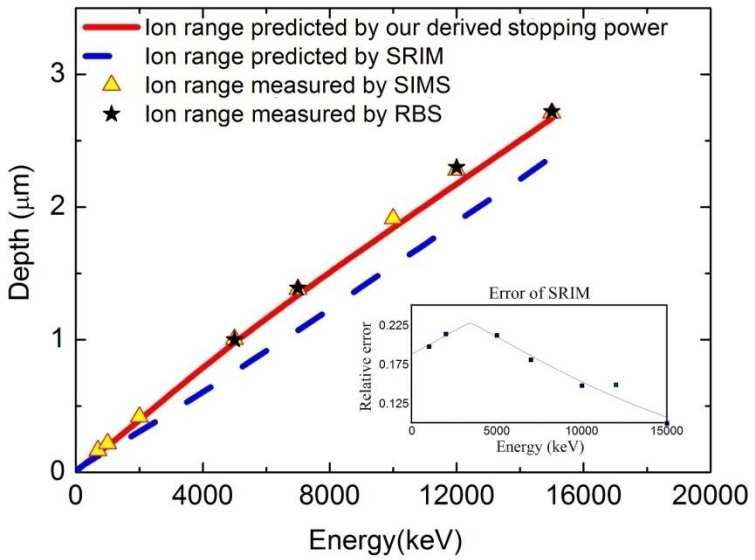

Fig. 3.5. Ranges of Au ions with different energies in SiC measured by SIMS (triangle) and RBS (star) as well as ion ranges predicted by SRIM (dash line) and this study (solid line). The SIMS results are the density corrected values assuming the 15% volume swelling. The inset shows the relative deviation between SRIM predictions and experimental results. [Jin et al, Electronic stopping powers for heavy ions in SiC and SiO_2, J. Appl. Phys., 2014]

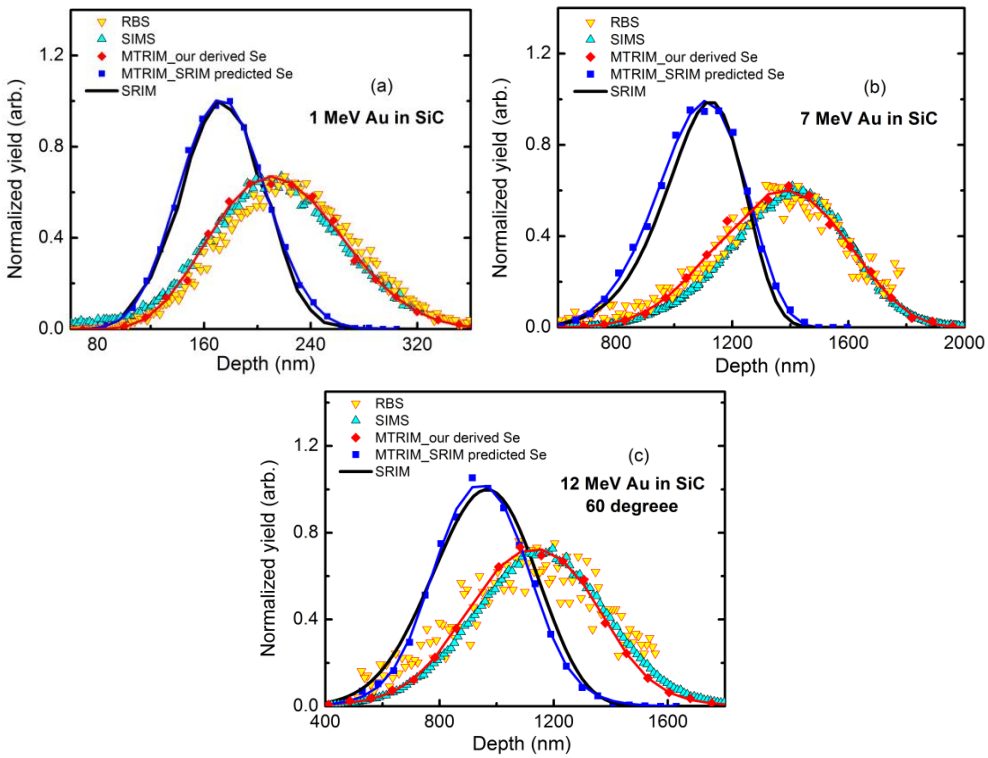

Fig. 3.6. Comparisons of ion distribution profiles for (a) 1, (b) 7, and (c) 12 MeV Au in SiC with measurements (RBS and SIMS), SRIM and M-TRIM predictions. [Jin et al, Electronic stopping powers for heavy ions in SiC and SiO_2, J. Appl. Phys., 2014]

CHAPTER 4

ANGULAR DISTRIBUTION AND RECOIL EFFECT FOR 1 MEV AU IONS THROUGH A SI_3N_4 THIN FOIL

Abstract

In this chapter, ToF-SIMS is utilized to determine the angular distribution of 1 MeV Au ions after penetrating a Si_3N_4 foil with a thickness of ~100 nm. The exiting Au ions are collected by a Si wafer located ~14 mm behind the Si_3N_4 foil, and the resulting 2-dimensional distribution of Au ions on the Si wafer is measured using ToF-SIMS. The SRIM-predicted angular distribution of Au ions through the Si_3N_4 thin foil is compared with the measured results, indicating that SRIM predicts reasonably the nuclear stopping power within 10% uncertainty. In addition, thickness reduction is observed in the suspended Si_3N_4 foils induced by 1 MeV Au ion irradiation.

4.1 Introduction

Transmission setups have been developed to directly measure electronic stopping power.[1-3] The energy of ions before and after penetrating a thin foil is measured to determine the energy loss. Electronic stopping power can be determined directly by this method for light ions (H, He) and medium heavy ions (C, Si and etc.). For very heavy ions,[3] however, nuclear energy loss is not negligible, and must be subtracted from the measured values in order to determine the electronic stopping power. Due to the restriction of the collimator placed in front of the Si detector (as shown in Fig. 2.1), only part of the ions within a certain scattering angle can be detected. In order to accurately determine electronic stopping power, reliable predictions of scattering angle and nuclear stopping power are critically important. Furthermore, due to difficulties to make very thin stopping foils (such as below 100 nm), in the lower energy regime (e.g., < 5 MeV), where the electronic stopping powers predicted by SRIM have been shown to have larger errors, the current transmission setup is not able to directly measure the stopping power. As an alternative approach, by measuring ion profiles at different ions energies, total stopping power (nuclear plus electronic stopping power) can be derived. With accurate information of nuclear stopping power, the electronic stopping power can be reasonably estimated.[3]

The SRIM code has been widely used to predict the scattering process and the nuclear stopping power for decades.[4,5] However, the predicted nuclear stopping powers of slow heavy ions may be overestimated due to the assumption of neutral atoms.[6] Direct experimental validation of SRIM predicted nuclear stopping power and scattering angles, especially for very heavy ions in low energy regime, is insufficient. Recently, the reliability of SRIM predicted nuclear stopping power for slow heavy ions has been questioned,[6] which makes direct measurement of angular scattering distributions critically important.

Historically, position-sensitive detectors were used to measure the angular distribution of light ions and medium heavy ions.[7] However, conventional detectors (i.e. Si detector) are problematic for measuring very heavy ions.[8-10] A time-of-flight spectrometer that could be continuously rotated was used to measure the angular distribution of Bi ions with 0.8 Bohr velocity though a C foil.[11] Unfortunately, this is not a standard instrument for most ion beam laboratories.

In this chapter, a new method is developed to measure the angular distribution of 1 MeV Au ions through a Si_3N_4 thin foil using ToF-SIMS. In addition, thickness of the suspended Si_3N_4 foils under ion irradiation is measured as a function of ion fluence by ToF-SIMS, SEM and TEM.

4.2 Experimental

The experimental design and procedure are described in Sec. 2.3.

4.3 Irradiation induced thinning of Si_3N_4 foils

The lateral distributions of scattered Au ions implanted into a Si wafer with different fluences are shown in Fig. 4.1. Gaussian distributions are applied to fit the curves. Apparently, the distributions become narrower with increasing ion fluence. This trend is due to the thickness reduction of the suspended Si_3N_4 foils under ion irradiation.

ToF-SIMS is used to measure the thickness of both window and supported regions of each foil upon irradiation to different ion fluences. The measured thickness of a

suspended foil by ToF-SIMS is always slightly smaller than the actual value, as the foil will break under sputtering when it is thinner than a certain value. In order to minimize this error, a virgin window is tested and the results are shown in Fig. 4.2 (a). The measured thickness of window region is ~3 nm less than that of the supported region, which indicates that the foil is broken under the sputtering condition when it is thinner than 3 nm. Figs. 4.2 (b) and (c) show the thickness differences between the window region and the supported region of the foils under 1 MeV Au irradiation with 1×10^{15} and 2×10^{15} cm^{-2}. After 1×10^{15} cm^{-2} irradiation, the window region is 15 nm thinner than the virgin film (supported region). Considering the ~3 nm critical thickness, the film was thinned by ~12 nm during the irradiation (from 101 nm to ~89 nm). The window region after 2×10^{15} cm^{-2} irradiation is 27 nm thinner than the virgin region, which means the foil was thinned by ~24 nm during the irradiation (from 99 nm to ~75 nm). The decrease in thickness is proportional to ion fluences and the loss rate under this irradiation condition is ~112 atom/ion. The foil was completely destroyed after 1×10^{16} cm^{-2} irradiation, which also supports this trend.

Although ToF-SIMS depth profiling measurements are simple and the above results seem straightforward, the uncertainty of the "critical foil thickness to break" in ToF-SIMS is a potential problem. To confirm the results from the ToF-SIMS measurements, SEM and TEM are used to investigate this thinning effect. Another virgin sample and a set of samples irradiated with 1×10^{15} and 2×10^{15} cm^{-2} Au ions were prepared for the microscopy measurement. SEM is employed to measure the thickness of the window region of each sample, and the results are shown in Fig. 4.3 (a-c). TEM is employed to measure the thickness of the corresponding supported film of each sample, and the results are shown in Fig. 4.3 (d-f). For the virgin sample, the TEM measured thickness of the virgin region is 102.8 nm; the SEM measured window thickness of the region is 102 nm. For the sample under the 1×10^{15} cm^{-2} irradiation, the virgin region is 95.2 nm thick, while the window region is 84 nm. For the sample under the 2×10^{15} cm^{-2} irradiation, the virgin region is 100.8 nm thick, while the window region is 78 nm. The results clearly show that the thickness of the suspended Si_3N_4 foil is decreased by 11.2 nm under the 1×10^{15} cm^{-2}

irradiation, and by 22.8 nm under the 2×10^{15} cm^{-2} irradiation. The measured change in thickness is also proportional to the ion fluence, and the loss rate is ~102 atom/ion. This value is only slightly smaller (9%) than the ToF-SIMS results, which is within uncertainty range of all the measurements.

Further measurements by ToF-SIMS show that the thickness change of the supported film under the same irradiation conditions is negligible compared to the window region (less than 1.5 nm under 1×10^{15} cm^{-2} irradiation). This result reveals that the sputtering effect on the front surface (the surface facing the incoming beam) is negligible for 1 MeV Au ion perpendicular irradiation; the change in thickness is predominately due to the forward recoils from the back surface of thin foils, similar to the electron beam drilling reported by previous work.[12]

4.4 Angular distribution of scattered ions

Comparisons between the measured angular distribution of scattered ions and the SRIM simulated results are shown in Fig. 4.4 for the fluence of 1×10^{15} and 2×10^{15} cm^{-2}. The deflection angles are determined by the radius in the Si wafer and the distance between the Si wafer and the Si_3N_4 foil (14.2 mm). Considering the thickness change of the foils, the average thicknesses before and after the irradiations (95 nm for 1×10^{15} cm^2 and 87 nm for 2×10^{15} cm^{-2}) are used in the SRIM simulation. The distribution for the irradiation fluence of 1×10^{16} cm^{-2} is not compared with SRIM, because the foil is totally destroyed and thus the average thickness cannot be identified. The error bars in Fig. 4.4 are mainly attributed to the background signal and the uncertainty in mass window selection during the SIMS measurement.

For both comparisons, SRIM reasonably predicts the angular distribution; however, the SRIM predicted distribution seems slightly wider than the measured distribution, indicating that SRIM may slightly overestimates the nuclear stopping power for 1 MeV Au in Si_3N_4. Previous experimental studies[11,13] with a different measurement method showed a similar result: for Bi ions at 0.8 Bohr velocity (~4.2 MeV) penetrating through a 13.7 μg cm^{-2} C foil, the SRIM predicted angular distribution is slightly wider than the

measured result. In the comparisons with lighter Ne and Ar ions at the same velocity, these same authors found that the SRIM prediction is in better agreement.[14]

One factor that may lead to this overestimation is that the electronic stopping power for Au ions in compounds containing light elements is significantly overestimated by SRIM.[3] Although the electronic stopping power contributes little to the angular scattering process, the average energy of ions penetrating the foils is underestimated by SRIM, which may cause the overestimation in scattering angles. Another important factor is that, as stated in Ref. [6], in SRIM code: "In all cases of nuclear stopping, it is assumed that the ion is neutral and the target atom is in its normal crystalline state. All these assumptions make for errors, and make the nuclear stopping too large for low energies". The observations in present study provide experimental evidence that supports this statement. Considering the error in electronic stopping power stated above, SRIM predicted nuclear stopping powers may be slightly larger (<10%) than the actual values, which is within the claimed error range by SRIM (18% for all ion-target combinations).[5,6] Further theoretical work is needed to provide more accurate nuclear stopping powers for slow heavy ions.

It should be mentioned that, compared with the previous technique of angular distribution measurements,[11] the method demonstrated in this work can be performed in most accelerator and ToF-SIMS laboratories with no special facility requirement, which can contribute to the development of the stopping database.

4.5 References

1 Y. Zhang, Nucl. Instrum. Methods Phys. Res. B **196**, 1 (2002).
2 Y. Zhang, W. Weber, and C. Wang, Phys. Rev. B **69**, 205201 (2004).
3 K. Jin, Y. Zhang, H. Xue, Z. Zhu, and W. J. Weber, Nucl. Instrum. Methods Phys. Res. B **307**, 65 (2013).
4 J. F. Ziegler, (www.srim.org).
5 J. F. Ziegler, J. P. Biersack, and U. Littmark, *The stopping and range of ions in solids*. (Per-gamon Press, New York, 1985).
6 H. Paul, AIP Conf. Proceedings **1525**, 309 (2013).
7 H. Krause, J. Barrett, S. Datz, P. Dittner, N. Jones, J. Gomez del Campo, and C. Vane, Phys. Rev. A **49**, 283 (1994).
8 H. J. Whitlow and Y. Zhang, Nucl. Instrum. Methods Phys. Res. B **190**, 375 (2002).
9 Y. Zhang and H. J. Whitlow, Nucl. Instrum. Methods Phys. Res. B **190**, 383 (2002).
10 Y. Zhang and W. J. Weber, Phys. Rev. B **82**, 075202 (2010).
11 H. Geissel, W. N. Lennard, H. R. Andrews, D. P. Jackson, I. V. Mitchell, D. Philips, and D. Ward, Nucl. Instrum. Methods Phys. Res. B **12**, 38 (1985).
12 D. G. Howitt, S. J. Chen, B. C. Gierhart, R. L. Smith, and S. D. Collins, J. Appl. Phys. **103**, 024310 (2008).
13 R. N. Sagaidak, V. Utyonkov, and F. Scarlassara, Nucl. Instrum. Methods Phys. Res. A **700**, 111 (2013).

Appendix 4.1

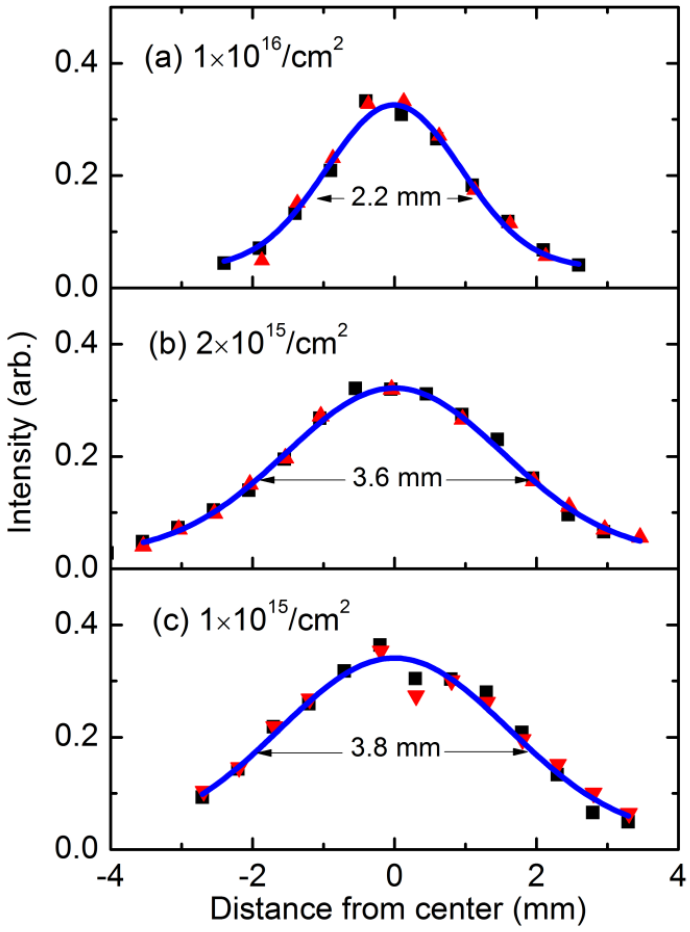

Fig. 4.1. Lateral distributions of the scattered Au ions implanted into the Si wafer with different irradiation fluences: (a) 1×10^{16} cm^{-2}, (b) 2×10^{15} cm^{-2} and (c) 1×10^{15} cm^{-2}. Two types of spots indicate the two perpendicular scans along diameters. [Jin et al, Angular distribution and recoil effect for 1 MeV Au^{+} ions through a Si_3N_4 thin foil, Nucl. Instr. Meth. Phys. Res., Sect. B, 2014]

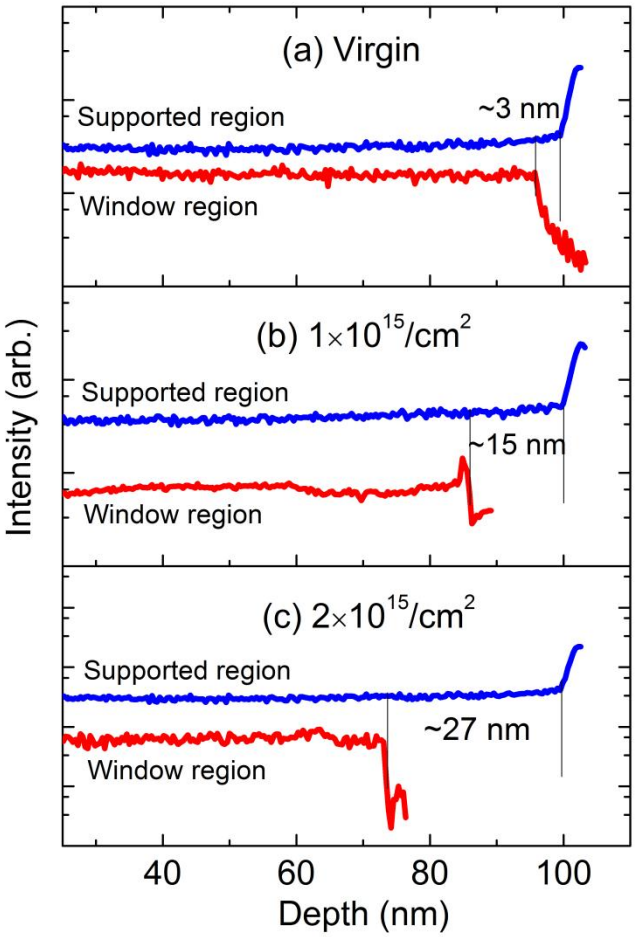

Fig. 4.2. The thickness measured by ToF-SIMS for both window regions (irradiated) and supported regions (virgin) of each sample with different fluences: (a) virgin sample, (b) 1×10^{15} cm^{-2}, and (c) 2×10^{15} cm^{-2}. [Jin et al, Angular distribution and recoil effect for 1 MeV Au^{+} ions through a Si_3N_4 thin foil, Nucl. Instr. Meth. Phys. Res., Sect. B, 2014]

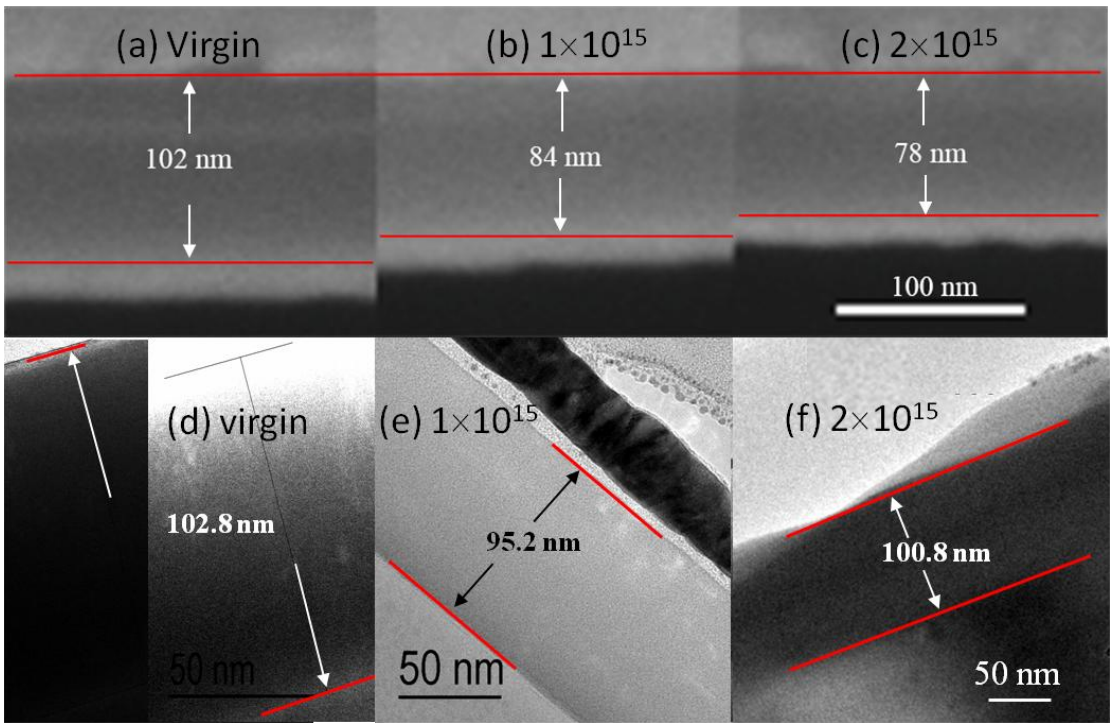

Fig. 4.3. SEM measurements on the thickness of window regions for (a) virgin sample and the samples after (b) 1×10^{15} cm^{-2} and (c) 2×10^{15} cm^{-2} irradiations. TEM measurements on the thickness of the supported regions of these three samples (d-f). In (d), the upper (left) and lower (right) boundaries are determined by adjusting the contrast. [Jin et al, Angular distribution and recoil effect for 1 MeV Au^{+} ions through a Si_3N_4 thin foil, Nucl. Instr. Meth. Phys. Res., Sect. B, 2014]

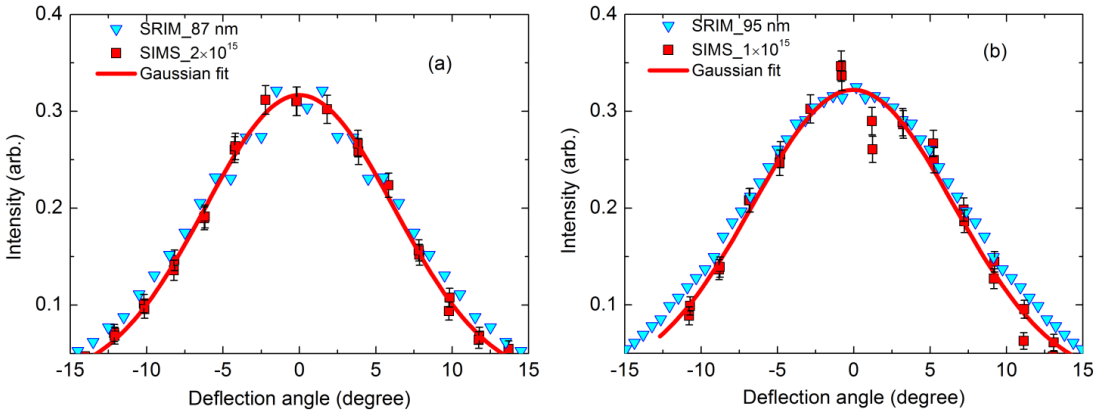

Fig. 4.4. Comparisons between the measurements and the SRIM predictions for the deflection angle of the transmitted ions with fluences of (a) 2×10^{15} cm^{-2} and (b) 1×10^{15} cm^{-2}. [Jin et al, Angular distribution and recoil effect for 1 MeV Au^{+} ions through a Si_3N_4 thin foil, Nucl. Instr. Meth. Phys. Res., Sect. B, 2014]

CHAPTER 5

DEPTH PROFILE OF AU ION IRRADIATION IN SI AND MGO

Abstract

In this chapter, implanted Au ion distributions in Si with energy from 1 to 15 MeV are measured using RBS and SIMS. The electronic stopping powers for Au ions in Si in the corresponding energy regimes are derived based on the measured ion distributions. The results show that SRIM significantly overestimates the electronic stopping power for Au ions in Si in the low energy regime. Such deviation is also observed in the case of Au ion irradiation in MgO. Moreover, significant channeling effects are observed on the ion distributions and damage profiles for Au ion irradiation in MgO along both axial and planar channels.

5.1 Introduction

Experimental determination of electronic stopping power for heavy ions in ceramics containing light elements is highly desired.[1,2] However, due to the experimental difficulties such as the challenge of fabricating uniform, thin and strong foils and the easy oxidation of certain materials, direct measurements of electronic stopping power for slow heavy ions is sometimes challenging. In such cases, alternative approaches providing experimental electronic stopping power values are needed. As discussed in chapter 3, implanted ion profile is directly correlated to the total (electronic + nuclear) stopping power. On the other hand, nuclear stopping power provided by SRIM has been generally considered reasonable[3,4] and it has also been experimentally validated in chapter 4 for 1 MeV Au ions penetrating a Si_3N_4 thin foil. As a result, electronic stopping power can be derived from the ion distributions at different energies.[5]

It has been reported[6-9] that the depth profile of both implanted ions and defects may shift to deeper region if ions are irradiated along low-index axial channels. This channeling effect is often not a concern in the materials that are readily amorphized under ion irradiation (e.g. Si[10] and SiC[11]). This is because measurements of ion distributions usually require relatively high fluences to achieve good statistics, and thus most of the ions travel in amorphous targets. However, in materials that are hardly amorphized under

ion irradiation at room temperature, e.g. MgO,[12-14] such channeling effects must be carefully considered when analyzing the measured ion and damage profiles.

Although the channeling effects of low-energy (tens to hundreds of keV) ion irradiation along axial channels have been extensively studied,[6,7,9] the effects of MeV-ion irradiation along planar channels, especially the effects on damage profile have not drawn adequate attention. This channeling issue cannot be ignored in MgO due to its open rock-salt structure. For example, significantly increased skewness is observed in the implanted ion profiles in MgO in previous studies,[14-16] which is not commonly observed in most other materials of interest (e.g. in Ref. 15, see the comparison between the Fig.1 for MgO and Figs. 2 and 3 for $SrTiO_3$ and $LiNbO_3$, respectively). Previous experimental results[15,17] have demonstrated that the distributions of implanted Au and Ag ions are not changed after 1 hour thermal annealing at 600 °C and 900 °C, respectively, indicating that the asymmetric ion profile is not attributed to the thermal migration of the implanted ions. Instead, it can be reasonably expected that the channeling effect may be the major contribution.

In this chapter, RBS and ToF-SIMS are utilized to measure the implanted Au ion distribution in Si from 1 to 15 MeV. Electronic stopping powers for Au ions in Si are estimated based on the measured ion profiles. In addition, the ion and damage profiles are measured for Au ions irradiated in MgO single crystals along various directions. The channeling effects are studied for the irradiations along axial and planar channels.

5.2 Experimental

The depth profile measurements by both RBS and ToF-SIMS are described in Sec. 2.4. The ion channeling technique is described in Sec. 2.5. The ion irradiation is described in Sec. 2.6.

Specifically in this chapter, Si wafers are implanted with Au ions with energies of 1, 2, 4, 6, 10 and 15 MeV, at the fluence of 5×10^{15} cm^{-2}. He ion with energy of 3.5 MeV is used for RBS measurements. The (100)-oriented (CrysTec, Berlin, Germany) and (110)-oriented (MTI Corporation, Richmond, CA, USA) MgO are implanted with 1 and 4 MeV

Au ions. The fluences are chosen at 5×10^{15} and 1×10^{14} cm^{-2}. The high fluence is used to achieve good statistics of the RBS yield scattered from Au atoms, and the low fluence is used to keep the sample at relatively low damage level to avoid the shift of defect distribution[18,19] (see details in chapter 6). Various irradiation directions are chosen for comparison and will be discussed in detail in Sec. 5.4. In RBS measurements in MgO, 2.0 MeV He ion is used to determine the Au ion distribution, and 3.0 MeV He ion is used to determine the damage profile.

5.3 Electronic stopping power derived from the Au ion profiles in Si

Au ion distributions in Si

Fig. 5.1 shows the SIMS and RBS measured Au ion distributions in Si with energies of 1 and 6 MeV. The SRIM predictions are also shown for comparison. Comparing RBS and SIMS results, a ~3% difference in peak positions is observed. As discussed in chapter 3, this difference is mainly attributed to volume swelling induced by high fluence ion irradiations, which agrees with the previous studies on Si irradiated with Si ions.[20] Considering this volume swelling, the RBS and SIMS measurements agree well with each other, but the SRIM predicted ion distributions for both energies are considerably shallower than the measured results.

The peak positions of the Au ion distributions from 1 to 15 MeV measured by SIMS are shown in Fig. 5.2. The SRIM calculated peak positions and the ion ranges are also plotted for comparison. Theoretical density of pre-irradiated Si, 2.321 g/cm^3, is used in the SRIM calculations for convenient comparison with literatures. Thus, SIMS results are correspondingly corrected by 3% volume swelling for consistency. Due to the slight asymmetry of the ion profiles, peak positions of ion profiles are slightly different from the ion ranges, as shown in Fig. 5.2, but this does not affect the comparisons in this study. It is clearly shown that SRIM underestimates the ranges of implanted Au ions. This result agrees with the study of Au ions in SiC, as demonstrated in chapter 3.

Electronic stopping power for Au ions in Si

The relationship between electronic stopping power and ion ranges is described by Eq. (3.3) and (3.4). According to these equations, the difference in ion ranges (or in the peak positions of ion distributions) between two energies is proportional to the reciprocal of the "average" total stopping power within this energy interval. This relationship has been experimentally demonstrated for Au ions in SiC,[5] in which the ratios of SRIM predicted to measured peak position difference between two energies agree well with the ratios of the measured to SRIM predicted average total stopping power within the corresponding energy intervals. Using this relationship, the "average" electronic stopping power between two adjacent energies can be derived by comparing the measured peak positions of these two energies with the SRIM predictions. Although this is a crude estimate method, it can provide a general trend of the electronic stopping power curve as a function of energy for the ion-solid combinations, in which direct measurement is not available.

Fig. 5.3 shows the electronic stopping powers calculated from the data shown in Fig. 5.2. Nuclear stopping values used in this calculation are SRIM predictions. A smooth curve is made to show the trend. Electronic stopping power curves from the predictions of SRIM and reciprocity theory[21] are also shown for comparison. The results show that SRIM significantly overestimates electronic stopping power in the low energy regime, while SRIM prediction and our derived curve match well at Au energies of ~10 MeV. On the other hand, our derived electronic stopping power curve follows the trend of reciprocity in the low energy regime. The unusual curvature in the reciprocity curve is believed to be an error from SRIM predicted electronic stopping power for Si ions in Au, as discussed in chapter 3.

Comparing our derived curve to SRIM as well as the reciprocity theory predictions, this result agrees well with the case of Au ions in SiC, as shown in Fig. 3.4. This good agreement demonstrates that direct measurement of energy loss and indirect derivation from ion profiles can be used as complementary methods to determine electronic

stopping power. This is beneficial to expand experimental database of electronic stopping power for heavy ions in light targets.

5.4 Channeling effects on Au ion distributions in MgO

Sample stages in ion beam analysis laboratories usually allow rotations along three orthogonal axes, as shown in Fig. 5.4 (a). Figs. 5.4 (b) and (c) show the 2-D angular scans of <100> and <110>-oriented MgO samples mounted on a sample holder with their edges parallel or perpendicular to the rotation axes. Low-index axial and planar channels can be clearly seen in the Figs. 5.4(b) and (c) with the rotations of θ and φ.

Fig. 5.5 (a) shows the depth profiles of 1 MeV Au ions implanted into MgO (100) at a fluence of 5×10^{15} cm^{-2} along different directions, as measured by RBS. The two angle values associated with each ion profile indicate the rotations of samples along θ and φ during implantation (see Fig. 5.4 (a)). The ion profiles are clearly divided into three groups: (0°, 0°), (7°, 0°)/ (7°, 2°), and (7°, 5°)/ (15°, 5°)/ (15°, 7°). These three groups correspond to irradiations along the axial channel, planar channel, and "off-channel" directions, respectively. This result clearly demonstrates that the range and skewness of implanted ion distributions increase in both axial and planar channeling irradiations.

Note that the (7°, 2°) spectrum overlaps with the (7°, 0°) spectrum rather than the (7°, 5°) spectrum. In fact, the width of planar channel is generally proportional to $(Z/E)^{1/2}$, where Z and E are the atomic number and the energy of incident ions, respectively.[22] The critical angle of the (100) planar channel in MgO for 2.0 MeV He ions is 0.245°.[22] Thus, it can be expected that the half angle for 1 MeV Au ions is ~2.4°, making the (7°, 2°) irradiation fall into the planar channel.

Fig. 5.5 (b) shows the depth profile measured by ToF-SIMS for 4 MeV Au ions irradiated in MgO (100) with the rotation of (7°, 2°). Although the ion range is much deeper than the SRIM prediction (will be discussed in detail in Sec. 5.6), no apparent channeling effect is observed. The difference in the ion distributions along the same direction between ion energies of 1 and 4 MeV can be explained by the fact that the

critical angle for 4 MeV Au ions is about a half of that for 1 MeV Au ions, i.e. ~1.2°. Consequently, the rotation of (7°, 2°) can avoid the (100) planar channels.

MgO samples are usually cut with edges parallel to the main crystalline axes. While the main axial channel may be avoided by solely rotating either θ or φ, the wide planar channels may not be completely avoided, as shown in both Figs. 5.4(b) and (c). As a result, although "a few degrees (usually 7°) off axial channel" is a regular method to minimize the channeling effect in previous studies,[23,24] rotating both θ and φ simultaneously is necessary to sufficiently avoid both axial and planar channels.

It is necessary to mention that, for 1 MeV Au, an observable "tail" exists even in the irradiations along (7°, 5°), (15°, 5°) and (15°, 7°), so-called "off channel" angles. This could be attributed to two contributions. First, when rotating large φ in order to fully avoid the (100) planar channel, the ions could fall into other higher index planar channels (which may not be obviously seen in Fig. 5.4) due to the large critical angles. Second, due to the open structure of MgO, some off-channel ions may fall into a channel after several collision or scattering events (post-collision channeling). Despite multiple attempts in this study on rotating the samples, channeling effects could not be fully eliminated for 1 MeV Au. As a result, if the purpose of a research effort requires strict "random" irradiation condition, either higher energy or lighter ions needs to be used.

5.5 Channeling effects on damage profile of MgO under Au ion irradiation

Channeling irradiations in MgO along axial and planar channels not only affect the ion distribution but also affect damage level and damage range. Fig. 5.6 (a) shows the RBS channeling spectra for 1 MeV Au ion irradiated MgO (110) to a fluence of 1×10^{14} cm^{-2} along different irradiation directions. The disorder levels derived from these spectra are shown in Fig. 5.6 (b). It is clearly observed that irradiations along both axial and planar channels significantly lead to lower peak damage level. Compared with the off-channel irradiation, peak damage level is decreased by ~30% for the irradiation along planar channel and by ~60% along the axial channel. In addition, the damage range for different

channeling irradiations is larger than that along the off channel irradiation. The corresponding implanted ion profiles, as measured by SIMS, are shown in Fig. 5.6 (c).

The decrease of peak damage level indicates a decrease of nuclear energy deposition or nuclear stopping power, which also accounts for the deeper penetration depth. Previous studies have shown that electronic stopping power is smaller in channeling irradiations for light ions (e.g. He[25]), but experimental validation is needed for the heavy ions in MgO.

It is also important to note that channeling irradiation effect on ion implantation profiles in MgO appears similar to the effects of thermal migration or irradiation-enhanced migration. Comparing with previous results, e.g. Fig. 1 in Ref. 24, two features are observed in both channeling effects and migration effects: (1) the damage level is decreased and (2) the damage is extended to deeper region. Thus, misinterpretation may happen if channeling irradiation (especially along planar channels) is not avoided, or its effect is not taken into account.

5.6 Electronic stopping power for Au ions in MgO

As stated in Sec. 5.4, a large discrepancy is observed between SRIM predicted and measured ion distributions for 4 MeV Au in MgO (Fig. 5.5 (b)), although the channeling effect is not observed. The projected ion range predicted by SRIM is 578 nm. The value determined by the SIMS measurement is ~773 nm ($\sum R_i n_i/N_i$, where n_i is the number of ions with the range of R_i, and N is the total number of ions), which is slightly smaller (<3%) than the peak position of 795 nm. Taking the potential irradiation-induced volume swelling (up to ~3%[26]) into consideration, the underestimation by SRIM is still ~23-25%, which is far beyond the experimental uncertainties. For the case of 1 MeV Au ions, only the peak position rather than the ion range from the measured results should be used for evaluation because of the residual channeling effect (i.e. the existence of the “tail”). Fig. 5.5 (a) shows that the peak position of 1 MeV Au ions in MgO (100) is ~167 nm as determined by RBS (corrected for the tilted angles during implantation). The SIMS determined value for 1 MeV Au ions in MgO (110) is 172 nm (Fig. 5.6 (c)). Considering

the possible volume swelling and the experimental uncertainties, the SIMS result is consistent with the RBS result. In contrast, SRIM predicted peak position for 1 MeV Au in MgO is ~158 nm (the ion range is 154 nm), which is ~7% less than the measured values.

Although no data from direct measurement of electronic stopping power for Au ions in MgO in this energy regime is available, some theoretical models can be used for comparison. Fig. 5.7 shows the electronic stopping power for Au ions in MgO predicted by SRIM[27], LS model[28] and the reciprocity theory[21]. Apparently, these three commonly used theories provide significantly inconsistent predictions. Note that the use of reciprocity theory relies on reliable stopping power data for light ions. SRIM usually provides reasonable predictions on electronic stopping powers for light ions. However, it has been found that SRIM predicted electronic stopping power for Mg ions in Au is significantly smaller than the experimental results[29] in the energy region below 70 keV/u. This may be the reason why the predicted values from reciprocity theory appear too low.

According to Eq. (3.3) and (3.4), the calculated ion ranges of 1 and 4 MeV Au in MgO are 173 and 668 nm based on the electronic stopping power values from the LS model. For 1 MeV Au, the calculated value agrees with the measured values, indicating the electronic stopping power in the LS model may be reasonable with energies lower than 1 MeV. For 4 MeV Au, the calculated value is still smaller than the measured values but much closer to the experiments than the SRIM predictions, indicating that the electronic stopping power given by the LS model may be slightly larger than the actual value but is more reasonable than SRIM predictions. This result qualitatively agrees with the study for Au ions in SiC,[1] demonstrated in chapter 3.

5.7 References

1 K. Jin, Y. Zhang, Z. Zhu, D. A. Grove, H. Xue, J. Xue, and W. J. Weber, J. Appl. Phys. **115**, 044903 (2014).

2 P. Sigmund, Nucl. Instrum. Methods Phys. Res. B **135**, 1 (1998).

3 D. J. O'Connor and J. P. Biersack, Nucl. Instrum. Methods Phys. Res. B **15**, 14 (1986).

4 H. Geissel, W. N. Lennard, H. R. Andrews, D. P. Jackson, I. V. Mitchell, D. Philips, and D. Ward, Nucl. Instrum. Methods Phys. Res. B **12**, 38 (1985).

5 K. Jin, Y. Zhang, H. Xue, Z. Zhu, and W. J. Weber, Nucl. Instrum. Methods Phys. Res. B **307**, 65 (2013).

6 F. Schrempel, T. Steinbach, Th Gischkat, and W. Wesch, Nucl. Instrum. Methods Phys. Res. B **266**, 2958 (2008).

7 Z. Zolnai, A. Ster, N. Q. Khanh, G. Battistig, T. Lohner, J. Gyulai, E. Kotai, and M. Posselt, J. Appl. Phys. **101**, 023502 (2007).

8 Dearnale.G, J. H. Freeman, G. A. Gard, and M. A. Wilkins, Can. J. Phys. **46**, 587 (1968).

9 M. Posselt, M. Mader, R. Grotzschel, and M. Behar, Appl. Phys. Lett. **83**, 545 (2003).

10 S. Roorda, W. C. Sinke, J. M. Poate, D. C. Jacobson, S. Dierker, B. S. Dennis, D. J. Eaglesham, F. Spaepen, and P. Fuoss, Phys. Rev. B **44**, 3702 (1991).

11 W. Jiang and W. J. Weber, Phys. Rev. B **64**, 125206 (2001).

12 E. Friedland, Nucl. Instrum. Methods Phys. Res. B **80-81**, 128 (1993).

13 E. Wendler, K. Gärtner, and W. Wesch, Nucl. Instrum. Methods Phys. Res. B **257**, 488 (2007).

14 H. Ogiso, S. Nakano, and J. Akedo, Nucl. Instrum. Methods Phys. Res. B **206**, 157 (2003).

15 K. Takahiro, A. Kunimatsu, S. Nagata, S. Yamaguchi, S. Yamamoto, Y. Aoki, and H. Naramoto, Nucl. Instrum. Methods Phys. Res. B **152**, 314 (1999).

16 Z. Mao, Z. He, D. Chen, W. Y. Cheung, and S. P. Wong, Solid State Communications **142**, 329 (2007).

17 R. L. Zimmerman, C. I. Muntele, and D. Ila, Surf. Coat. Technol. **196**, 85 (2005).

18 I. O. Usov, P. N. Arendt, and K. E. Sickafus, Nucl. Instrum. Methods Phys. Res. B **268**, 622 (2010).

19 E. Friedland, Nucl. Instrum. Methods Phys. Res. B **80/81**, 128 (1993).

20 P. Giri, V. Raineri, G. Franzo, and E. Rimini, Phys. Rev. B **65**, 012110 (2001).

21 P. Sigmund, Euro. Phys. J. D **47**, 45 (2008).

22 S. D. Mukherjee and D. W. Palmer, Phys. Lett. **69A** (1979).

23 E. Friedland and M. Hayes, Nucl. Instrum. Methods Phys. Res. B **65**, 287 (1992).

24 I. O. Usov, P. N. Arendt, J. R. Groves, L. Stan, and R. F. DePaula, Nucl. Instrum. Methods Phys. Res. B **243**, 87 (2006).

25 L. Shao and M. Nastasi, Appl. Phys. Lett. **87**, 064103 (2005).

26 G. F. Hurley, J. C. Kennedy, Jr. F. W. Clinard, R. A. Youngman, and W. R. McDonell, J. Nucl. Mater. **103-104**, 761 (1981).

27 J. F. Ziegler, (www.srim.org).
28 J. Lindhard, M. Scharff, and H.E. Schioett, Mat. Fys. Medd. K. Dan. Vidensk. Selsk. **33**, 1 (1963).
29 K. Arstila, J. Keinonen, and P. Tikkanen, Phys. Rev. B **41**, 6117 (1990).

Appendix 5.1

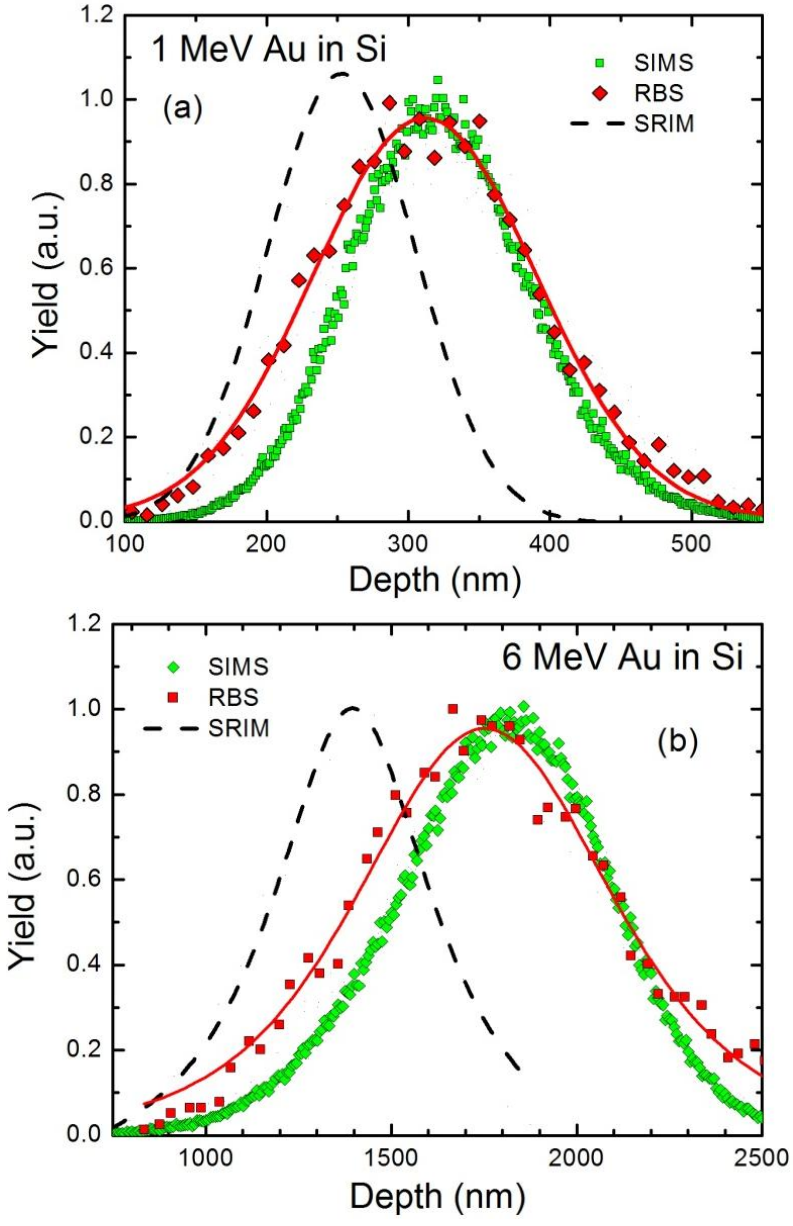

Fig. 5.1. SIMS and RBS measured depth profiles of implanted Au ions with (a) 1 MeV and (b) 6 MeV. SRIM predicted results are also shown for comparison.

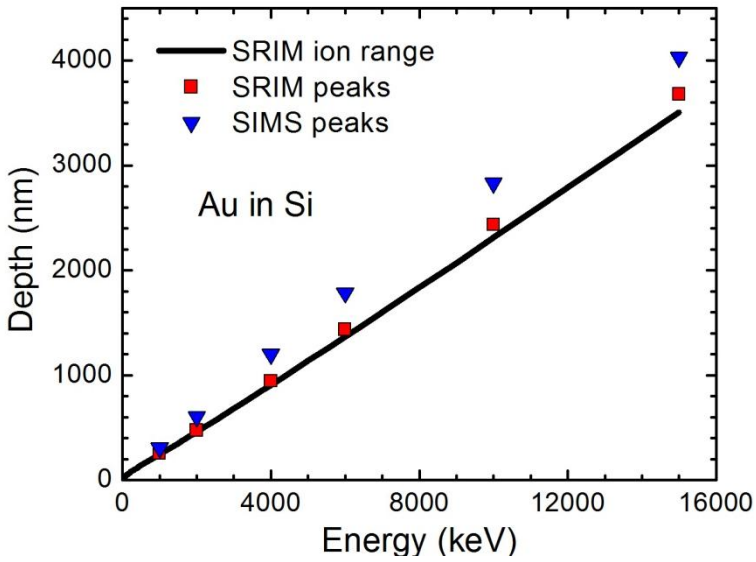

Fig. 5.2. Peak positions of the depth profiles of Au ions with different energies in Si, measured by SIMS (blue triangles) and predicted by SRIM (red squares). The ion ranges predicted by SRIM are shown as the solid line. The SIMS results are corrected for 3% volume swelling.

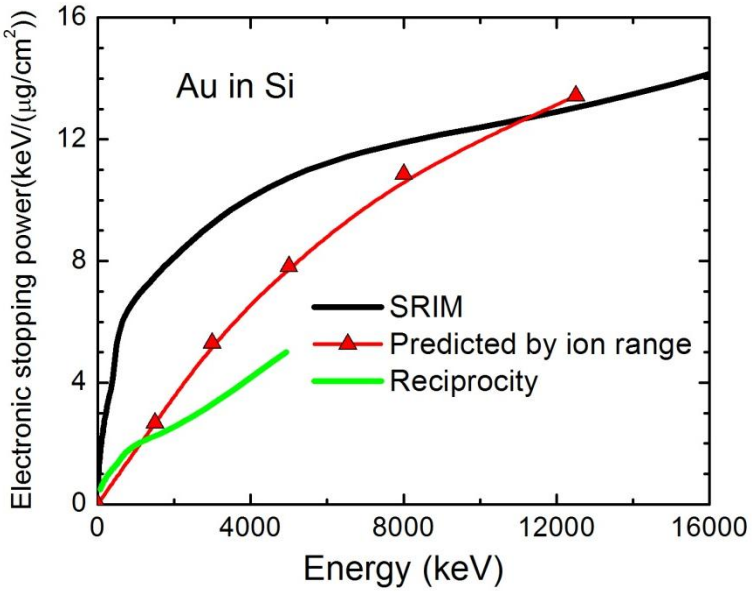

Fig. 5.3. Electronic stopping powers calculated based on the data in Fig. 5.2 (Red triangles). The predictions from SRIM (black line) and the reciprocity theory (green line) are also shown for comparison.

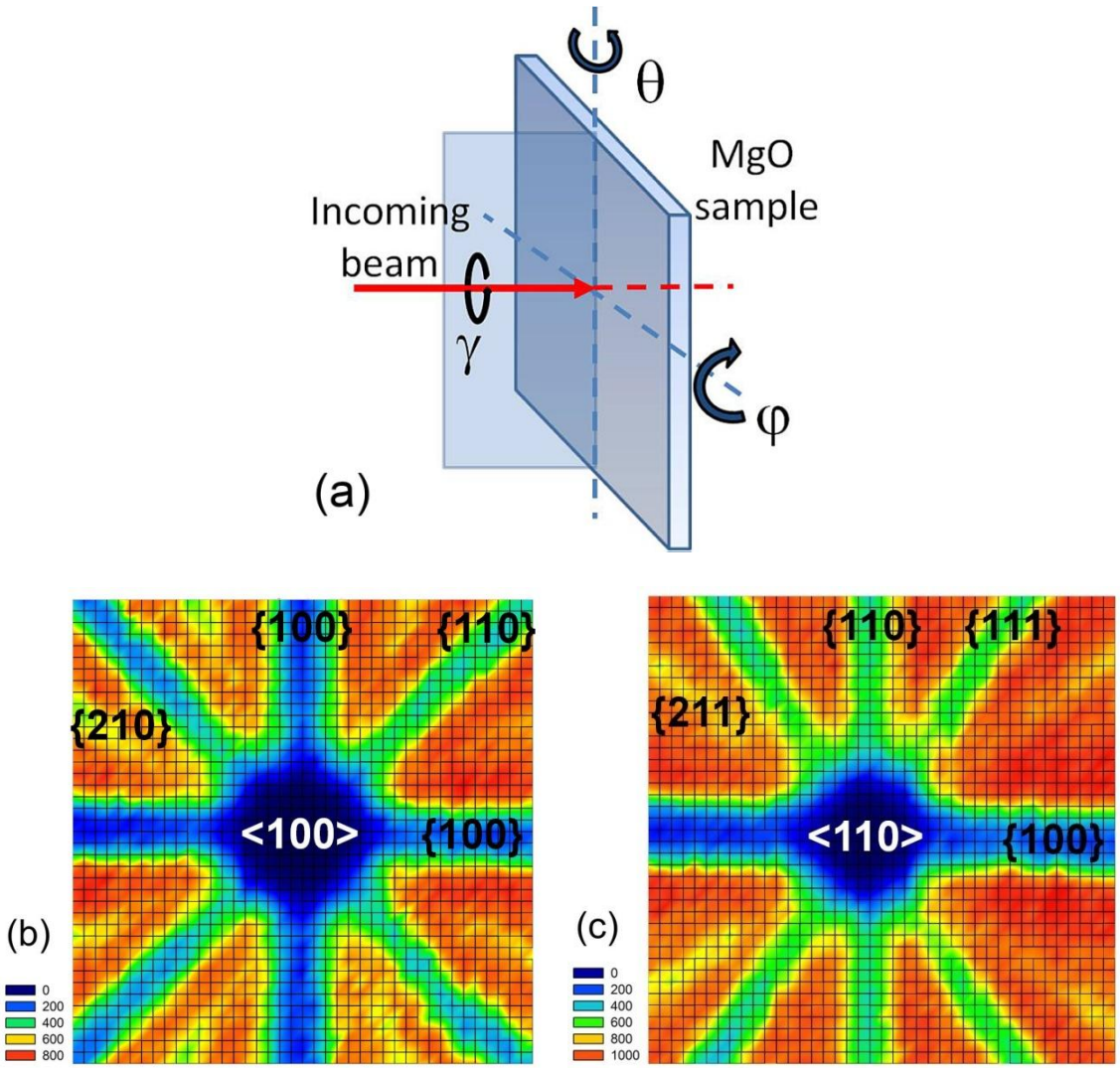

Fig. 5.4. (a) Geometric configuration of the rotations of a MgO sample. (b), (c) Contour maps of a 2-D angular scan (θ as horizontal and φ as vertical axes) of MgO (100) and (110), respectively. The scanning range is ±1.44° and the step length is 0.072°.

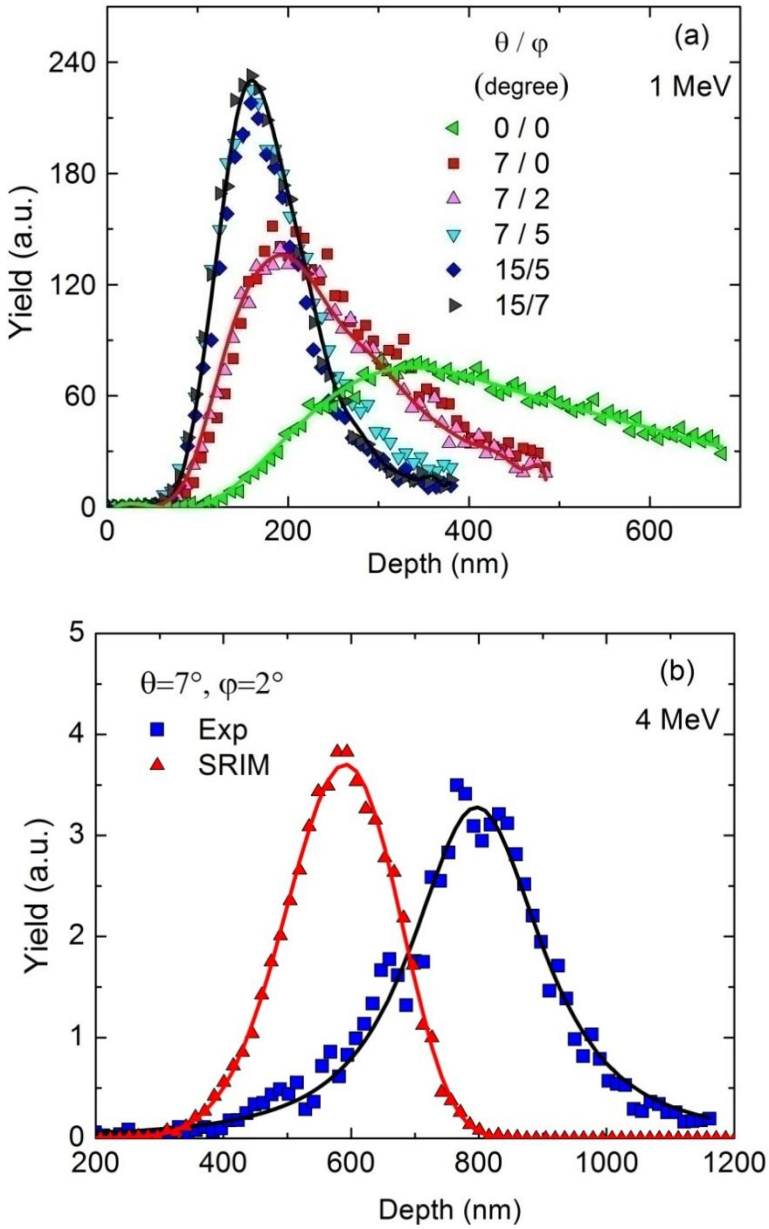

Fig. 5.5. (a) Depth profiles of 1 MeV Au irradiated in MgO (100) along various directions, as measured by RBS. (b) Depth profile of 4 MeV Au irradiated MgO (100) along (θ, φ) = (7°, 2°), measured using ToF-SIMS. The SRIM prediction is presented for comparison. Solid lines are fit to data.

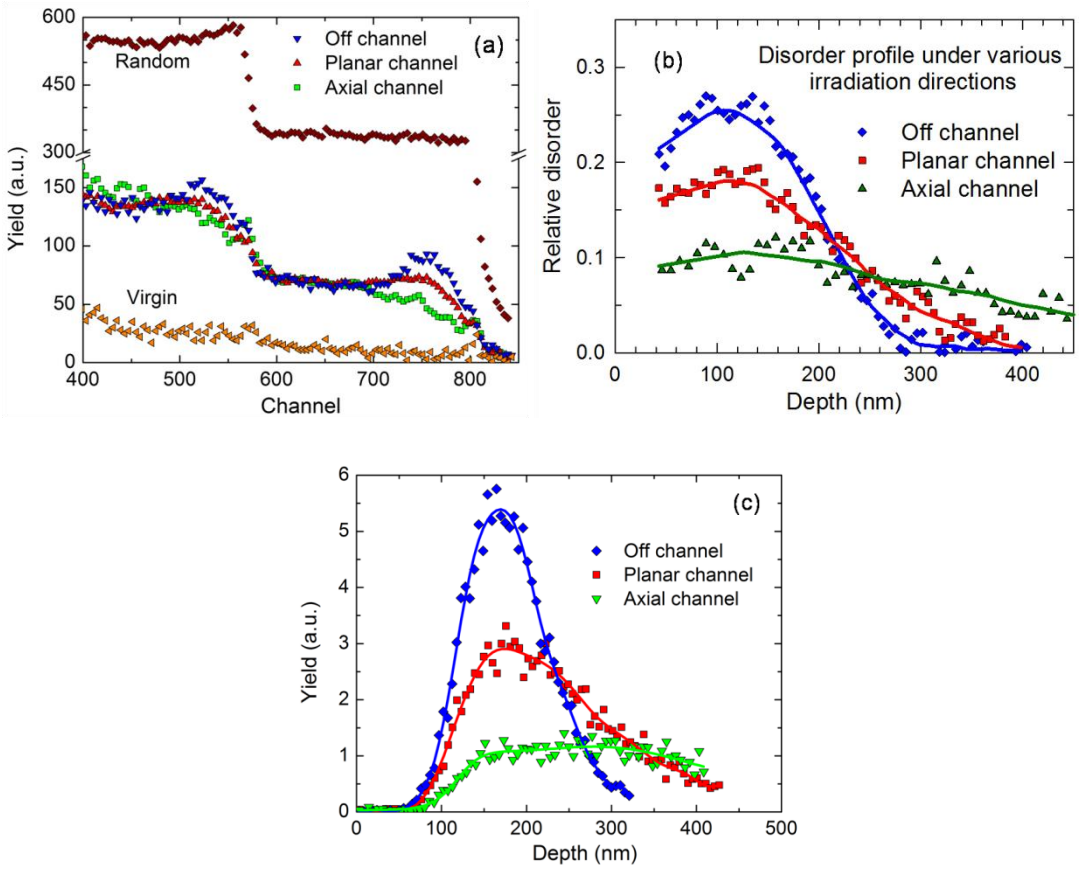

Fig. 5.6. (a) RBS channeling spectra, (b) derived disorder profile from (a), and (c) SIMS measured depth profiles of 1 MeV Au ions irradiated in MgO (110) along the directions of axial channel, planar channel, and off channel. The irradiation fluence is 1×10^{14} cm^{-2}. Solid lines are fit to data.

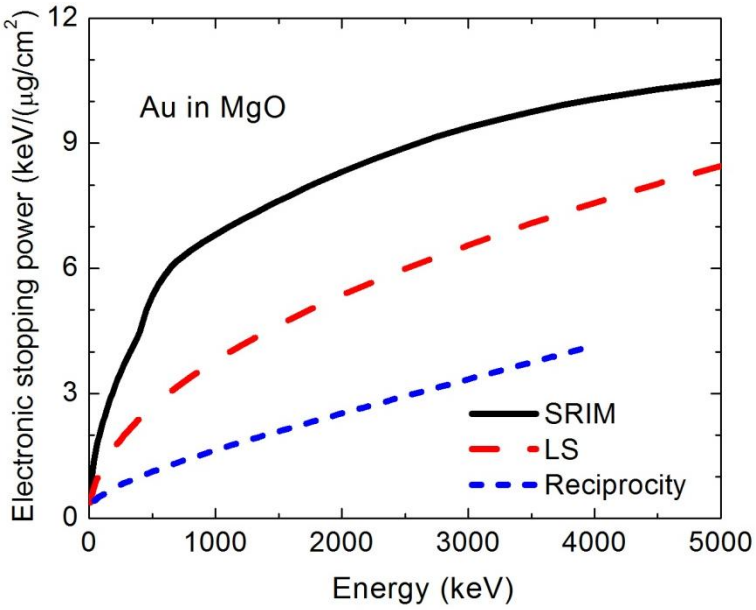

Fig. 5.7. Electronic stopping powers for Au ions in MgO predicted by SRIM, LS model and reciprocity theory.

CHAPTER 6

EFFECTS OF NUCLEAR AND ELECTRONIC ENERGY DEPOSITION ON DEFECT EVOLUTION IN MGO

Abstract

In this chapter, RBS channeling technique is applied to study defect evolution in MgO under 1 MeV Au ion irradiation. For fluences lower than 2.5×10^{14} cm^{-2}, damage accumulation is observed. With further irradiations, the damage level is observed decreased at the original damage peak, and the depth corresponding to the maximum measured damage increases. According to cross-sectional TEM analysis, the observations from RBS channeling may be attributed to clustering of point defects. Furthermore, 21 MeV Ni ions are irradiated in the MgO samples, in which initial damage is induced by 1 MeV Au ions. The observations from both RBS channeling and TEM show that the pre-induced damage level is decreased under the Ni ion irradiation, probably due to the formation of dislocation loops promoted by ionizing energy deposition.

6.1 Introduction

Irradiation effects in MgO have been extensively studied for decades (e.g. Ref.1-13) for its promising applications in nuclear engineering. For example, MgO is proposed as a candidate material used in inert matrix fuel due to its high melting temperature, high thermal conductivity, and high irradiation tolerance.[14,15] MgO is also a typical model ionic ceramic for studies of ion-solid interaction, due to its simple chemical and crystalline structure.

However, as discussed in chapter 1, understanding defect evolution in MgO is a long-standing challenge. Heavy ion irradiation induces complex damage process involving point defects, dislocations, and randomly disordered region.[10,16] Significantly deeper than expected damage range has been reported under high fluence irradiations with different ions at different energies.[1,5,13,17] Agreement has not been achieved on interpreting these results.

In contrast to extensive studies on the damage evolution induced by nuclear energy deposition, effects of electronic energy deposition on defect evolution in MgO have not been well understood. Competitive effects between nuclear and electronic energy

deposition have recently been observed under dual beam irradiations,[18,19] but the underlying mechanism is not clear.

In this chapter, defect evolution under nuclear and electronic energy deposition is studied using RBS channeling technique. Cross-sectional TEM is utilized as a complementary technique to interpret the ion channeling results.

6.2 Experimental

Defect evolution under heavy ion irradiation is studied under two circumstances: nuclear energy loss dominant and electronic energy loss dominant. 1.0 MeV Au ion is selected for the first case, and 21 MeV Ni ion is used for the second one. According to SRIM, the nuclear and electronic stopping powers of 1 MeV Au ion in MgO are 4.7 and 2.4 keV/nm, respectively. However, according to the result in chapter 5, this electronic stopping power value is not reliable. Instead, the LS value, 1.3 keV/nm, is more realistic. For 21 MeV Ni ion, the SRIM predicted values of nuclear and electronic stopping power are 0.08 and 9.4 keV/nm. In this case, most (>99%) of the energy deposition is to electronic subsystem.

In order to study defect accumulation and evolution under nuclear energy deposition, irradiation with 1 MeV Au ions are performed to the fluences ranging from 2×10^{13} to 5×10^{15} cm^{-2}. In order to study the ionization effects resulting from electronic energy deposition on existing defects in MgO, irradiations of MgO with 1 MeV Au ions are carried out at the fluence of 1×10^{14} cm^{-2} to induce an initial damage state. The initial damage is induced at both room temperature (~300 K) and low temperature (~193 K). The damaged samples are further irradiated with 21 MeV Ni ions at room temperature to fluences up to 6.5×10^{15} cm^{-2}.

The technical details of irradiation conditions are described in Sec. 2.6. Ion channeling studies are described in Sec. 2.5. TEM observations are carried out at 200 keV with a Zeiss Libra 200MC TEM/STEM.

6.3 Defect evolution in MgO under nuclear energy deposition

Fig. 6.1 shows the RBS/channeling spectra of MgO irradiated with 1 MeV Au ions at different fluences at room temperature. There appear two stages in the damage evolution within this fluence range. The first stage ranges from 2×10^{13} to ~2.5×10^{14} cm^{-2}, corresponding to a peak dose from 0.08 to 1 dpa. In this stage, damage accumulation is observed. Since the damage peak exists in the channeling spectra, the defect type can be expected to include point defects or local amorphous regions, which agrees with previous experimental results.[1] With further irradiations beyond 2.5×10^{14} cm^{-2}, two phenomenon are observed. First, damage level is decreased at the original damage peak and near the sample surface. Second, the measured damage peak appears to shift to deeper region. For example, at fluence of 2.5×10^{15} cm^{-2}, the damage peak is shifted to ~340 nm, which is much deeper than that for low fluences (~140 nm).

Ion channeling technique is good at quantifying point defects and providing depth information. However, it provides limited information on the detailed structural information of higher dimensional defects, especially when different types of defects are mixed together. As a result, cross-sectional TEM is employed to further investigate the nature of defect structures. Fig. 6.2 shows the high resolution (HR) TEM images and the corresponding diffraction patterns from Fast-Fourier-Transform (FFT) of the MgO irradiated with 1 MeV Au ions to a fluence of 2.5×10^{15} cm^{-2}. The images are taken at the depth of ~120-160 nm, corresponding to the displacement peak region (~10 dpa), where decrease in damage level is observed by RBS channeling technique. Typical Moiré patterns are clearly observed in Figs. 6.2 (a) and (c). More Moiré patterns are observed in different locations at the same depth in several parallel samples, while they are not observed in pristine samples or in the samples irradiated at low fluences. Moiré patterns show the interfering of the two sets of lattice that have nearly common periodicities.[20] In other words, it results from slight lattice mismatch, translation, or rotation in lattice orientations.[21] Figs. 6.2 (b) and (d) indicate two situations corresponding to the cases of lattice translation or lattice rotation.

In molecular-dynamic simulations,[22] interstitial clusters with rock-salt structure are observed to aggregate from randomly distributed Frankel pairs in MgO. These "structural" defect clusters can be expected in experiments to have a slight mismatch in orientations, or displacement compared to their parent lattice. Such mismatch may result in the observation of Moiré patterns from TEM. Besides, this can also explain the decrease in damage level observed in the RBS channeling study, because the organized defects contribute less to the direct backscattering yield of incident He ions compared to the randomly distributed interstitials.[23]

As discussed in chapter 1, significantly deeper-than-expected damage range (or damage peak) in MgO has been reported in studies using different heavy ions since 1990s.[5,13,17] One of the proposed explanations is diffusion or migration of defects,[17,24,25] which can explain why defects appear at the depth beyond the irradiation range. Although defect migration may contribute to such observations, there is another factor that cannot be ignored. As discussed in chapter 5, channeling irradiation effects cannot be fully avoided despite the attempts of rotating the samples. In the case of 1 MeV Au ion irradiation in MgO, based on the SIMS measurement, as shown in Fig. 6.3, considerable number of implanted Au ions (>10% comparing to the peak concentration) stop at depths over 300 nm. On the other hand, Fig. 6.4 shows the disorder level (based on the ion channeling result shown in Fig. 6.1) as a function of ion fluence. The damage level decreases after a critical dose due to the clustering of interstitials. As a result, it is reasonable to expect that under high irradiation fluences, the damage level at the dose peak drops, while the deep region may reach the doses corresponding to the maximum damage level. Consequently, the damage peak appears to move into the deep region.

It is necessary to emphasize that this contribution may be easily overlooked if the measured depth profile is only compared with the SRIM predictions because SRIM assumes amorphous materials, and such channeling irradiation induced "tail" will not be observed. As a result, using SRIM to predict or describe damage and ion profile requires more caution in the materials in which channeling effect is significant. In such cases, it may be necessary to measure ion distributions to interpret the observed damage profile.

6.4 Defect evolution in MgO under electronic energy deposition

Fig. 6.5 shows the ion channeling spectra of the MgO irradiated initially with 1 MeV Au ions at low temperature (~193 K) and with subsequent 21 MeV Ni ions at room temperature. With only Au ion irradiation, a damage peak is observed with a relative disorder of ~0.25. No significant change is observed after subsequent Ni ion irradiation until a fluence of 1×10^{14} cm^{-2}. With further Ni ion irradiation, the damage level around the original damage peak decreases. In addition to the decease of damage level, the shape of the channeling spectra is changed. The "damage peak" disappears after high fluence (larger than 1×10^{15} cm^{-2}) Ni ion irradiations. The measurement of Ni ion irradiated MgO after the initial Au irradiation at room temperature shows a similar result in the damage evolution as this case.

It has been introduced in chapter 2 that RBS channeling yield of a material containing defects includes two parts: dechanneling part and direct backscattering part. Generally speaking,[23] contributions of point defects from both direct backscattering and dechanneling are significant. As a result, a "peak" in RBS channeling profile is usually observed. Typical examples of this feature include Si,[26] SiC,[27] $SrTiO_3$,[28] etc. In contrast, for some other defects, e.g. dislocations, the contribution from direct backscattering is negligible comparing with that from dechanneling. In such cases, such "peak" is not seen or not significant. This is usually observed in ion irradiated metals.[29] It has also been observed in some ceramics in which dislocations are the dominant type of defects, e.g. ZrO_2.[30]

Electronic energy deposition has conflicting effects on defect evolution, as discussed in detail in chapter 1. It has been studied in SiC where a significant annealing effect is observed: the pre-induced damage level is decreased after the electronic energy deposition from high energy ion beam irradiations (See Fig. 1.7).[31] The behavior in SiC appears similar in MgO, except that an overall decrease of damage profile in SiC is observed. In other words, the shape of "damage peak" remains during the ion annealing process in SiC while the disorder level decreases as a result of defect annealing and recrystallization of amorphization domains. This difference suggests that the mechanism

of ion annealing process between SiC and MgO is different. Change of defect types can be reasonably expected in MgO under 21 MeV Ni ion irradiation.

TEM is utilized to study defect structure of Ni ion annealed MgO. Fig. 6.6 shows a cross-sectional TEM image of MgO irradiated with 1 MeV Au ions to 1×10^{14} cm^{-2} at 193 K, followed by the 21 MeV Ni ion irradiation to the fluence of 6.5×10^{15} cm^{-2} at room temperature. The image is taken at the depth close to the damage peak of the Au ion irradiation. Different from the high dose 1 MeV Au ion irradiation, Moiré patterns are not observed. Instead, dislocation loops with the size of a few nm are observed.

This TEM observation supports the findings from RBS channeling that dislocation loops contribute little to direct backscattering yield but introduce a large dechanneling yield.[23] Dislocations have been observed in MgO by TEM in neutron irradiation at elevated temperature (430 K).[32] It can be reasonably expected that the local elevated temperature induced by electronic energy deposition through electron-phonon coupling enhances mobility of point defects and thus promotes formation of such dislocation loops. The findings in this work also agree well with the competitive effects observed between the nuclear and electronic energy deposition from the dual beam irradiation experiments.[18,19]

6.5 References

1 E. Friedland, Nucl. Instrum. Methods Phys. Res. B **80**-**81**, 128 (1993).

2 H. Matzke, A. Turos, P. Rabette, and O. Meyer, J. Phys. C: Solid State Phys. **14**, 3333 (1981).

3 E. R. Vance, Surf. Interface Anal. **12**, 509 (1988).

4 K. Takahiro, A. Kunimatsu, S. Nagata, S. Yamaguchi, S. Yamamoto, Y. Aoki, and H. Naramoto, Nucl. Instrum. Methods Phys. Res. B **152**, 314 (1999).

5 H. Ogiso, S. Nakano, and J. Akedo, Nucl. Instrum. Methods Phys. Res. B **206**, 157 (2003).

6 R. L. Zimmerman, C. I. Muntele, and D. Ila, Surf. Coat. Technol. **196**, 85 (2005).

7 I. O. Usov, P. N. Arendt, J. R. Groves, L. Stan, and R. F. DePaula, Nucl. Instrum. Methods Phys. Res. B **243**, 87 (2006).

8 Z. Mao, Z. He, D. Chen, W. Y. Cheung, and S. P. Wong, Solid State Communications **142**, 329 (2007).

9 E. Wendler, K. Gärtner, and W. Wesch, Nucl. Instrum. Methods Phys. Res. B **266**, 2872 (2008).

10 I. O. Usov, P. N. Arendt, and K. E. Sickafus, Nucl. Instrum. Methods Phys. Res. B **268**, 622 (2010).

11 L. Thomé, A. Debelle, F. Garrido, P. Trocellier, Y. Serruys, G. Velisa, and S. Miro, Appl. Phys. Lett. **102**, 141906 (2013).

12 G. B. Krefft, J. Vac. Sci. Technol. **14**, 533 (1977).

13 E. Friedland and M. Hayes, Nucl. Instrum. Methods Phys. Res. B **65**, 287 (1992).

14 E. A. C. Neeft, K. Bakker, R. L. Belvroy, W. Tams, R. P. C. Schram, R. Conrad, and A. van Veen, J. Nucl. Mater. **317**, 217 (2003).

15 S. Miwa, Y. Ishi, and M. Osaka, J. Nucl. Mater. **389**, 402 (2009).

16 E. Friedland, Nucl. Instrum. Methods Phys. Res. B **80**/**81**, 128 (1993).

17 E. Wendler, K. Gärtner, and W. Wesch, Nucl. Instrum. Methods Phys. Res. B **257**, 488 (2007).

18 L. Thomé, A. Debelle, F. Garrido, P. Trocellier, Y. Serruys, G. Velisa, and S. Miro, Appl. Phys. Lett. **102**, 141906 (2013).

19 L. Thome, G. Velisa, A. Debelle, S. Miro, F. Garrido, P. Trocellier, and Y. Serruys, Nucl. Instrum. Methods Phys. Res. B **326**, 219 (2014).

20 D. B. Williams and C. B. Carter, *The Transmission Electron Microscope*. (Springer US, 1996), pp.392.

21 A. J. Martinez-Galera, I. Brihuega, A. Gutierrez-Rubio, T. Stauber, and J. M. Gomez-Rodriguez, Sci. Rep. **4**, 7314 (2014).

22 D. S. Aidhy, P. C. Millett, D. Wolf, S. R. Phillpot, and H. Huang, Scripta Mater. **60**, 691 (2009).

23 L. C. Feldman, J. W. Mayer, and S. T. Picraux, *Materials Analysis by Ion Channeling*. (Academic Press, 1982).

24 S. Moll, Y. Zhang, A. Debelle, L. Thomé, J. Crocombette, Z. Zihua, J. Jagielski, and W. J. Weber, Acta Mater. **88**, 314 (2015).

25 L. Gea, C. R. A. Catlow, S. M. M. Ramos, B. Canut, and P. Thevenard, Nucl. Instrum. Methods Phys. Res. B **65**, 282 (1992).
26 S. Roorda, W. C. Sinke, J. M. Poate, D. C. Jacobson, S. Dierker, B. S. Dennis, D. J. Eaglesham, F. Spaepen, and P. Fuoss, Phys. Rev. B **44**, 3702 (1991).
27 W. Jiang and W. J. Weber, Phys. Rev. B **64**, 125206 (2001).
28 Y. Zhang, J. Lian, C. M. Wang, W. Jiang, R. Ewing, and W. J. Weber, Phys. Rev. B **72**, 094112 (2005).
29 J. A. Borders and J. M. Poate, Phys. Rev. B **13**, 969 (1976).
30 S. Moll, L. Thome, G. Sattonnay, A. Debelle, F. Garrido, L. Vincent, and J. Jagielski, J. Appl. Phys. **106**, 073509 (2009).
31 Y. Zhang, T. Varga, M. Ishimaru, P. D. Edmondson, H. Xue, P. Liu, S. Moll, F. Namavar, C. Hardiman, S. Shannon, and W. J. Weber, Nucl. Instrum. Methods Phys. Res. B **327**, 33 (2014).
32 F. W. Clinard, G. F. Hurley, and L. W. Hobbs, J. Nucl. Mater. **108**, 655 (1982).

Appendix 6.1

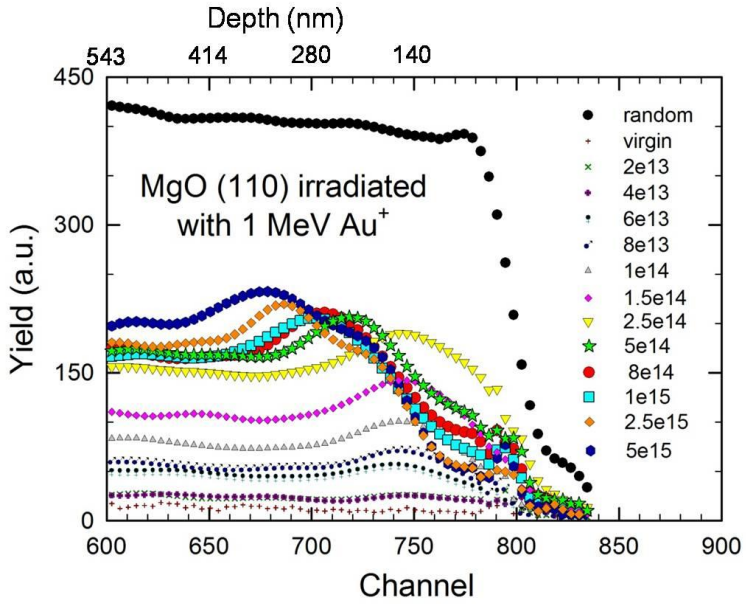

Fig. 6.1. RBS channeling spectra of MgO (110) single crystal irradiated with 1 MeV Au ions at room temperature. The Au fluence ranges from 2×10^{13} to 5×10^{15} cm^{-2}.

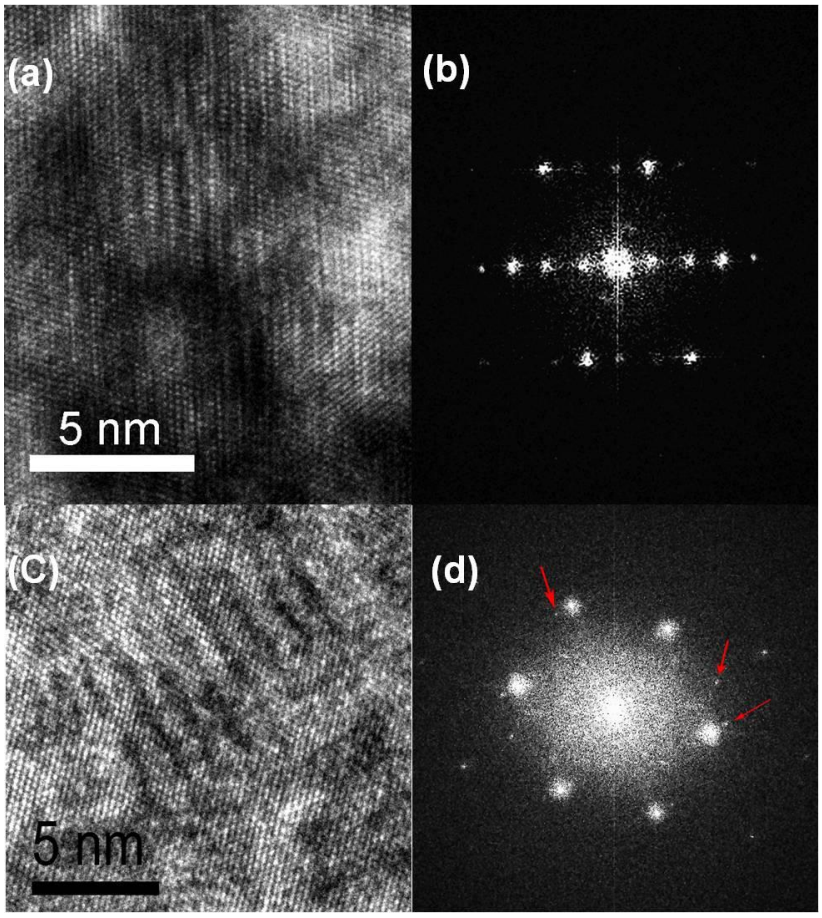

Fig. 6.2. HRTEM images and the corresponding diffraction patterns from FFT of the MgO (110) irradiated with 1 MeV Au ions at the fluence of 2.5×10^{15} cm^{-2}. The images are taken at the depth of ~120-160 nm, corresponding to the displacement peak region (10 dpa), where the decrease in damage level is observed by RBS/channeling technique.

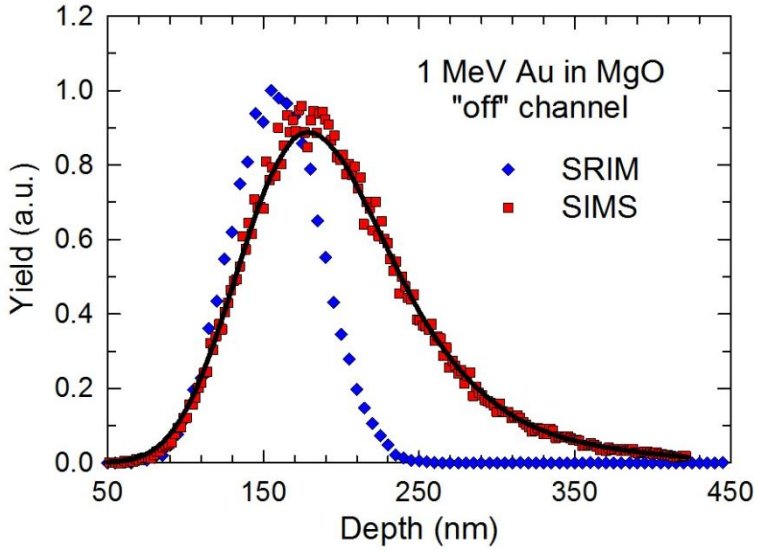

Fig. 6.3. SRIM predicted and SIMS measured 1 MeV Au ion distributions in MgO.

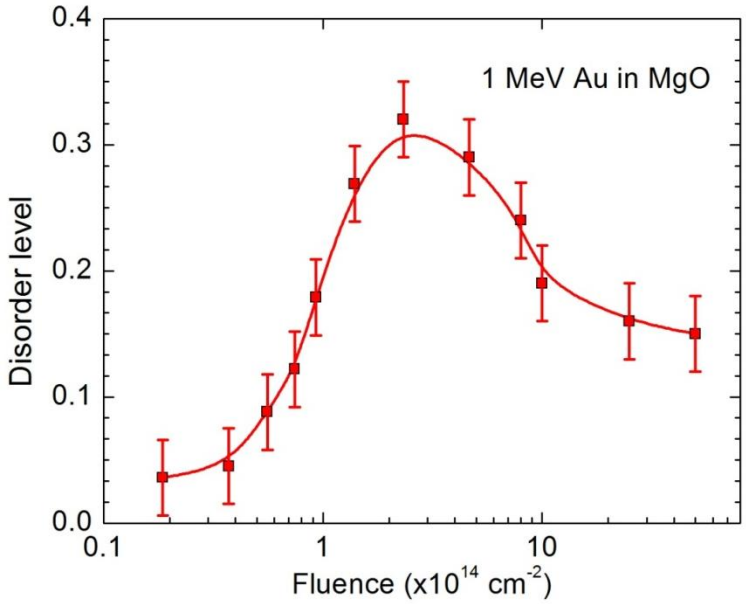

Fig. 6.4. Disorder level as a function of ion fluence for MgO irradiated with 1 MeV Au ions. The disorder levels are taken at the displacement peak.

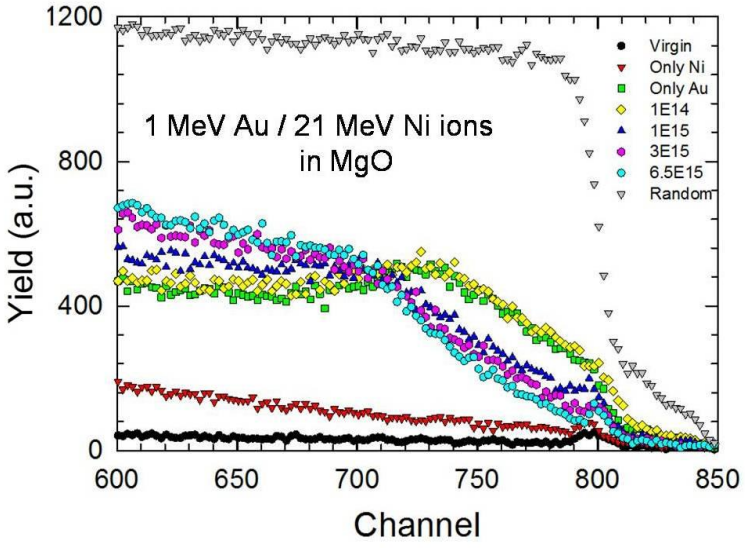

Fig. 6.5. RBS channeling spectra of MgO (110) single crystal irradiated with 1 MeV Au ions at low temperature only (green squares), 21 MeV Ni ions at room temperature only (red opposite triangles), and the 21 MeV Ni ions at different fluences after the pre-damage induced by the Au irradiation.

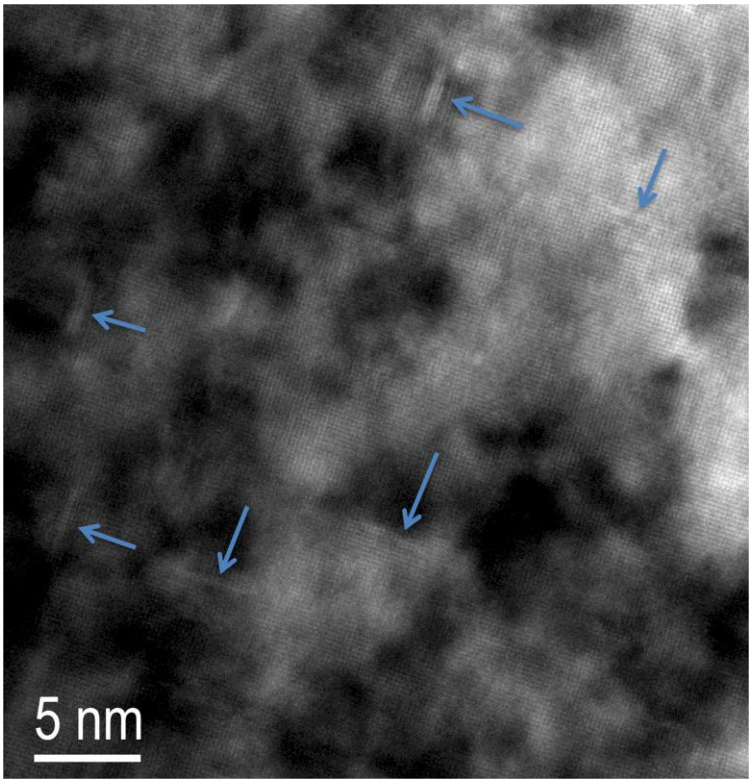

Fig. 6.6.Cross-sectional TEM image of MgO irradiated with 1 MeV Au ions to fluence of 1×10^{14} cm^{-2} at low temperature, followed by 21 MeV Ni ion irradiation to fluence of 6.5×10^{15} cm^{-2}.

CHAPTER 7
CONCLUSION

In this dissertation, electronic stopping powers for heavy ions (i.e. Cl, Br, I and Au) in SiC and SiO_2 are determined over a continuous energy regime. Considerable error is observed in SRIM predictions, especially for Au ions. By combining the reciprocity theory with experimental results, new electronic stopping power curves are derived, and a modified TRIM code has been developed to utilize our derived electronic stopping power values. RBS and ToF-SIMS have been applied to measure the Au ion distribution in SiC. The measured ion range-energy relationship and the ion distributions agree well with the predictions from our modified TRIM code, validating our derived electronic stopping power values. [K. Jin, Y. Zhang, Z. Zhu, D. A. Grove, H. Xue, J. Xue, and W. J. Weber, "Electronic stopping powers for heavy ions in SiC and SiO_2" J. Appl. Phys. 115 (2014) 044903]

In order to experimentally examine nuclear stopping predicted in SRIM that is important to the stopping measurement, an approach that can be performed using regular instruments commonly existed in ion beam laboratories has been demonstrated to measure angular distributions of MeV ions penetrating thin foils. The angular distribution of 1 MeV Au ions after penetrating a Si_3N_4 thin foil has been measured. The experimental results agree with the SRIM predictions within a 10% uncertainty. Thinning effects in the suspended thin foils due to forward recoils induced by heavy ion irradiation has been observed and accounted for. [K. Jin, Z. Zhu, S. Manandhar, J. Liu, C. Chen, V. Shutthanandan, S. Thevuthasan, W. J. Weber and Y. Zhang, "Angular distribution and recoil effect for 1 MeV Au^+ ions through a Si_3N_4 thin foil" Nucl. Instr. Meth. Phys. Res., Sect. B 332 (2014) 346]

In addition to direct measurements of electronic stopping power for Au ions in SiC and SiO_2, Au stopping in Si has also been derived from measurement of ion distributions at different energies ranging from 1 to 15 MeV. The derived electronic stopping powers in the low energy regime are significantly lower than the predictions from SRIM, which agrees with the results of Au ions in SiC and SiO_2 that SRIM overestimates the electronic stopping power for heavy ions in light targets. [Chapter 5]

Significant channeling effects have been observed for Au ion irradiation in MgO. Irradiations along both axial and planar channels lead to deeper ion and damage distribution, as well as a lower peak damage level. The channeling effect cannot be fully avoided for 1 MeV Au ion irradiation, despite the attempts of sample rotation. [Chapter 5] Along with the clustering of point defects, this could contribute to the observations of the unusual deeper damage in MgO after high fluence ion irradiations. [Chapter 6]

The defect evolution in pre-damaged MgO under 21 MeV Ni ion irradiations has been studied using RBS/channeling technique combined with TEM observation. It has been observed that the damage level in MgO is decreased after the Ni ion irradiations, which is probably due to the formation of dislocation loops promoted by the electronic energy deposition. [Chapter 6]

APPENDIX

PUBLICATIONS

Some of the results in this dissertation have been published. Here, the publication information and the contributions from Ke Jin are listed. The results in chapter 3 have been published in *Publication 2*; the results in chapter 4 have been published in *Publication 3*.

1. **K. Jin**, H.Y. Xiao, Y. Zhang, and W.J. Weber, "Effects of boron-nitride substrates on Stone-Wales defect formation in graphene: an ab initio molecular dynamics study" Appl. Phys. Lett. 104 (2014) 203106

   K. Jin's involvement: proposed and performed the simulation, analyzed the results and wrote the paper.

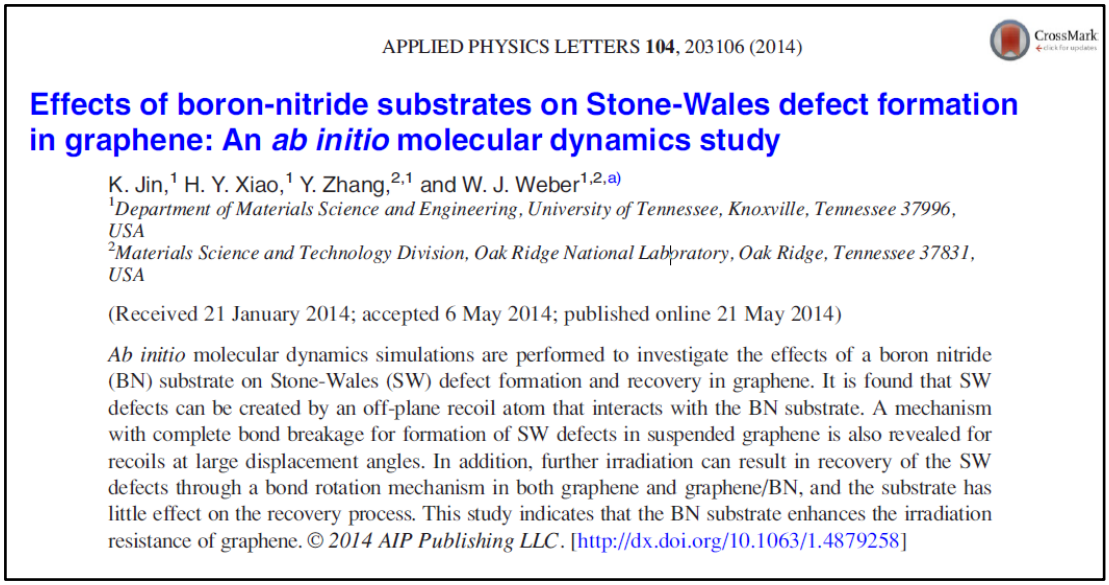

APPLIED PHYSICS LETTERS **104**, 203106 (2014)

Effects of boron-nitride substrates on Stone-Wales defect formation in graphene: An *ab initio* molecular dynamics study

K. Jin,[1] H. Y. Xiao,[1] Y. Zhang,[2,1] and W. J. Weber[1,2,a)]
[1]*Department of Materials Science and Engineering, University of Tennessee, Knoxville, Tennessee 37996, USA*
[2]*Materials Science and Technology Division, Oak Ridge National Laboratory, Oak Ridge, Tennessee 37831, USA*

(Received 21 January 2014; accepted 6 May 2014; published online 21 May 2014)

Ab initio molecular dynamics simulations are performed to investigate the effects of a boron nitride (BN) substrate on Stone-Wales (SW) defect formation and recovery in graphene. It is found that SW defects can be created by an off-plane recoil atom that interacts with the BN substrate. A mechanism with complete bond breakage for formation of SW defects in suspended graphene is also revealed for recoils at large displacement angles. In addition, further irradiation can result in recovery of the SW defects through a bond rotation mechanism in both graphene and graphene/BN, and the substrate has little effect on the recovery process. This study indicates that the BN substrate enhances the irradiation resistance of graphene. © *2014 AIP Publishing LLC*. [http://dx.doi.org/10.1063/1.4879258]

2. **K. Jin**, Y. Zhang, Z. Zhu, D. A. Grove, H. Xue, J. Xue, and W. J. Weber, "Electronic stopping powers for heavy ions in SiC and SiO_2" J. Appl. Phys. 115 (2014) 044903

   K. Jin's involvement: proposed the critical data analysis procedure, performed the experimental data analysis, modified the TRIM-85 code to connect the electronic stopping power and the ion distributions, and wrote the paper.

JOURNAL OF APPLIED PHYSICS **115**, 044903 (2014)

Electronic stopping powers for heavy ions in SiC and SiO_2

K. Jin,[1] Y. Zhang,[1,2,a)] Z. Zhu,[3] D. A. Grove,[4] H. Xue,[1] J. Xue,[5] and W. J. Weber[1,2]
[1]*Department of Materials Science & Engineering, University of Tennessee, Knoxville, Tennessee 37996, USA*
[2]*Materials Science & Technology Division, Oak Ridge National Laboratory, Oak Ridge, Tennessee 37831, USA*
[3]*Pacific Northwest National Laboratory, P.O. Box 999, Richland, Washington 99352, USA*
[4]*Luxel Corporation, Friday Harbor, Washington 98250, USA*
[5]*State Key Laboratory of Nuclear Physics and Technology, School of Physics, Peking University, Beijing 100871, People's Republic of China*

(Received 10 November 2013; accepted 23 December 2013; published online 24 January 2014)

Accurate information on electronic stopping power is fundamental for broad advances in materials science, electronic industry, space exploration, and sustainable energy technologies. In the case of slow heavy ions in light targets, current codes and models provide significantly inconsistent predictions, among which the Stopping and Range of Ions in Matter (SRIM) code is the most commonly used one. Experimental evidence, however, has demonstrated considerable errors in the predicted ion and damage profiles based on SRIM stopping powers. In this work, electronic stopping powers for Cl, Br, I, and Au ions are experimentally determined in two important functional materials, SiC and SiO_2, based on a single ion technique, and new electronic stopping power values are derived over the energy regime from 0 to 15 MeV, where large deviations from the SRIM predictions are observed. As an experimental validation, Rutherford backscattering spectrometry (RBS) and secondary ion mass spectrometry (SIMS) are utilized to measure the depth profiles of implanted Au ions in SiC for energies from 700 keV to 15 MeV. The measured ion distributions by both RBS and SIMS are considerably deeper than the SRIM predictions, but agree well with predictions based on our derived stopping powers.
[http://dx.doi.org/10.1063/1.4861642]

3. **K. Jin**, Z. Zhu, S. Manandhar, J. Liu, C. Chen, V. Shutthanandan, S. Thevuthasan, W. J. Weber and Y. Zhang, "Angular distribution and recoil effect for 1 MeV Au^+ ions through a Si_3N_4 thin foil" Nucl. Instr. Meth. Phys. Res., Sect. B 332 (2014) 346

K. Jin's involvement: proposed and designed the experiments, prepared the samples, performed SIMS measurements, performed data analysis and wrote the paper.

Contents lists available at ScienceDirect

Nuclear Instruments and Methods in Physics Research B

journal homepage: www.elsevier.com/locate/nimb

Angular distribution and recoil effect for 1 MeV Au^+ ions through a Si_3N_4 thin foil

Ke Jin [a], Zihua Zhu [b,*], Sandeep Manandhar [b], Jia Liu [b], Chien-Hung Chen [a], Vaithiyalingam Shutthanandan [b], Suntharampillai Thevuthasan [b], William J. Weber [a,c], Yanwen Zhang [c,a,*]

[a] Department of Materials Science & Engineering, University of Tennessee, Knoxville, TN 37996, USA
[b] Environmental Molecular Sciences Laboratory, Pacific Northwest National Laboratory, P.O. Box 999, Richland, WA 99352, USA
[c] Materials Science & Technology Division, Oak Ridge National Laboratory, Oak Ridge, TN 37831, USA

ARTICLE INFO

Article history:
Available online 18 March 2014

Keywords:
Silicon nitride
Heavy ion
Stopping power
Angular distribution
SIMS

ABSTRACT

The Stopping and Range of Ions in Matter (SRIM) code has been widely used to predict nuclear stopping power and angular distribution of ion–solid collisions. However, experimental validation of the predictions is insufficient for slow heavy ions in nonmetallic compounds. In this work, time-of-flight secondary ion mass spectrometry (ToF-SIMS) is applied to determine the angular distribution of 1 MeV Au ions after penetrating a Si_3N_4 foil with a thickness of ~100 nm. The exiting Au ions are collected by a Si wafer located ~14 mm behind the Si_3N_4 foil, and the resulting 2-dimensional distribution of Au ions on the Si wafer is measured by ToF-SIMS. The SRIM-predicted angular distribution of Au ions through the Si_3N_4 thin foil is compared with the measured results, indicating that SRIM slightly overestimates the nuclear stopping power by up to 10%. In addition, thickness reduction of the suspended Si_3N_4 foils induced by 1 MeV Au ion irradiation is observed with an average loss rate of ~107 atoms/ion.

4. **K. Jin**, Y. Zhang, H. Xue, Z. Zhu and W.J. Weber, "Ion distribution and electronic stopping power for Au ions in silicon carbide" Nucl. Instr. Meth. Phys. Res., Sect. B 307 (2013) 65

   K. Jin's involvement: proposed the critical data analysis procedure, performed the experimental data analysis, and wrote the paper.

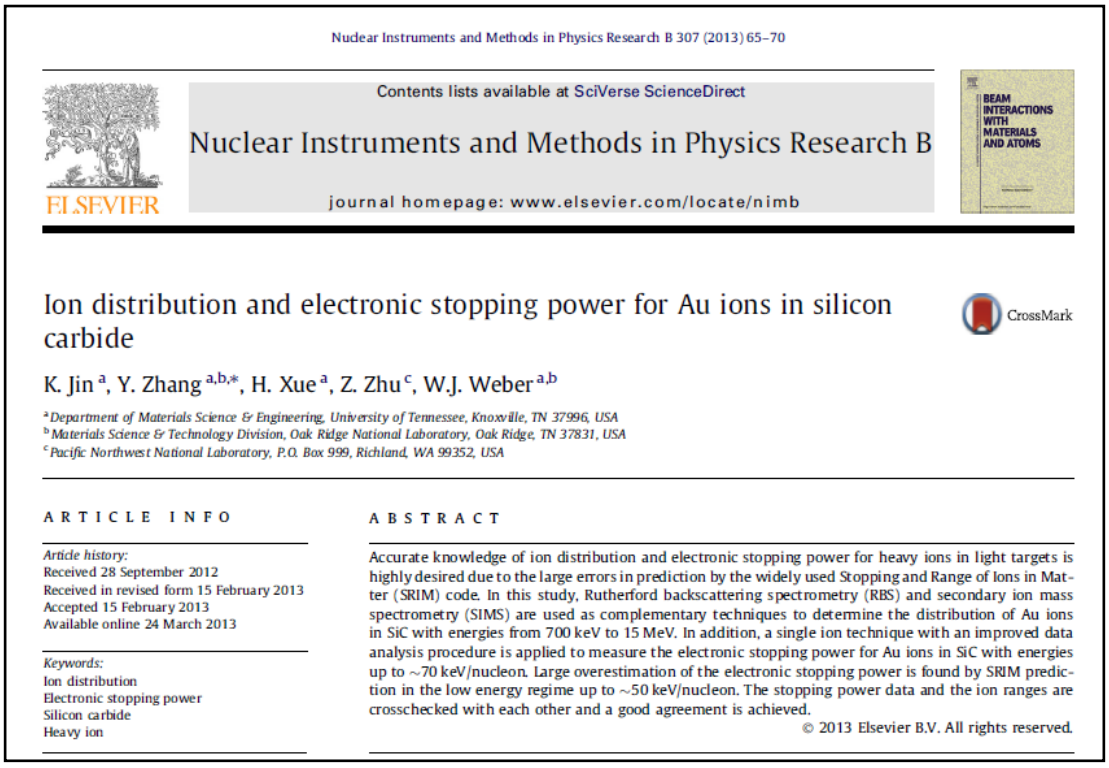

Nuclear Instruments and Methods in Physics Research B 307 (2013) 65–70

Contents lists available at SciVerse ScienceDirect

Nuclear Instruments and Methods in Physics Research B

journal homepage: www.elsevier.com/locate/nimb

Ion distribution and electronic stopping power for Au ions in silicon carbide

K. Jin [a], Y. Zhang [a,b,*], H. Xue [a], Z. Zhu [c], W.J. Weber [a,b]

[a] Department of Materials Science & Engineering, University of Tennessee, Knoxville, TN 37996, USA
[b] Materials Science & Technology Division, Oak Ridge National Laboratory, Oak Ridge, TN 37831, USA
[c] Pacific Northwest National Laboratory, P.O. Box 999, Richland, WA 99352, USA

ARTICLE INFO

Article history:
Received 28 September 2012
Received in revised form 15 February 2013
Accepted 15 February 2013
Available online 24 March 2013

Keywords:
Ion distribution
Electronic stopping power
Silicon carbide
Heavy ion

ABSTRACT

Accurate knowledge of ion distribution and electronic stopping power for heavy ions in light targets is highly desired due to the large errors in prediction by the widely used Stopping and Range of Ions in Matter (SRIM) code. In this study, Rutherford backscattering spectrometry (RBS) and secondary ion mass spectrometry (SIMS) are used as complementary techniques to determine the distribution of Au ions in SiC with energies from 700 keV to 15 MeV. In addition, a single ion technique with an improved data analysis procedure is applied to measure the electronic stopping power for Au ions in SiC with energies up to ~70 keV/nucleon. Large overestimation of the electronic stopping power is found by SRIM prediction in the low energy regime up to ~50 keV/nucleon. The stopping power data and the ion ranges are crosschecked with each other and a good agreement is achieved.

5. Z. Wang, **K. Jin**, Y. Zhang, F. Wang, and Z. Zhu, "ToF-SIMS depth profiling of insulating samples, interlaced mode or non-interlaced mode?" Surf. Interface Anal. 46 (2014) 257

   K. Jin's involvement: performed some SIMS measurements to assist seeking the optimized strategy of depth profiling of MgO.

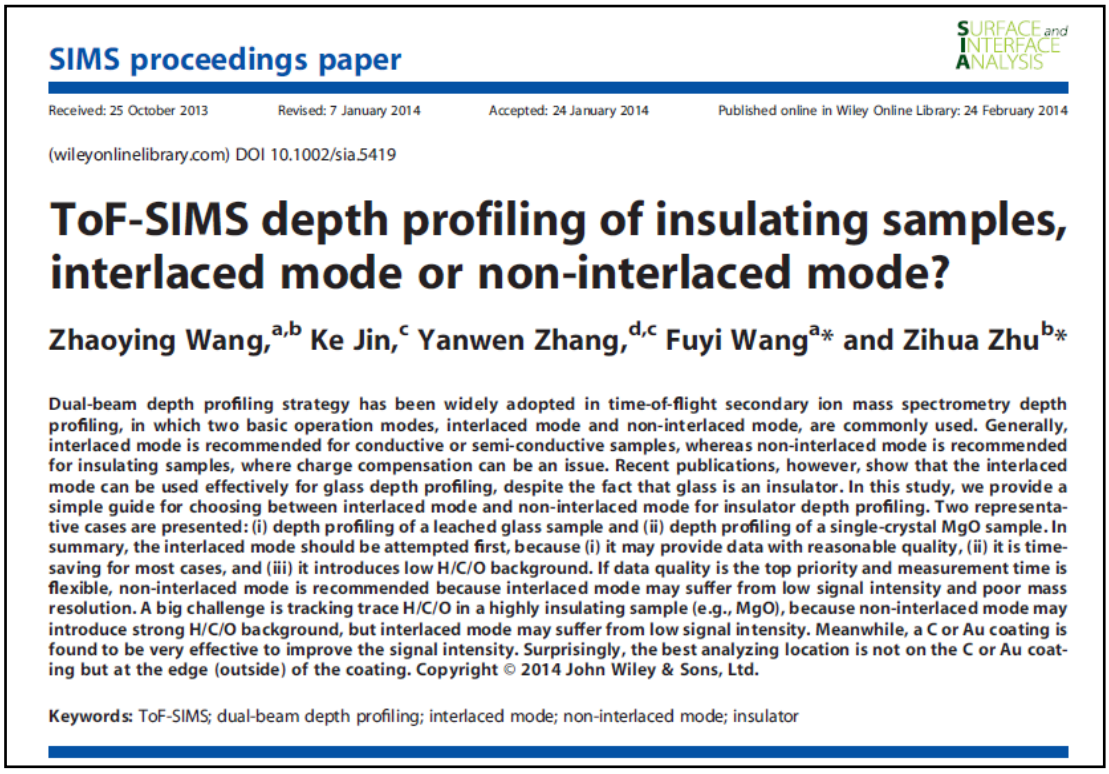

SIMS proceedings paper

SURFACE and INTERFACE ANALYSIS

Received: 25 October 2013 Revised: 7 January 2014 Accepted: 24 January 2014 Published online in Wiley Online Library: 24 February 2014

(wileyonlinelibrary.com) DOI 10.1002/sia.5419

ToF-SIMS depth profiling of insulating samples, interlaced mode or non-interlaced mode?

Zhaoying Wang,[a,b] Ke Jin,[c] Yanwen Zhang,[d,c] Fuyi Wang[a]* and Zihua Zhu[b]*

Dual-beam depth profiling strategy has been widely adopted in time-of-flight secondary ion mass spectrometry depth profiling, in which two basic operation modes, interlaced mode and non-interlaced mode, are commonly used. Generally, interlaced mode is recommended for conductive or semi-conductive samples, whereas non-interlaced mode is recommended for insulating samples, where charge compensation can be an issue. Recent publications, however, show that the interlaced mode can be used effectively for glass depth profiling, despite the fact that glass is an insulator. In this study, we provide a simple guide for choosing between interlaced mode and non-interlaced mode for insulator depth profiling. Two representative cases are presented: (i) depth profiling of a leached glass sample and (ii) depth profiling of a single-crystal MgO sample. In summary, the interlaced mode should be attempted first, because (i) it may provide data with reasonable quality, (ii) it is time-saving for most cases, and (iii) it introduces low H/C/O background. If data quality is the top priority and measurement time is flexible, non-interlaced mode is recommended because interlaced mode may suffer from low signal intensity and poor mass resolution. A big challenge is tracking trace H/C/O in a highly insulating sample (e.g., MgO), because non-interlaced mode may introduce strong H/C/O background, but interlaced mode may suffer from low signal intensity. Meanwhile, a C or Au coating is found to be very effective to improve the signal intensity. Surprisingly, the best analyzing location is not on the C or Au coating but at the edge (outside) of the coating.

Keywords: ToF-SIMS; dual-beam depth profiling; interlaced mode; non-interlaced mode; insulator

6. Y. Zhang, M.L. Crespillo, H. Xue, **K. Jin**, C.H. Chen, C.L. Fontana, J.T. Graham, and W.J. Weber, "New ion beam materials laboratory for materials modification and irradiation effects research" Nucl. Instr. Meth. Phys. Res., Sect. B 338 (2014) 19

K. Jin's involvement: as one of the major operators in the ion beam materials laboratory, performed the ion beam irradiation and RBS/channeling analysis shown in Figs. 5, 8, 10 and 12.

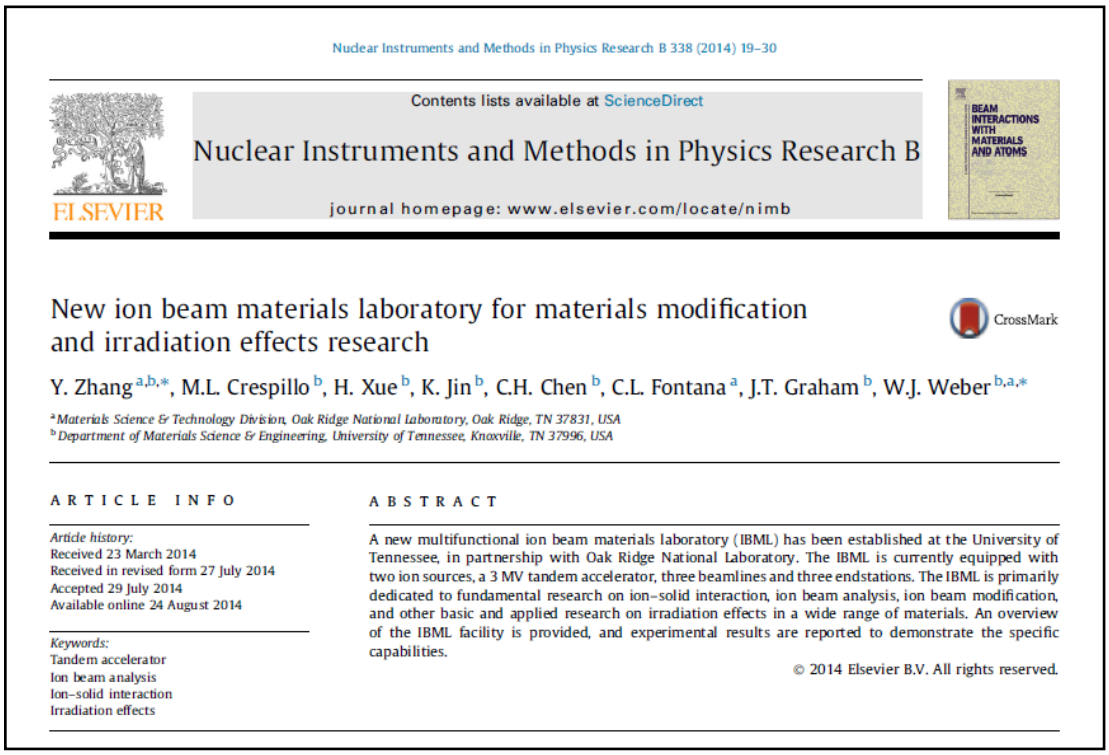

Nuclear Instruments and Methods in Physics Research B 338 (2014) 19–30

Contents lists available at ScienceDirect

Nuclear Instruments and Methods in Physics Research B

journal homepage: www.elsevier.com/locate/nimb

New ion beam materials laboratory for materials modification and irradiation effects research

Y. Zhang [a,b,*], M.L. Crespillo [b], H. Xue [b], K. Jin [b], C.H. Chen [b], C.L. Fontana [a], J.T. Graham [b], W.J. Weber [b,a,*]

[a] Materials Science & Technology Division, Oak Ridge National Laboratory, Oak Ridge, TN 37831, USA
[b] Department of Materials Science & Engineering, University of Tennessee, Knoxville, TN 37996, USA

ARTICLE INFO

Article history:
Received 23 March 2014
Received in revised form 27 July 2014
Accepted 29 July 2014
Available online 24 August 2014

Keywords:
Tandem accelerator
Ion beam analysis
Ion–solid interaction
Irradiation effects

ABSTRACT

A new multifunctional ion beam materials laboratory (IBML) has been established at the University of Tennessee, in partnership with Oak Ridge National Laboratory. The IBML is currently equipped with two ion sources, a 3 MV tandem accelerator, three beamlines and three endstations. The IBML is primarily dedicated to fundamental research on ion–solid interaction, ion beam analysis, ion beam modification, and other basic and applied research on irradiation effects in a wide range of materials. An overview of the IBML facility is provided, and experimental results are reported to demonstrate the specific capabilities.

7. W. J. Weber, E. Zarkadoula, O. H. Pakarinen, R. Sachan, M. F. Chisholm, P. Liu, H. Xue, **K. Jin**, and Y. Zhang, "Synergy of elastic and inelastic energy loss on ion track formation in $SrTiO_3$" Sci. Rep. 5 (2015) 7726

   K. Jin's involvement: performed part of the ion irradiations and RBS analysis.

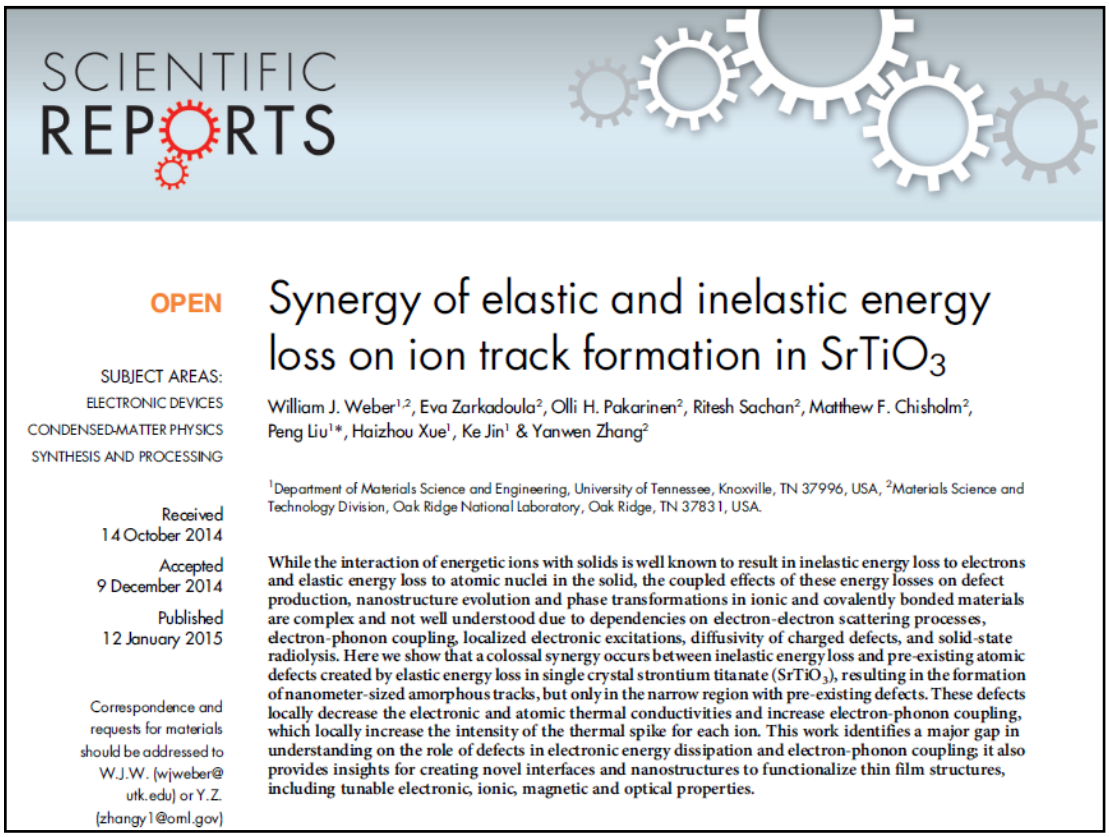

SCIENTIFIC REPORTS

OPEN

SUBJECT AREAS:
ELECTRONIC DEVICES
CONDENSED-MATTER PHYSICS
SYNTHESIS AND PROCESSING

Received
14 October 2014

Accepted
9 December 2014

Published
12 January 2015

Correspondence and requests for materials should be addressed to W.J.W. (wjweber@utk.edu) or Y.Z. (zhangy1@ornl.gov)

Synergy of elastic and inelastic energy loss on ion track formation in $SrTiO_3$

William J. Weber[1,2], Eva Zarkadoula[2], Olli H. Pakarinen[2], Ritesh Sachan[2], Matthew F. Chisholm[2], Peng Liu[1]*, Haizhou Xue[1], Ke Jin[1] & Yanwen Zhang[2]

[1]Department of Materials Science and Engineering, University of Tennessee, Knoxville, TN 37996, USA, [2]Materials Science and Technology Division, Oak Ridge National Laboratory, Oak Ridge, TN 37831, USA.

While the interaction of energetic ions with solids is well known to result in inelastic energy loss to electrons and elastic energy loss to atomic nuclei in the solid, the coupled effects of these energy losses on defect production, nanostructure evolution and phase transformations in ionic and covalently bonded materials are complex and not well understood due to dependencies on electron-electron scattering processes, electron-phonon coupling, localized electronic excitations, diffusivity of charged defects, and solid-state radiolysis. Here we show that a colossal synergy occurs between inelastic energy loss and pre-existing atomic defects created by elastic energy loss in single crystal strontium titanate ($SrTiO_3$), resulting in the formation of nanometer-sized amorphous tracks, but only in the narrow region with pre-existing defects. These defects locally decrease the electronic and atomic thermal conductivities and increase electron-phonon coupling, which locally increase the intensity of the thermal spike for each ion. This work identifies a major gap in understanding on the role of defects in electronic energy dissipation and electron-phonon coupling; it also provides insights for creating novel interfaces and nanostructures to functionalize thin film structures, including tunable electronic, ionic, magnetic and optical properties.

8. Y. Zhang, D.S. Aidhy, T. Varga, S. Moll, P.D. Edmondson, F. Namavar, **K. Jin**, C. N. Ostrouchov, and W.J. Weber, "The effect of electronic energy loss on irradiation-induced grain growth in nanocrystalline oxides" Phys. Chem. Chem. Phys. 16 (2014) 8051

K. Jin's involvement: assisted the data analysis

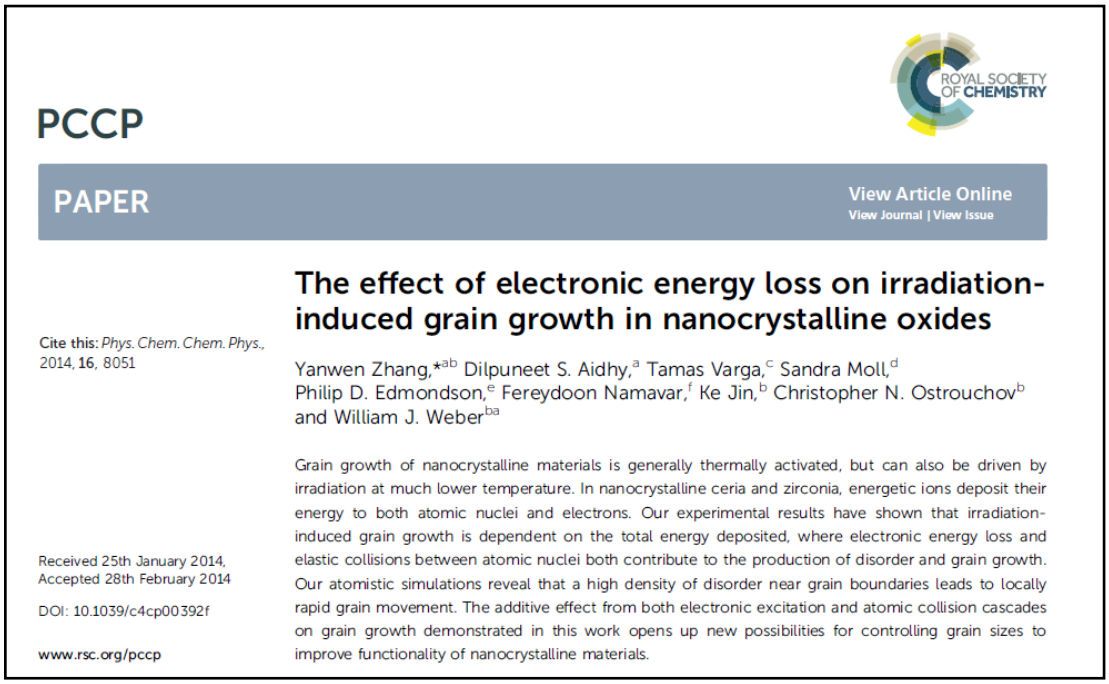

PCCP

PAPER

View Article Online
View Journal | View Issue

Cite this: *Phys. Chem. Chem. Phys.*, 2014, **16**, 8051

The effect of electronic energy loss on irradiation-induced grain growth in nanocrystalline oxides

Yanwen Zhang,*[ab] Dilpuneet S. Aidhy,[a] Tamas Varga,[c] Sandra Moll,[d] Philip D. Edmondson,[e] Fereydoon Namavar,[f] Ke Jin,[b] Christopher N. Ostrouchov[b] and William J. Weber[ba]

Grain growth of nanocrystalline materials is generally thermally activated, but can also be driven by irradiation at much lower temperature. In nanocrystalline ceria and zirconia, energetic ions deposit their energy to both atomic nuclei and electrons. Our experimental results have shown that irradiation-induced grain growth is dependent on the total energy deposited, where electronic energy loss and elastic collisions between atomic nuclei both contribute to the production of disorder and grain growth. Our atomistic simulations reveal that a high density of disorder near grain boundaries leads to locally rapid grain movement. The additive effect from both electronic excitation and atomic collision cascades on grain growth demonstrated in this work opens up new possibilities for controlling grain sizes to improve functionality of nanocrystalline materials.

Received 25th January 2014,
Accepted 28th February 2014

DOI: 10.1039/c4cp00392f

www.rsc.org/pccp

9. G. Cao, D. J. Singh, X. Zhang, G. Samolyuk, L. Qiao, C. Parish, **K. Jin**, Y. Zhang, H. Guo, S. Tang, W. Wang, J. Yi, C. Cantoni, W. Siemons, E. Payzant, M. Biegalski, T. Z. Ward, D. Mandrus, G.M. Stocks, and Z. Gai "Ferromagnetism and nonmetallic transport of thin-film α-$FeSi_2$: a stabilized metastable material" Phys. Rev. Lett. 114 (2015) 147202

K. Jin's involvement: performed RBS analysis to study the sample composition.

PRL 114, 147202 (2015) PHYSICAL REVIEW LETTERS week ending 10 APRIL 2015

Ferromagnetism and Nonmetallic Transport of Thin-Film α-$FeSi_2$: A Stabilized Metastable Material

Guixin Cao,[1] D. J. Singh,[2] X.-G. Zhang,[1] German Samolyuk,[2] Liang Qiao,[1] Chad Parish,[2] Ke Jin,[3] Yanwen Zhang,[3,2] Hangwen Guo,[2] Siwei Tang,[1,3] Wenbin Wang,[2] Jieyu Yi,[1,3] Claudia Cantoni,[2] Wolter Siemons,[2] E. Andrew Payzant,[1] Michael Biegalski,[1] T. Z. Ward,[2] David Mandrus,[3,2] G. M. Stocks,[2] and Zheng Gai[1,*]

[1]*Center for Nanophase Materials Sciences, Oak Ridge National Laboratory, Oak Ridge, Tennessee 37831, USA*
[2]*Materials Science and Technology Division, Oak Ridge National Laboratory, Oak Ridge, Tennessee 37831-6056, USA*
[3]*Department of Materials Science and Engineering, University of Tennessee, Knoxville, Tennessee 37996, USA*

(Received 1 September 2014; revised manuscript received 27 January 2015; published 7 April 2015)

A metastable phase α-$FeSi_2$ was epitaxially stabilized on a silicon substrate using pulsed laser deposition. Nonmetallic and ferromagnetic behaviors are tailored on α-$FeSi_2$ (111) thin films, while the bulk material of α-$FeSi_2$ is metallic and nonmagnetic. The transport property of the films renders two different conducting states with a strong crossover at 50 K, which is accompanied by the onset of a ferromagnetic transition as well as a substantial magnetoresistance. These experimental results are discussed in terms of the unusual electronic structure of α-$FeSi_2$ obtained within density functional calculations and Boltzmann transport calculations with and without strain. Our finding sheds light on achieving ferromagnetic semiconductors through both their structure and doping tailoring, and provides an example of a tailored material with rich functionalities for both basic research and practical applications.

DOI: 10.1103/PhysRevLett.114.147202 PACS numbers: 75.47.Np, 68.55.-a, 72.80.Ga

VITA

Ke Jin was born in Beijing, China in 1988. After graduating from Beijing National Day School, Beijing, China in 2006, Ke was enrolled in Peking University, Beijing, China, where he earned his Bachelor's Degree in Physics in 2010. Then he went to the University of Florida, Gainesville, FL, in the same year and earned his Master's Degree in Materials Science and Engineering in 2011. Since then, he started to pursue a doctorate in Materials Science and Engineering at the University of Tennessee, under the guidance of Dr. Yanwen Zhang.